

Exploring the Chemistry of Re^I: Physical and Theoretical Investigations

by

Philip D. Bulsink

*Thesis submitted to the
Faculty of Graduate and Postdoctoral Studies
In partial fulfilment of the requirements
For the degree of*

***Master of Science
In
Chemistry***

*Ottawa-Carleton Chemistry Institute
University of Ottawa*

Supervisors: Professors Darrin Richeson & Tom Woo

Abstract

The development of Rhenium I photocatalysts has been pursued since Lehn first showed the excellent performance of the Re^I bipyridine tricarbonyl catalyst. Since then, development has modified the organic ligand to demonstrate continued or improved activity with other α -diimine bidentate geometries. Geometry has been limited to κ^2 motifs, with *fac*-(CO)₃ and axial halides. This work will demonstrate the synthesis, characterization, and testing of a new $\kappa^3(L_3)-Re^1(CO)_2X$ (X = Cl, Br, CN, OTf) family of compounds for CO₂ reduction, as well as computational investigations into the mechanism of the reduction of CO₂ to CO and other species.

Acknowledgements

I'm thankful for the assistance of my supervisors Dr. Darrin Richeson and Dr. Tom Woo, in guiding this research, providing suggestions and assistance, and for help with editing of this thesis and other papers and projects.

Thanks to the members of the Richeson and Woo research groups, both past and present, for the assistance provided and for making the time spent researching and writing this thesis enjoyable. Thanks as well to Frank and Sean in the Brusso lab, for their help with their spectroscopic characterization equipment (IR, UV-Vis, and Fluorescence). Thanks to Jake and the Gambarotta laboratory for use of their GC, Rola and the Detellier lab for the assistance with the TGA, and to the Sciano Lab, especially Janice, Charles, and Deni, for their assistance in use of their photolysis equipment.

I'd like to thank Dr. Ilia Korobkov for his work measuring and solving the x-ray crystal structures of the compounds discussed. He assisted with some paper writing as well.

Finally, I'd like to thank my wife Leanne and my parents for their unending support, and understanding when I came home frustrated or exhausted from a day in the lab.

Contents

1	Introduction	1
1.1	Photochemistry & Catalysis	1
1.2	Rhenium	3
1.3	CO ₂ Reduction Chemistry	5
1.4	Objectives	6
2	New Coordination Geometries for Re^I	7
2.1	Introduction	7
2.2	Synthesis of Bidentate and Terdentate Re ^I Complexes	8
2.3	Characterization	11
2.3.1	NMR Analysis	11
2.3.2	Structure Analysis with X-Ray Crystallography and DFT	15
2.3.3	Infra-Red Spectroscopy	27
2.3.4	Photophysical Properties	30
2.3.5	Fluorescence	34
2.4	Conclusions	35
3	Photocatalysis of CO₂	37
3.1	Introduction	37
3.2	Photocatalytic Reactions with New Compounds	38
3.2.1	Conditions	38
3.2.2	Experimental Results	38
3.2.3	Rationalization of Results	39
3.3	Conclusions	44
4	Mechanism of CO₂ Reduction	45
4.1	Introduction	45

4.2	Mechanism Pathways	46
4.2.1	Excimer Formation and Decomposition of the Sacrificial Amine	49
4.2.2	The ‘Bicarbonate’ Pathway	52
4.2.3	The ‘Formate’ Pathway	58
4.2.4	The ‘Water-Gas Shift’ Pathway	62
4.3	Comparison Between Mechanistic Pathways	68
4.4	Conclusions	70
5	TurboControl	71
5.1	Development	72
5.2	Usage	74
5.3	Conclusions	75
6	Conclusions	76
A	Experimental Procedures	78
A.1	General Methods	78
A.2	Computational Methods	79
A.3	X-ray Crystallography	80
A.4	(terpy- κ^2 -N,N')Re(CO) ₃ Cl (2.1)	81
A.5	(terpy- κ^3 -N,N',N'')Re(CO) ₂ Cl (2.2)	82
A.6	(terpy- κ^2 -N,N')Re(CO) ₃ Br (2.3)	82
A.7	(terpy- κ^3 -N,N',N'')Re(CO) ₂ Br (2.4)	83
A.8	(terpy- κ^2 -N,N')Re(CO) ₃ CN (2.5)	83
A.9	(terpy- κ^3 -N,N',N'')Re(CO) ₂ CN (2.6)	84
A.10	(terpy- κ^2 -N,N')Re(CO) ₃ OTf (2.7)	84
A.11	(terpy- κ^3 -N,N',N'')Re(CO) ₂ OTf (2.8)	85
B	X-ray Crystal Structures	86
C	Molecular Orbitals Diagrams	92
D	Reaction Potential Energy Diagrams	101
E	TurboControl and TurboGo Manual	111
E.1	Introduction	111
E.2	System Requirements	111

E.3	Installation	112
E.4	TurboGo	113
E.5	TurboControl	113
E.6	Input File Format	115
E.6.1	Keywords	115
E.6.2	Route Card Options	116
E.6.3	Title	117
E.6.4	Charge and Spin	117
E.6.5	Geometry	117
E.6.6	Additional control File Modifications	117
E.6.7	Example Input File	118
E.7	Code Details	118
E.8	Citing TurboControl	120
E.9	License	120

Glossary of Terms	122
-------------------	------------

List of Tables

2.1	Crystal data and structure refinement for compounds 2.1 , 2.3 , and 2.5	15
2.2	Solvated and gas phase energy differences between Axial & Trans geometries of κ^x -(terpy)-Re(CO) _{5-x} CN (x=2,3)	18
2.3	Selected Distances, Angles, and Torsions for 2.1	20
2.4	Selected Distances, Angles, and Torsions for 2.3	21
2.5	Selected Distances, Angles, and Torsions for 2.5	22
2.6	Selected Distances, Angles, and Torsions for 2.2	25
2.7	Selected Distances, Angles and Torsions for Acetonitrile Adduct of 2.8 . .	26
2.8	Crystal data and structure refinement for compounds 2.2 and 2.8	27
4.1	Energies for the reaction steps in the photoinduced excimer formation pathway	51
4.2	Energies for the reaction steps in the ‘carbonate’ pathway	53
4.3	Energies for the reaction steps in the ‘formate’ pathway	59
4.4	Energies for the reaction steps in the ‘water-gas shift’ mechanism	62
4.5	Energies for the reaction steps in the ‘equatorial’ geometry	66

List of Figures

1.1	Two common bidentate complexes using terdentate ligands.	4
2.1	Results of TGA analysis on 2.1 and 2.3	9
2.2	The aromatic region of the ^1H NMR spectra of the four bidentate compounds.	12
2.3	The aromatic region of the ^1H NMR spectra showing bidentate - terdentate conversion.	13
2.4	Proton-explicit skeletal drawing of 2,2':6',2"-terpyridine.	13
2.5	The aromatic region of the ^1H NMR spectra of the four terdentate compounds.	14
2.6	The ^{13}C NMR spectra of 2.1	14
2.7	X-ray crystal structure representation for 2.1 , 2.3 and 2.5	17
2.8	X-ray crystal structure representation for 2 and 8	23
2.9	FTIR Spectra for complexes 2.1 and 2.2	28
2.10	DFT predicted FTIR spectra for 2.1 and 2.2	29
2.11	FTIR Spectra for complexes 2.7 and 2.8	30
2.12	UV-Vis spectra for compounds 2.1 , 2.3 , 2.5 , and 2.7	31
2.13	UV-Vis spectra for compounds 2.2 , 2.4 , 2.6 , and 2.8	31
2.14	Plots of the experimental and computed UV-Vis spectra for compound 2.1 . .	32
2.15	Plots of the experimental and computed UV-Vis spectra for compound 2.2 . .	33
2.16	UV-Vis and fluorescence spectra for 2.1 and 2.2	35
3.1	A photograph of aged and fresh catalytic mixture.	40
3.2	UV-Visible spectra of freshly prepared and aged catalyst mixture.	41
3.3	Structure and absorption spectra of proposed $[\kappa^3\text{-(terpy)}-\text{Re}(\text{CO})_3]^+$. .	42
3.4	Structure and absorption spectra of the catalyst-TEOA complex.	43
4.1	Potential Energy Surface for the production of the excimer.	52

4.2	DFT calculated structures for the ‘bicarbonate’ mechanistic pathway.	55
4.3	Potential Energy Surface for the bicarbonate mechanistic pathway.	56
4.4	DFT calculated structures for the ‘formate’ mechanistic pathway.	59
4.5	Potential Energy Surface for the formate mechanistic pathway.	60
4.6	DFT calculated structures for the axial ‘water-gas shift’ mechanistic pathway.	64
4.7	Potential Energy Surface for the axial geometry of the water-gas shift mechanistic pathway.	65
4.8	DFT calculated structures for the equatorial ‘water-gas shift’ mechanistic pathway.	66
4.9	Potential Energy Surface for the planar geometry of the water-gas shift mechanistic pathway.	67
4.10	An overview of the energies of the three mechanistic pathways of photochemical CO ₂ reduction in DMF.	69

List of Schemes

2.1	Synthesis of 2.1 and 2.3	8
2.2	Synthesis of 2.2 and 2.4	10
2.3	Anion exchange pathways.	10
3.1	Reorganization from catalytic excimer to form 3.1	41
4.1	Overview of mechanistic pathways.	47
4.2	Formation of the excimer species via absorption of a photon and oxidation of the sacrificial amine.	50
4.3	Decomposition pathway for the sacrificial amine.	51
4.4	The ‘bicarbonate’ mechanistic pathway.	54
4.5	The ‘formate’ mechanistic pathway.	58
4.6	The ‘water-gas shift’ mechanistic pathway.	63
4.7	Rearrangement of carbonyl and open site.	65

Chapter 1

Introduction

Common distinctions split most chemical compounds into one of two categories: organic and inorganic. Organic molecules contain carbon and hydrogen, with or without additional nitrogen, oxygen, phosphorus, sulphur, and the halides. Inorganic chemistry is, therefore, considered to be the remainder of the molecules possible. While they may include some aspect of organic chemistry (especially in organometallic molecules), the main structural motif or reactive center is a non-organic feature. These inorganic compounds can range from compounds such as lithium or Grignard reagents with significant organic influence, to metallic alloys or mineral compounds. With such a wide range of possibilities, inorganic chemistry has many facets. A widely active research area is the development and testing of transition metal complexes for catalytic, photo-physical, biochemical or manufacturing uses.

1.1 Photochemistry & Catalysis

A report of the first synthesized organometallic complex was published by Zeise in 1831.¹ To form what is now known as Zeise's salt, $\text{K}[\text{PtCl}_3(\text{C}_2\text{H}_4)] \cdot \text{H}_2\text{O}$, he mixed platinum

chloride with ethanol, followed by a reaction with potassium chloride.² After some controversy to the composition of this, it was confirmed by Griess and Martius,³ and later expanded upon by Birnbaum.⁴

The field of organometallics was expanded greatly by Frankland,² and many of his complexes were catalytically active. Further development of this new type of chemistry quickly led to useful catalysts for the conversion of petroleum products and other chemistries, using nearly all of the transition metals. These catalysts take all forms, from simple olefin and halide compounds to multi-metallic complexes with large organic ligands.

Some of the most significant organometallic catalysts since the late 1990s have been the development of earth metal pincer complexes to replace noble metal or early transition metal catalysts, which are often more toxic or expensive to produce. Brookhart and Gibson published a series of papers^{5–8} on the use of iron and cobalt with bis(imino)pyridine ligands to perform ethylene polymerization at rates exceeding those of similar noble metal complexes and metallocenes.⁹ The role of the ligand in the mechanism is still up for debate, but many modified systems have been synthesized and tested since the first work was published.¹⁰

Many of these types of pincer complexes are photochemically active. In transition metal complexes, the interaction between the metal atom(s) and the ligands can cause significant electron mobility upon the absorption of incident photons. The metal atom's *d* orbitals typically lie at or near the Highest Occupied Molecular Orbital (HOMO) energy, while the ligands often have low energy anti-bonding orbitals (π^*) at the Lowest Unoccupied Molecular Orbital (LUMO) levels. When a photon is absorbed and is promoted from the ground state to the excited state, that state is spatially removed from the metal centre, this motion of the electron is labelled a Metal-Ligand Charge Transfer

(MLCT). Formally, the metal atom is oxidized by the photons, this oxidation allows for redox reactivity at the metal centre for as long as the electron remains removed to the ligand. Relaxation (through photon emission via fluorescence or phosphorescence, or via vibrational or other motion processes) can return the electron to the metal to reform the ground electronic state.

1.2 Rhenium

Rhenium compounds in particular are known to have a broad range of applications. Their use in catalysis has been explored, covering olefin hydrogenation,¹¹ epoxidation (with chiral selectivity),¹² and in a host of organic bond formation reactions¹³ (Friedel-Crafts acylation and alkylation,^{14–16} nucleophilic addition,^{17,18} carbon-carbon coupling,^{19,20} as well as other heteroatom-carbon bond formation^{21–25}). Rhenium has also been used in radiopharmaceutical applications, due to the availability of moderately radioactive isotopes.^{26,27} These compounds exhibit other interesting fundamental photophysical properties as well.²⁸

Since the mid-1970s, complexes containing the α -diimine Re^I tricarbonyl core have attracted a great deal of attention due to their attractive photochemical properties. The pseudo-octahedral *fac*-[L₂Re(CO)₃X] and *fac*-[L₂(L')Re(CO)₃]⁺ complexes have been the dominant species.^{29–39} A large family of compounds with these formulations have been accessed by the addition of chelating diimine σ -donor ligands to [Re(CO)₅X] with the quantitative replacement of two *cis* carbonyls in the Re^I starting material.^{29,40–48} Significantly, these reactions form only bidentate coordinated ligands with *facial* tricarbonyl isomers as products even when a potentially tridentate σ -donor, such as bis(imino)pyridine or 2,2':6',2"-terpyridine, are employed in the reaction (see Figure 1.1).^{49–52}

These robust species have been examined for potential applications in organic light-

emitting diodes (OLEDs),^{53,54} chemosensors and biotechnology probes,^{55–59} fluorescence microscopy imaging of cells,^{55,60–63} as chemotherapy agents,⁶⁴ in the formation of macromolecules,⁶⁵ and the photochemical reduction of CO₂ to CO.^{66–70} Among the key photo-physical features of these α -diimine Re^I compounds is the electron transfer capability of this system and the interplay between the Re center and the well-known non-innocent redox activity of the ligands.^{71,72}

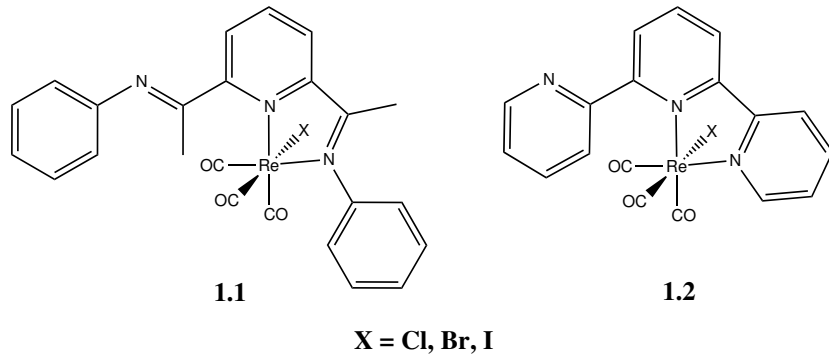


Figure 1.1 Two common *fac*-[L₂Re(CO)₃X] complexes with terdentate σ -donor ligands: L = bis(imino)pyridine (**1.1**) and 2,2':6',2''-terpyridine (**1.2**).

Further development of this chemistry has been restricted by the limited structural and electronic variability of the common pseudo-octahedral *fac*-[L₂ReX(CO)₃] (L₂ = α -diimine) products. While these systems continue to receive considerable attention, studies detailing the coordination chemistry of the meridionally-coordinated tridentate triimine Re^I dicarbonyl core are quite limited.⁷³ For example, while κ^3 (terpy)Re(CO)₂Cl was initially reported in 1988,⁷⁴ closer analysis of the reported analytical data (including ¹H NMR) indicate that this compound is more likely κ^2 LRe(CO)₃Cl. A more recent report for this compound provides spectroscopic details of this species as well as the preliminary report for the generation of [κ³(terpy)Re(CO)₂L']⁺ cations (L = PPh₃, PEt₃, NC₅H₅, and NCCH₃).⁷⁵ Finally, the ¹H NMR data for κ³(terpy)Re(CO)₂Br has been reported⁵¹ but accompanied no other characterization.

In order to fully exploit the potential of this versatile family of compounds, the limits imposed by the bidentate coordination need to be addressed. Furthermore, it would appear that, on the basis of the tridentate ligands that have been investigated, the concerted effort to produce the tridentate species has been essentially unsuccessful, or requiring harsh conditions.⁵²

1.3 CO₂ Reduction Chemistry

Recent years have seen an increase in the concentration of CO₂ in the atmosphere as a product of combustion of oil, gas and coal in the industry and transportation sectors.⁷⁶ This is of significant concern due to the greenhouse gas properties of CO₂.^{77,78} Attempts to reduce emissions proceed by various pathways, including the utilization of renewable resources such as wind and solar for energy production;⁷⁹ development of more fuel and energy efficient processes; and attempts to capture CO₂ from industrial exhaust streams.^{80–82} It can then be stored in underground depositories, or used as a feedstock in the production of simple molecules or fuels.^{83–85} Due to it being the final product in combustion and its high thermodynamic stability, the reduction of CO₂ is an energy-intensive task.^{86,87} While plant life naturally performs CO₂ transformation via photosynthesis, no artificial means have proven to be robust and scalable enough for the task in large scale.⁸⁸

The development of catalysts for ‘artificial photosynthesis’ has explored various means, including utilizing metal electrodes,⁸⁹ electrocatalytic semiconductors (such as TiO₂, ZnS, CdS, or As or S doped Ag),^{90,91} and organometallic species of Co, Ni, Mn, and Fe (particularly porphyrin complexes).^{92–102} These typically require the addition of electrons, and current trends look to solar powered electricity production for a ‘green’ CO₂ reduction platform.¹⁰³

Alternate solutions involves the use of photoredox catalysts, including α -diimino complexes of Re^I, Ru^{II}, Os^{II}, and Ir^{III}.^{66,104–114} In recent years, the popularity of these α -diimino compounds has increased, owing to their unique MLCT excited states and easily tunable photophysical properties. Of these complexes, Re^I based catalysts are of particular interest. Whether acting as a mono-metallic photocatalyst, or with Ru in multi-metallic complexes, the high quantum yield (up to $\Phi=0.59$)^{115,116} and exclusive selectivity to production of CO is unparalleled in these catalysts.^{117,118} Research focus has turned to tuning photophysical properties for increased use of photons in the visible spectrum (particularly lower energy) and modification of the ligand framework for increased turnover numbers and frequencies.^{87,117,119–121}

1.4 Objectives

Attracted by the challenge of synthesizing Re^I terdentate compounds, the objectives were to synthesize, crystallographically authenticate, and investigate the photophysical properties of low-valent rhenium pincer complexes displaying an N,N',N"-chelated terpyridine array.

Complexes of 2,2':6',2"-terpyridine (terpy) are of interest due to the conceptual relationship to established bis(imino)pyridine compounds.^{122,123} This thesis will be a discussion of the development of chemistry of Re^I complexes, their characterization, and comparison of structural and photo-physical properties to computed values.

This thesis will focus on the synthesis and testing of a novel Re^I catalyst attempting to improve on those points. It will also provide a more detailed examination at specifics of the mechanisms proposed for current Re^I diimine catalysts, and propose new geometries for prior mechanistic steps based on experimental, computational, and literature review work.

Chapter 2

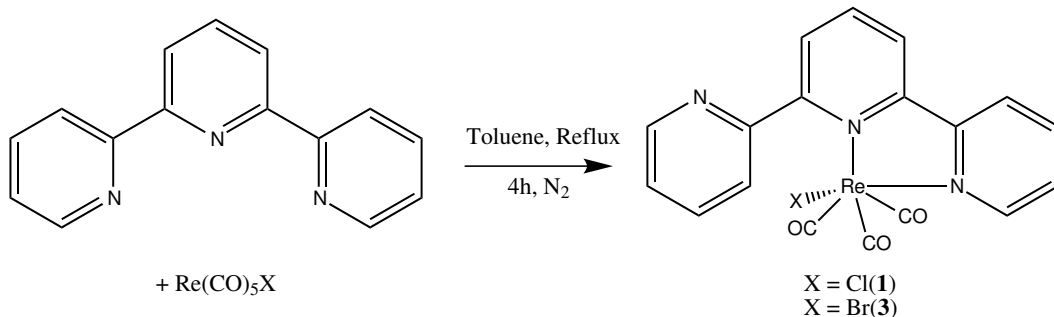
New Coordination Geometries for Re^I

2.1 Introduction

Re^I compounds have been typically bidentate (κ^2) compounds, even when using a potentially terdentate (κ^3) ligand such as bis(imino)pyridine or terpyridine (refer to Figure 1.1). The chemistry of this rhenium α -diimino complex has been extensively investigated, with over 1700 references appearing in a SciFinder structure search for that metal-ligand motif.¹²⁴ The ejection of an additional carbonyl and the chelation of the pendant arm of the ligand was attempted to extend the conjugated π system of the ligand and its interaction with the metal centre. This was first demonstrated by prior work in our group for the bis(imino)pyridine ligand.⁷³ This section will demonstrate the expansion of the possible rhenium(I) pincer complex geometries by synthesizing and characterizing a series of terdentate complexes with the 2,2':6'2"-terpyridine ligand.

2.2 Synthesis of Bidentate and Terdentate Re^I Complexes

Similar to the prior work, synthesis began with the production of the bidentate complex $\kappa^2(\text{terpy})\text{Re}(\text{CO})_3\text{X}$ ($\text{X} = \text{Cl}, \text{Br}$) by coordination of 2,2':6',2"-terpyridine with a $\text{Re}(\text{CO})_5\text{X}$ starting material in dry toluene at reflux for 4 hours, as shown in Scheme 2.1. A bright yellow powder precipitated from solution and was collected by filtration, washed with cold hexanes, and dried *in vacuo* to a good yield of **2.1** and **2.3** respectively.ⁱ These bidentate compounds were characterized fully and used without further purification to produce $\kappa^3(\text{terpy})\text{Re}(\text{CO})_2\text{X}$ ($\text{X} = \text{Cl}, \text{Br}$) via thermolysis, as well as for anion exchange reactions.



Scheme 2.1 Synthesis of **2.1** and **2.3** from $\text{Re}(\text{CO})_5\text{X}$ and 2,2':6',2"-terpyridine.

Conversion of compounds **2.1** and **2.3** to the κ^3 moiety required the release of CO and the subsequent coordination of the free pendant arm. Prior work had identified the thermal lability of the carbonyl, based on a method first described by Buckingham with a osmium complexes.¹²⁵ In this method, a ceramic sample boat was placed in a tube furnace at elevated temperature, under a flowing atmosphere of N₂. After some time, the sample is removed and collected at nearly quantitative yield. Determination of

ⁱExperimental details for all compounds can be seen in Appendix A Experimental Procedures

the appropriate thermolysis temperature was performed by Thermogravimetric Analysis (TGA) of the sample. A loss of 6-8 % of starting mass from the sample is consistent with the loss of one carbonyl group from the complex. Results of TGA on **2.1** and **2.3** is shown in Figure 2.1.

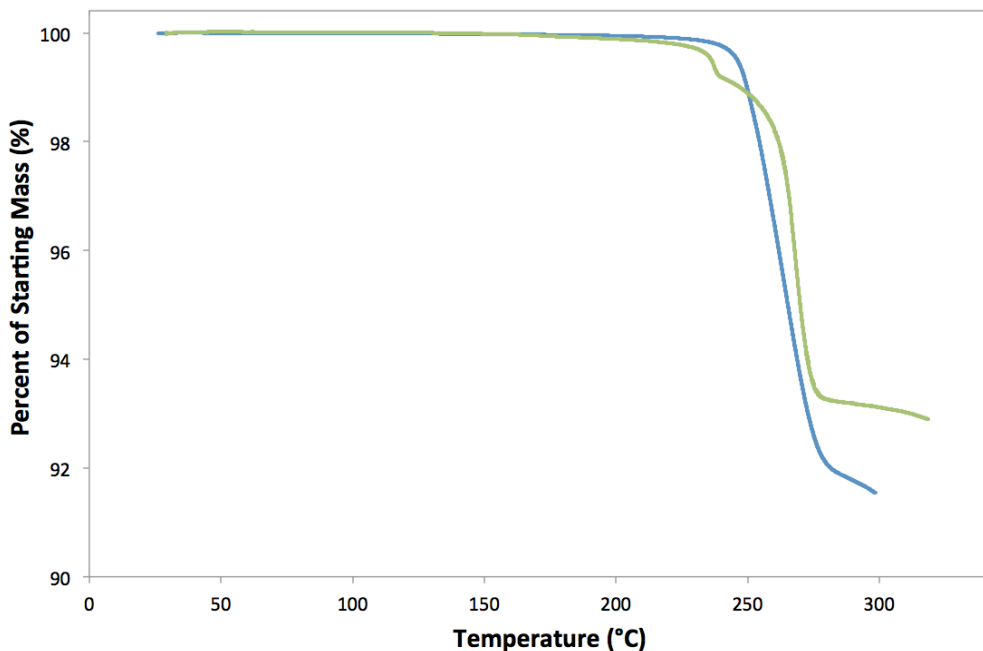
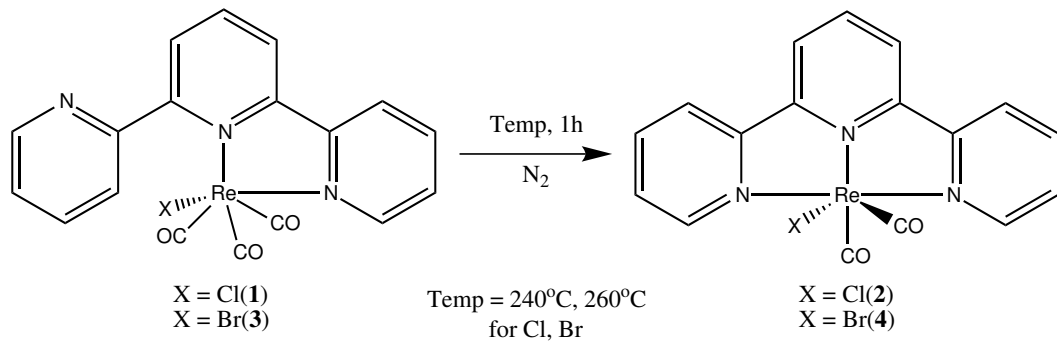


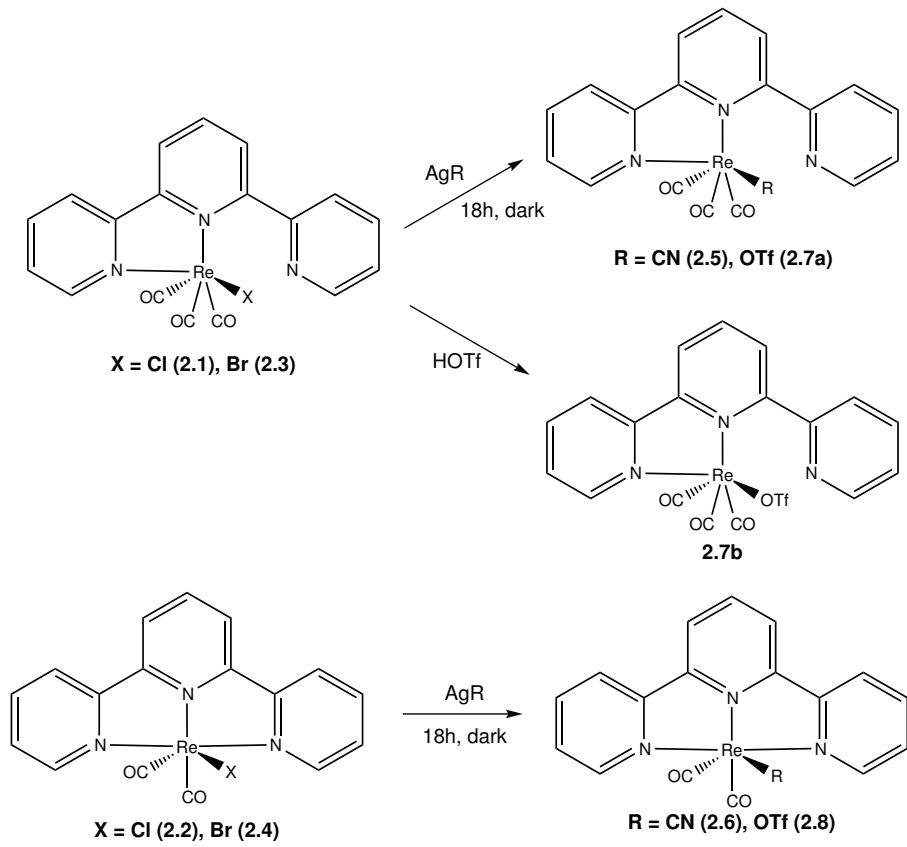
Figure 2.1 Results of TGA analysis on **2.1** (blue) and **2.3** (green).

The onset of mass loss in the TGA of **2.1**, and the onset of the main mass loss in the TGA of **2.3** were chosen to identify a thermolysis temperature for each sample. For **2.1**, thermolysis was performed at 240 °C, and for **2.3** thermolysis was performed at 260 °C, yielding **2.2** and **2.4** respectively, at quantitative yields, by the pathway in Scheme 2.2.

Further reactions were carried out on the above products to yield triflate and cyano complexes in bidentate and terdentate geometries. These anion exchange reactions were performed by the addition of the silver salt to the chloride products **2.1** or **2.2**, to precipitate AgCl, leaving $\kappa^2(\text{terpy})\text{Re}(\text{CO})_3\text{CN}$ (**2.5**), $\kappa^3(\text{terpy})\text{Re}(\text{CO})_2\text{CN}$ (**2.6**), $\kappa^2(\text{terpy})\text{Re}(\text{CO})_3\text{OTf}$ (**2.7a**) and $\kappa^3(\text{terpy})\text{Re}(\text{CO})_2\text{OTf}$ (**2.8a**), as shown in Scheme 2.3.



Scheme 2.2 Synthesis of **2.2** and **2.4** by thermolysis of **2.1** or **2.3**, respectively.



Scheme 2.3 Anion exchange pathways to synthesize **2.5** - **2.8**.

Reaction with the bromide products proceeds with similar results. As the Ag anion exchange reactions result in only moderate yields, **2.7b** was synthesized by the direct

addition of neat triflic acid ($\text{CF}_3\text{SO}_3\text{H}$) to **2.1**. HCl was released, the solutions were quenched by addition of dilute aqueous NaCO_3 , and product was collected via separation into chloroform, again at moderate yield.

2.3 Characterization

Full characterization was performed, including Nuclear Magnetic Resonance (NMR) analysis, x-ray crystallography, elemental analysis, as well as UV-Vis and IR spectroscopy. Computational Density Functional Theory (DFT) methods were used to solve the geometries, and Time Dependant Density Functional Theory (TD-DFT) was performed to predict UV-Vis spectra and identify electronic transitions.

2.3.1 NMR Analysis

Proton NMR was performed on each of the samples. Each sample was dissolved completely in deuterated acetonitrile (CD_3CN) and analysis was performed on a Bruker AVANCE 400 MHz spectrometer. Data was processed from the FID signal via the Top-Spin program, and spectra were analyzed using ACD NMR Processor v12.0.

Detailed peak analysis comparing bidentate samples **2.1**, **2.3**, **2.5**, and **2.7** (Figure 2.2) or terdentate **2.2**, **2.4**, **2.6**, and **2.8** (Figure 2.5) show little difference between samples. This is due to the distance between the anion and any protons on the ligand. Anions with different σ -donor strength marginally impact the metal-ligand interactions; these have only small effect on the location of peaks, shifting between samples by typically less than 0.1 ppm. As is shown in Figure 2.2, the characteristic shape of each spectra remains constant, only exact peak locations and some peak order varies with anion choice.

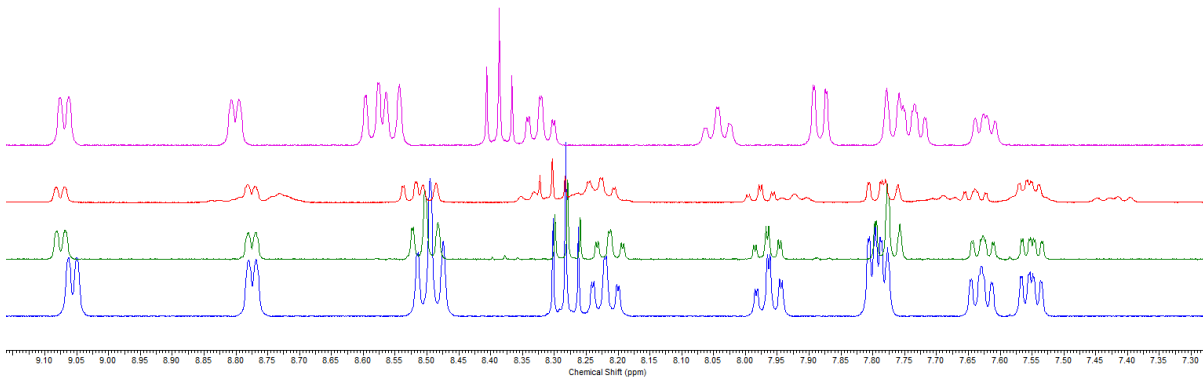


Figure 2.2 The aromatic region of the ¹H NMR spectra for bidentate compounds **2.1** (blue), **2.3** (green), **2.5** (red) and **2.7** (purple).

The characteristic feature in the NMR spectra after the transformation from bidentate to terdentate (e.g. sample **2.1** to **2.2**) is the reduction in the total number of the signals in the aromatic region (between 7 and 9 ppm). This simplification is due to the increased symmetrization of the ligand, while the κ^2 -bidentate ligand has a freely rotating pendant group. Prior work in literature⁵¹ and in our group¹²⁶ shows the temperature dependence of the rate of rotation of this pendant arm for various ligand species. However, the κ^3 -terdentate species has no free groups, the rigid geometry and higher order symmetry results in the simpler NMR spectrum.

The simplification of peaks due to the symmetrization of the ligand results in the peaks from free pendant arm protons *a*, *b*, *c*, and *d* (see Figure 2.4) with peaks at 9.06, 7.63, 8.22 and 7.79 ppm, respectively, aligning with their mirroring peaks at *a'*, *b'*, *c'* and *d'* (with peaks at 8.77, 7.55, 7.96, and 7.80 ppm). The new symmetrized peaks show integrations of two protons per peak, relative to the single proton (*f*) peak from the central pyridyl ring, *para* to the nitrogen. As well, the presence of metal-ligand interaction in the pendant arms reduces the deshielding effect, shifting the free pyridyl *ortho* proton from 9.06 to 8.77 ppm in the chelated group, with similar shifts evident for

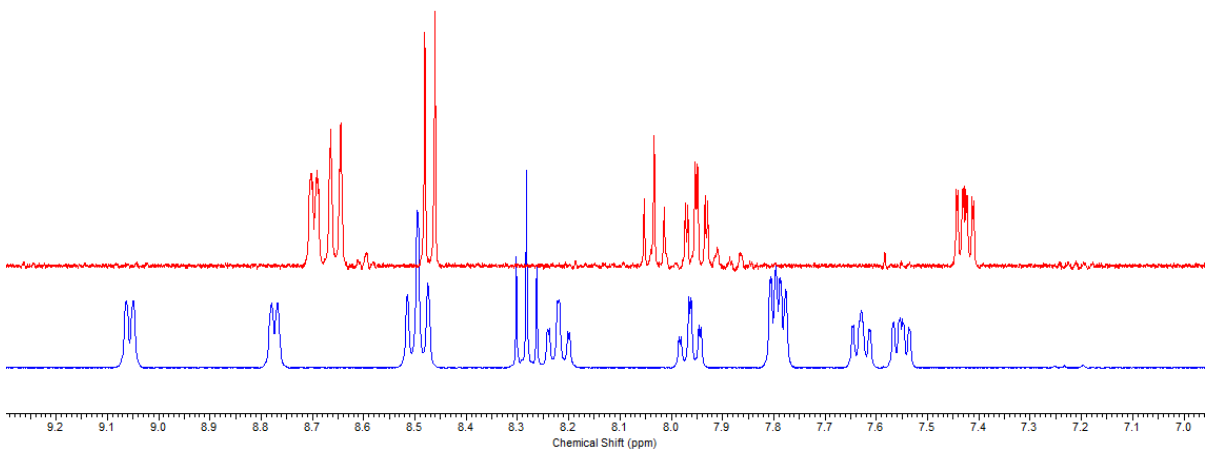


Figure 2.3 The aromatic region of the ^1H NMR spectra for compounds **2.1** (blue) and **2.2** (red), showing the simplification of the spectra upon the conversion from bidentate to terdentate.

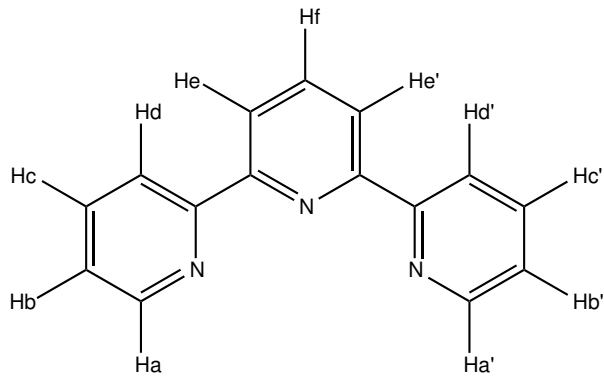


Figure 2.4 Proton-explicit skeletal drawing of 2,2':6',2''-terpyridine.

the other pendant protons.

As in the case of bidentate compounds, modification of the anion has only minor effects on the NMR spectra. This is the expected behaviour, the conjugated pi system and the lack of protons near the modified anion combine to be susceptible in only a minor fashion.

Carbon NMR (^{13}C) was attempted on the complexes as well. Unfortunately, Re^I complexes perform poorly in ^{13}C NMR experiments, the signal to noise ratio is incredibly

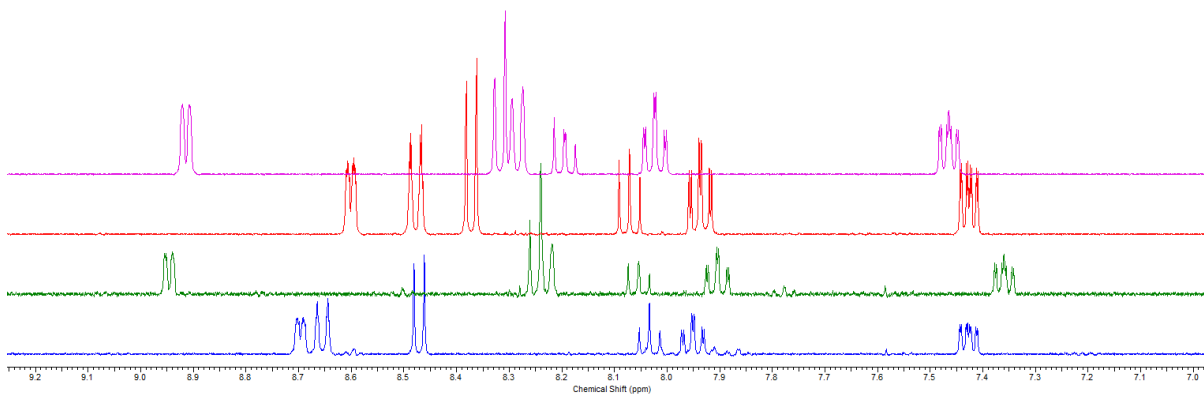


Figure 2.5 The aromatic region of the ^1H NMR spectra for compounds **2.2** (blue), **2.4** (green), **2.6** (red) and **2.8** (purple).

poor (if a signal is even visible). The effect of this is a lack of ^{13}C NMR analysis of these compounds in literature, with very few exceptions.¹²⁷ Extensive efforts included use of a 500 MHz spectrometer, with 1664 scans to produce the best example, seen in Figure 2.6, with average peak signal to noise ratio (s/n) of only 4 - 5.

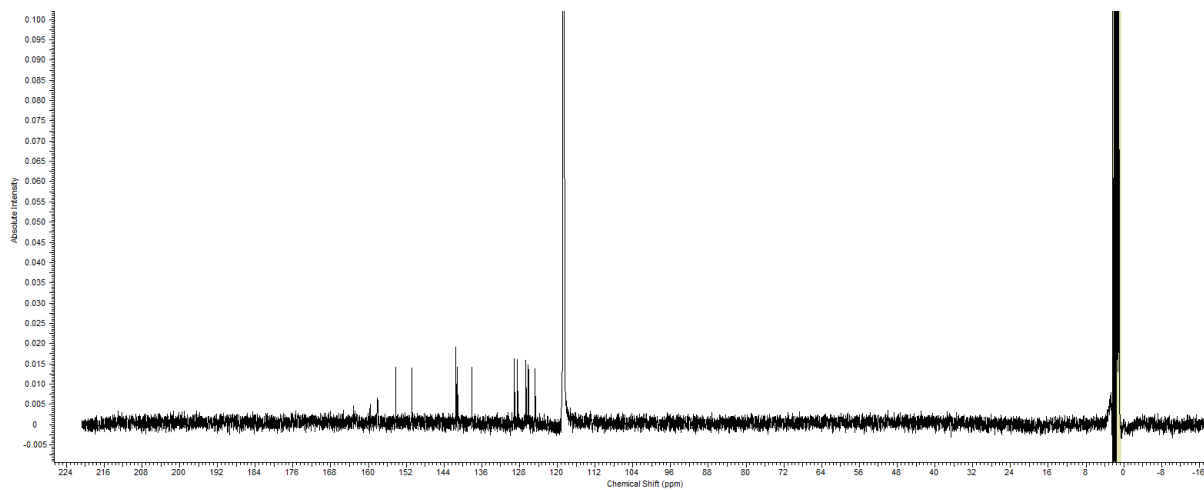


Figure 2.6 The ^{13}C NMR spectra of **2.1**. Spectra for other compounds could not be collected.

2.3.2 Structure Analysis with X-Ray Crystallography and DFT

Single crystal analysis by x-ray crystallography yielded good structures of compounds **2.1**, **2.2**, **2.3**, **2.5**, and **2.8**. These are the first reported crystal structures of the κ^3 terdentate Re^I compounds. A number of structural characteristics are common between the various bidentate or terdentate complexes. Much analysis has been done on the structures of bidentate complexes in literature^{128–130} the notable characteristic within terpyridine compounds is the rotation of the pendant arm, pushing the nitrogen atom away from the plane of the metal-ligand bonds by approximately 100°. Cell parameters and other collection data for compounds **2.1**, **2.3**, **2.5**, and **2.7** are located in Table 2.1.

Table 2.1 Crystal data and structure refinement for compounds **2.1**, **2.3**, and **2.5**

Compound	2.1	2.3	2.5
Empirical formula	C ₁₉ H ₁₁ N ₃ O ₃ ReCl	C ₁₉ H ₁₁ N ₃ O ₃ ReBr	C ₂₀ H ₁₁ N ₄ O ₃ Re
Formula weight (g/mol)	538.96	583.41	530.04
Temperature (K)	200	200	200
Wavelength (Å)	0.71073	0.71073	0.71073
Crystal System	Triclinic	Monoclinic	Triclinic
Space Group	P-1	C2/c	P-1
a (Å)	9.8736(4)	31.1537(7)	9.9196(9)
b (Å)	14.8202(4)	7.1176(2)	14.9902(14)
c (Å)	16.3472(4)	16.8519(4)	16.5187(15)
α (deg)	69.2890(10)	90.000	68.363(2)
β (deg)	80.801(2)	111.0230(10)	80.929(2)
γ (deg)	79.836(2)	90.000	79.975(2)
Volume (Å ³)	2190.00(12)	3488.00	2236.6(4)
Z, r (calc) (Mg/m ³)	2, 1.997	8, 2.222	2, 1.927
Absorption coefficient (mm ⁻¹)	6.063	9.282	5.821
Absorption correction	Semi-empirical from equivalents		
Final R indices [I≥2σ(I)]	R1 = 0.0397, wR2 = 0.0839	R1 = 0.0232, wR2 = 0.0614	R1 = 0.0390, wR2 = 0.0921
R indices (all data)	R1 = 0.0604, wR2 = 0.0951	R1 = 0.0285, wR2 = 0.0642	R1 = 0.0500, wR2 = 0.0961

In addition, the structures of all species were geometry optimized at the first principles DFT level, with the B3LYP exchange-correlation functional^{131,132} using the Gaussian 09

quantum chemistry package.¹³³ The LanL2DZ basis set/effective core potential was used on Re,¹³⁴ and the all-electron TZVP basis set for the remaining lighter atoms.¹³⁵ These are popular basis set and functional choices for computational chemistry, owing to their reasonable accuracy with decent computational speed,¹³⁶ although they are not without their faults.¹³⁷ Frequency analysis of all structures was used to confirm the nature of the stationary points. Solvent effects were computed when necessary using the integral equation formalism variant of the Polarizable Continuum Model (PCM) for solvation within Gaussian 09.^{138,139} The results of these calculations are compared to the x-ray crystallography data in Tables 2.3 to 2.7.

The crystal structure of **2.3** had a higher symmetry than the other samples. Details on the exact methods used for structure elucidation are available in section A.3. All of the structures found are of high quality. The structures of **2.1**, **2.3**, and **2.5** can be seen in Figure 2.7. More views of these structures can be seen in Appendix section A.3. Crystals suitable for x-ray analysis were unable to be collected from compound **2.7**.

Selected bond lengths, bond angles, and torsion angles are listed in Table 2.3, Table 2.4 and Table 2.5 for products **2.1**, **2.3**, and **2.5** respectively. The experimental results agree closely with the computed values for all samples. The structures can be seen in Figure 2.7a, Figure 2.7b and Figure 2.7c, and more views of these structures can be seen in Appendix B, X-ray Crystal Structures.

The Re^I centre in the pseudo-octahedral complex is supported by a planar, pincer coordinated ligand defined by the terminal and central pyridyl group of the terpyridine. One of the carbonyl groups lies in this plane trans to the central pyridyl group, while the remaining carbonyl groups and the anionic group or other complexed species lie on an approximately perpendicular plane to the ligand. Bond angles around the Re centre show a significant deviation of up to 15° from the ideal octahedral geometry for all samples

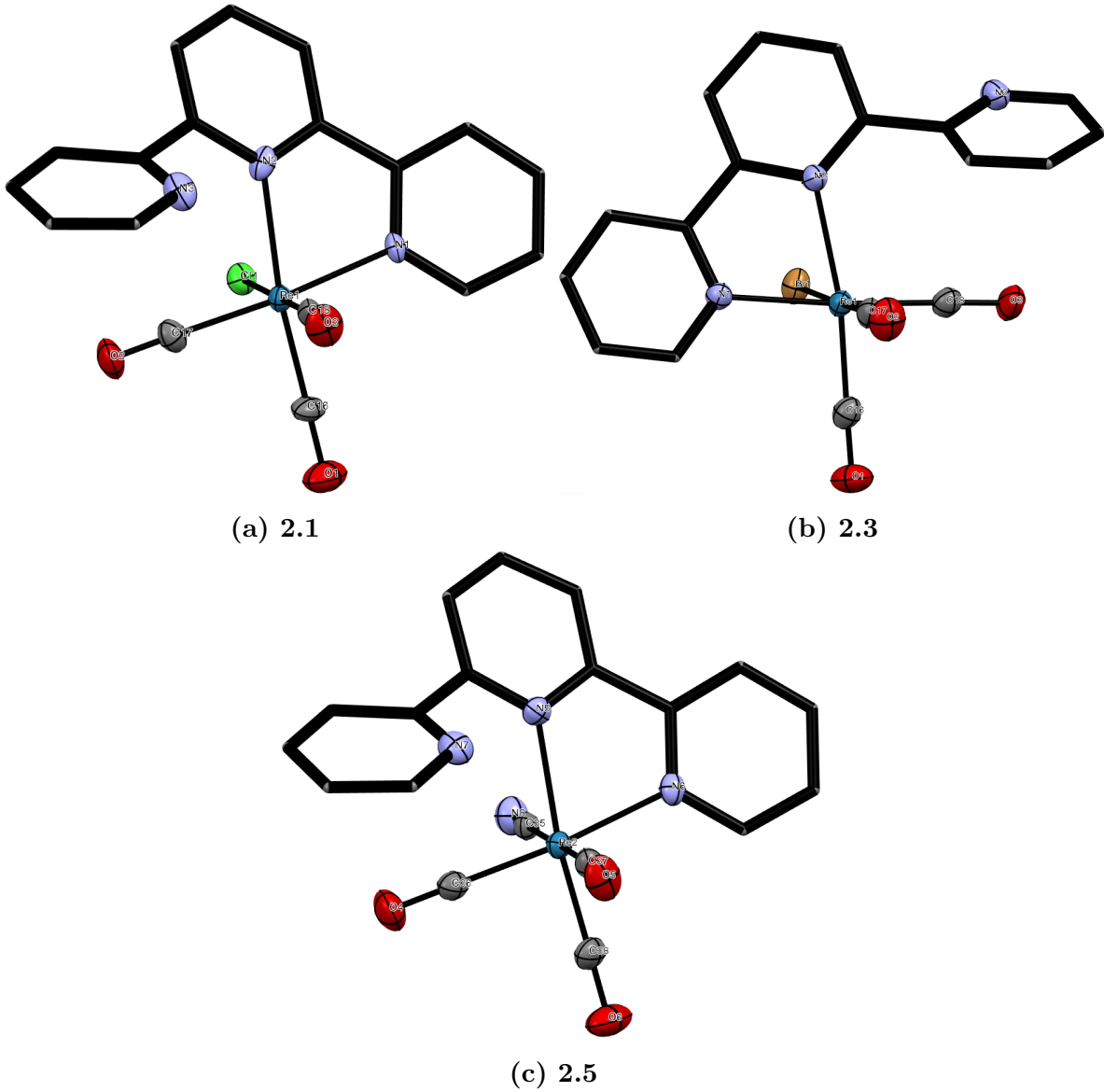


Figure 2.7 X-ray crystal structure representation for **2.1**, **2.3**, and **2.5**. Co-crystallized chloroform, hydrogen atoms, and thermal ellipsoids of ligand carbon atoms are omitted for clarity.

analyzed. The typical N-Re-N bond angle of 75° is due to the atomic size of rhenium, comparison to the crystal structure of an analogous compound with a manganese atom¹⁴⁰ shows a decrease in the bonding angle for the Re complex by approximately 4° due to an increase of bond length from metal to nitrogen of about 0.12 \AA for both the central

and terminal pyridines.

The deviation from octahedral is further visible in the rotation of the X-Re-CO plane (X=halide, anion, or other complexed group) by approximately 10 degrees from the right angle relative to the plane of the ligand. The axial halide, anion, or chelated group typically occupies a position slightly departed from the perpendicular, angled to be over the ligand. The reason for the eclipsing is unknown, as no steric interference exists at that site, and analysis of electrostatic or other short-range electronic effects computationally show any interaction between this site and the aromatic rings. In Re^I complexes, the halide or anion is located axial relative to the plane of the ligand. For the acetonitrile complex with triflate counterion, the acetonitrile occupies the axial position. This site occupation holds through the complete set of x-ray crystal structures with a κ^2 -(bipy)Re(CO)₃X core structure motif deposited in the Cambridge Crystallography Data Centre (CCDC) database,¹⁴¹ and extends through other α -diimine complexes seen in our lab and in literature.⁷³

Table 2.2 Solvated and gas phase energy differences between Axial & Trans geometries of κ^x -(terpy)-Re(CO)_{5-x}CN (x=2,3)

Bidentate		Terdentate	
E(gas) ^a	E(solution) ^b	E(gas) ^a	E(solution) ^b
14.70	11.87	16.28	16.43

^a B3LYP SCF energy in kcal/mol.

^b B3LYP SCF energy in kcal/mol, with
PCM solvation in acetonitrile.

The crystal structure for compound **2.5** contains two molecules per unit cell, one of which is solved to have the cyano group in the position trans to the ligand. However, careful analysis of the bond lengths, angles, and torsion data in Table 2.5 shows a remarked similarity between all -CO and -CN groups. Additionally, in an x-ray diffraction pattern, -CN and -CO are difficult to differentiate with certainty. Thus, while the struc-

ture solved to the two isomers, critical analysis would suggest that this molecule does not violate the axial position pattern laid out above. The computed structures energies in Table 2.2 show a favouring of the axial position by 12-16 kcal/mol in the gas phase and by PCM in a simulated acetonitrile solvent.

Selected bond lengths, bond angles, and torsions are listed in Table 2.3, Table 2.4 and Table 2.5 for products **2.1**, **2.3**, and **2.5** respectively.

Table 2.3 Selected Distances, Angles, and Torsions for **2.1**.

Bond	Distance (Å)	
	Experimental	Calculated
Re(1)-C(16)	1.89(1)	1.91
Re(1)-C(17)	1.934(8)	1.94
Re(1)-C(18)	1.90(1)	1.92
Re(1)-N(1)	2.162(6)	2.20
Re(1)-N(2)	2.236(9)	2.29
Re(1)-Cl(1)	2.496(2)	2.52
C(16)-O(1)	1.16(1)	1.15
C(17)-O(2)	1.12(1)	1.15
C(18)-O(3)	1.15(1)	1.16
Angle	Degrees (°)	
	Experimental	Calculated
C(16)-Re(1)-C(17)	87.6(4)	86.9
C(16)-Re(1)-C(18)	88.3(4)	90.6
C(17)-Re(1)-C(18)	87.3(4)	89.6
C(16)-Re(1)-N(1)	96.4(3)	96.2
C(17)-Re(1)-N(1)	174.9(3)	175.6
C(18)-Re(1)-N(1)	95.9(3)	93.5
C(16)-Re(1)-N(2)	169.3(3)	170.4
C(17)-Re(1)-N(2)	101.1(3)	102.8
C(18)-Re(1)-N(2)	98.3(3)	89.4
N(2)-Re(1)-N(1)	74.5(3)	74.1
C(16)-Re(1)-Cl(1)	91.7(3)	91.4
C(17)-Re(1)-Cl(1)	91.7(3)	94.8
C(18)-Re(1)-Cl(1)	179.9(3)	175.3
N(1)-Re(1)-Cl(1)	84.0(2)	82.0
N(2)-Re(1)-Cl(1)	81.6(2)	87.8
O(1)-C(16)-Re(1)	179.6(9)	178.2
O(2)-C(17)-Re(1)	176.0(8)	176.9
O(3)-C(18)-Re(1)	177.3(9)	179.3
Torsion	Degrees (°)	
	Experimental	Calculated
N(1)-C(5)-C(6)-N(2)	16(1)	15
N(2)-C(10)-C(11)-N(3)	41(1)	139

Table 2.4 Selected Distances, Angles, and Torsions for **2.3**.

Bond	Distance (\AA)	
	Experimental	Calculated
Re(1)-C(16)	1.911(3)	1.92
Re(1)-C(17)	1.890(3)	1.92
Re(1)-C(18)	1.921(4)	1.94
Re(1)-N(1)	2.173(3)	2.20
Re(1)-N(2)	2.232(2)	2.29
Re(1)-Br(1)	2.6410(4)	2.68
C(16)-O(1)	1.150(4)	1.15
C(17)-O(2)	1.157(4)	1.15
C(18)-O(3)	1.155(5)	1.16
Angle	Degrees ($^\circ$)	
	Experimental	Calculated
C(16)-Re(1)-C(17)	89.1(1)	90.8
C(16)-Re(1)-C(18)	85.9(1)	86.8
C(16)-Re(1)-N(1)	97.9(1)	96.0
C(17)-Re(1)-N(1)	92.5(1)	93.6
C(18)-Re(1)-N(1)	175.4(1)	175.6
C(16)-Re(1)-N(2)	171.2(1)	170.3
C(17)-Re(1)-N(2)	96.0(1)	89.4
C(18)-Re(1)-N(2)	101.3(1)	102.9
N(1)-Re(1)-N(2)	74.7(1)	74.3
C(16)-Re(1)-Br(1)	92.7(1)	90.4
C(17)-Re(1)-Br(1)	177.6(1)	176.1
C(18)-Re(1)-Br(1)	91.6(1)	94.1
N(1)-Re(1)-Br(1)	85.74(7)	82.6
N(2)-Re(1)-Br(1)	82.07(7)	88.8
O(1)-C(16)-Re(1)	178.6(3)	178.3
O(2)-C(17)-Re(1)	179.5(3)	179.4
O(3)-C(18)-Re(1)	179.9(3)	176.8
Torsion	Degrees ($^\circ$)	
	Experimental	Calculated
N(1)-C(6)-C(1)-N(2)	-15.4(4)	-15
N(2)-C(5)-C(11)-N(3)	141.1(3)	136

Table 2.5 Selected Distances, Angles, and Torsions for **2.5**.

Axial CN			Planar CN		
Bond	Distance (Å)		Bond	Distance (Å)	
	Exp.	Calc.		Exp.	Calc.
Re(2)-C(35)	2.148(7)	2.14	Re(1)-C(19)	2.105(8)	1.99
Re(2)-C(36)	1.926(6)	1.94	Re(1)-C(16)	1.928(5)	2.09
Re(2)-C(37)	1.954(7)	1.97	Re(1)-C(18)	1.96(1)	2.01
Re(2)-C(38)	1.902(9)	1.92	Re(1)-C(17)	1.918(7)	1.90
Re(2)-N(5)	2.242(7)	2.29	Re(1)-N(1)	2.253(5)	2.32
Re(2)-N(6)	2.168(5)	2.20	Re(1)-N(2)	2.176(4)	2.19
C(35)-N(8)	1.138(9)	1.16	C(19)-O(3)	1.17(1)	1.15
C(36)-O(4)	1.145(8)	1.15	C(16)-N(4)	1.149(7)	1.16
C(37)-O(5)	1.151(9)	1.15	C(18)-O(2)	1.14(1)	1.14
C(38)-O(6)	1.17(1)	1.15	C(17)-O(1)	1.130(8)	1.16
Angle	Degrees (°)		Angle	Degrees (°)	
	Exp.	Calc.		Exp.	Calc.
C(36)-Re(2)-C(38)	87.7(3)	87.2	C(16)-Re(1)-C(17)	87.8(3)	90.2
C(36)-Re(2)-C(37)	88.0(3)	89.9	C(16)-Re(1)-C(18)	87.0(3)	84.8
C(36)-Re(2)-C(35)	92.1(3)	93.4	C(16)-Re(1)-C(19)	92.5(3)	88.4
C(38)-Re(2)-C(37)	88.5(3)	91.0	C(17)-Re(1)-C(18)	88.7(3)	88.4
C(38)-Re(2)-C(35)	90.8(3)	91.6	C(17)-Re(1)-C(19)	90.5(3)	87.7
C(37)-Re(2)-C(35)	179.2(3)	175.9	C(18)-Re(1)-C(19)	179.1(3)	172.2
C(36)-Re(2)-N(5)	100.6(3)	102.6	C(16)-Re(1)-N(1)	102.2(2)	98.1
C(36)-Re(2)-N(6)	174.2(3)	175.7	C(16)-Re(1)-N(2)	175.9(2)	172.0
C(38)-Re(2)-N(5)	169.3(3)	170.1	C(17)-Re(1)-N(1)	168.3(3)	170.5
C(38)-Re(2)-N(6)	96.6(3)	96.2	C(17)-Re(1)-N(2)	95.9(3)	97.5
C(37)-Re(2)-N(5)	98.4(2)	89.4	C(18)-Re(1)-N(1)	97.7(3)	88.5
C(37)-Re(2)-N(6)	96.0(2)	92.6	C(18)-Re(1)-N(2)	94.8(3)	93.4
C(35)-Re(2)-N(5)	82.3(2)	87.5	C(19)-Re(1)-N(1)	83.2(2)	96.3
C(35)-Re(2)-N(6)	83.9(2)	84.0	C(19)-Re(1)-N(2)	85.7(2)	93.9
N(5)-Re(2)-N(6)	74.7(2)	74.0	N(1)-Re(1)-N(2)	73.9(2)	73.7
O(6)-C(38)-Re(2)	179.4(7)	178.0	O(1)-C(17)-Re(1)	178.2(7)	177.6
O(5)-C(37)-Re(2)	175.5(6)	179.4	O(2)-C(18)-Re(1)	172.0(7)	176.4
N(8)-C(35)-Re(2)	178.0(6)	176.4	O(3)-C(19)-Re(1)	178.0(6)	176.6
O(4)-C(36)-Re(2)	179.0(7)	177.3	N(4)-C(16)-Re(1)	178.7(6)	178.1
Torsion	Degrees (°)		Torsion	Degrees (°)	
	Exp.	Calc.		Exp.	Calc.
N(5)-C(20)-C(25)-N(6)	14.5(9)	14	N(1)-C(1)-C(6)-N(2)	12.5(8)	15
N(5)-C(24)-C(30)-N(7)	41(1)	136	N(1)-C(5)-C(11)-N(3)	43.7(9)	137

Structural comparisons between the bidentate samples and the terdentate show many similarities. The loss of one carbonyl always accompanies the chelation of the pendant arm of the ligand. The increased coordination forces the ligand to adopt a more rigidly planar geometry, this is visible in the structure of **2.2** (Figure 2.8a) and **2.8** (Figure 2.8b). Suitable crystals for x-ray analysis were unable to be collected for the remaining complexes.

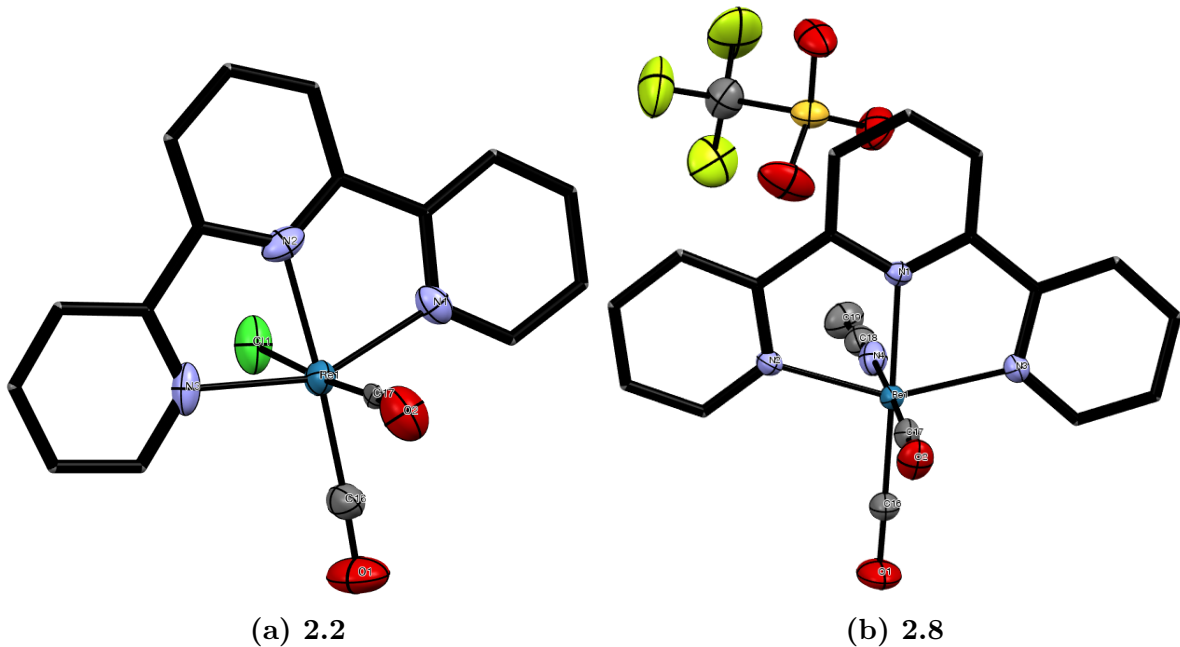


Figure 2.8 X-ray crystal structure representation for **2.2** and **2.8**. Co-crystallized chloroform, hydrogen atoms, and thermal ellipsoids of ligand carbon atoms are omitted for clarity.

Selected bond lengths, bond angles, and torsions are listed in Table 2.6 and Table 2.7 for products **2.2** and **2.8**. Cell parameters and collection data can be found in Table 2.8.

Both **2.2** and **2.8** structures are pseudo-octahedral in geometry, with *mer* coordinated terpyridine ligand. The carbonyl groups and chloride/acetonitrile form a plane approximately perpendicular to the ligand. As in the κ^2 -bidentate samples discussed above, the carbonyls occupy the equatorial and one axial position relative to the ligand,

and the chloride or acetonitrile occupy the remaining axial position. The N-Re-N bond angles remain approximately 75°, and the central pyridyl N to chloride or acetonitrile angle is still approximately 80-85°.

Comparisons between the κ^2 -bidentate and κ^3 -terdentate samples (**2.1** and **2.2**) highlight the geometrical changes experienced in the thermolysis reaction. The distance from Re to the central pyridyl N has shortened from 2.24 to 2.08 Å. This bond shortening of 0.16 Å signifies increased metal-ligand interaction. This comes at the expense of decreased interaction with the carbonyl groups, with the bond to the planar CO increasing from 1.89 to 1.93 Å and the axial CO bond increasing from 1.901 to 1.975 Å. As the carbonyls experience less π backbonding from the metal, the internal C-O bond shortens by as much as 0.1 Å.

The κ^3 -terdentate samples (**2.2** and **2.8**) provide the opportunity to analyse both neutral and cationic species. Due to the weakly coordinated triflate anion in **2.8**, a number of geometric differences arise compared to **2.2**. While the ligand is coordinated by only 0.01 - 0.02 Å closer to the metal atom, the carbonyl groups are 0.04 - 0.1 Å closer, indicating their increased electron donation to the electron poor metal centre. As well, the C-O bonds in the carbonyls are 0.03 - 0.12 Å longer, indicating the increased π backbonding occurring in the cation.

Table 2.6 Selected Distances, Angles, and Torsions for **2.2**.

Bond	Distance (Å)	
	Experimental	Calculated
Re(1)-C(16)	1.926(9)	1.92
Re(1)-C(17)	1.975(10)	1.91
Re(1)-N(1)	2.119(7)	2.13
Re(1)-N(2)	2.080(7)	2.09
Re(1)-N(3)	2.126(7)	2.13
Re(1)-Cl(1)	2.489(3)	2.53
N(1)-N(3)	4.14(1)	4.15
C(16)-O(1)	1.14(1)	1.16
C(17)-O(2)	1.05(1)	1.16
Angle	Degrees (°)	
	Experimental	Calculated
C(16)-Re(1)-C(17)	91.5(4)	89.2
C(16)-Re(1)-N(2)	173.7(4)	172.0
C(17)-Re(1)-N(2)	94.6(3)	98.8
C(16)-Re(1)-N(1)	103.9(3)	103.0
C(17)-Re(1)-N(1)	92.7(3)	93.4
N(2)-Re(1)-N(1)	77.3(3)	76.7
C(16)-Re(1)-N(3)	101.8(3)	103.0
C(17)-Re(1)-N(3)	91.7(3)	93.4
N(2)-Re(1)-N(3)	76.6(3)	76.7
N(1)-Re(1)-N(3)	153.7(3)	153.2
C(16)-Re(1)-Cl(1)	91.8(3)	89.1
C(17)-Re(1)-Cl(1)	176.5(2)	178.3
N(2)-Re(1)-Cl(1)	82.1(2)	82.9
N(1)-Re(1)-Cl(1)	85.4(2)	87.0
N(3)-Re(1)-Cl(1)	88.7(2)	87.0
O(1)-C(16)-Re(1)	177.9(9)	179.1
O(2)-C(17)-Re(1)	173.2(8)	179.2
Torsion	Degrees (°)	
	Experimental	Calculated
N(1)-C(5)-C(6)-N(2)	1(1)	2
N(2)-C(10)-C(11)-N(3)	-4(1)	-2

Table 2.7 Selected Distances, Angles and Torsions for Acetonitrile Adduct of **2.8**.

Bond	Distance (\AA)	
	Experimental	Calculated
Re(1)-C(16)	1.889(4)	1.93
Re(1)-C(17)	1.885(3)	1.93
Re(1)-N(1)	2.091(3)	2.10
Re(1)-N(2)	2.135(3)	2.15
Re(1)-N(3)	2.131(3)	2.15
Re(1)-N(4)	2.160(3)	2.15
N(2)-N(3)	4.138(4)	4.18
C(16)-O(1)	1.170(4)	1.16
C(17)-O(2)	1.171(4)	1.15
Angle	Degrees ($^\circ$)	
	Experimental	Calculated
C(16)-Re(1)-C(17)	87.69(16)	88.1
C(16)-Re(1)-N(1)	175.95(12)	176.1
C(17)-Re(1)-N(1)	96.35(12)	95.8
C(16)-Re(1)-N(3)	103.81(13)	103.6
C(17)-Re(1)-N(3)	94.03(12)	92.3
N(1)-Re(1)-N(3)	76.20(10)	76.3
C(16)-Re(1)-N(2)	103.58(13)	103.6
C(17)-Re(1)-N(2)	93.73(12)	92.3
N(1)-Re(1)-N(2)	75.99(10)	76.3
N(3)-Re(1)-N(2)	151.77(11)	152.5
C(16)-Re(1)-N(4)	90.50(14)	88.5
C(17)-Re(1)-N(4)	178.10(12)	176.6
N(1)-Re(1)-N(4)	85.46(10)	87.6
N(3)-Re(1)-N(4)	86.94(10)	88.5
N(2)-Re(1)-N(4)	86.15(10)	88.5
O(1)-C(16)-Re(1)	179.1(3)	178.8
O(2)-C(17)-Re(1)	178.0(3)	178.9
Torsion	Degrees ($^\circ$)	
	Experimental	Calculated
N(1)-C(1)-C(6)-N(2)	1.7(4)	1
N(1)-C(5)-C(11)-N(3)	-1.8(4)	-1

Table 2.8 Crystal data and structure refinement for compounds **2.2** and **2.8**

Compound	2.2	2.8
Empirical formula	C ₁₈ H ₁₁ N ₃ O ₂ ReCl	C ₂₁ H ₁₄ N ₄ O ₅ F ₃ SRe
Formula weight (g/mol)	510.95	665.61
Temperature (K)	200	200
Wavelength (Å)	0.71073	0.71073
Crystal System	Triclinic	Triclinic
Space Group	P-1	P-1
a (Å)	8.5275(3)	8.5745(4)
b (Å)	14.2421(5)	11.9805(5)
c (Å)	17.4637(6)	13.0970(5)
α (deg)	77.948(2)	79.748(2)
β (deg)	85.684(2)	81.106(2)
γ (deg)	79.890	88.091(2)
Volume (Å ³)	2041.79(12)	1307.99(10)
Z, r (calc) (Mg/m ³)	4, 2.050	2, 1.993
Absorption coefficient (mm ⁻¹)	6.494	5.094
Absorption correction	Semi-empirical from equivalents	
Final R indices [I≥2σ(I)]	R1 = 0.0636, wR2 = 0.1018	R1 = 0.0294, wR2 = 0.0673
R indices (all data)	R1 = 0.0985, wR2 = 0.1110	R1 = 0.0366, wR2 = 0.0700

2.3.3 Infra-Red Spectroscopy

Conversion of bidentate to terdentate species was confirmed utilizing Fourier Transform Infrared (FTIR) spectroscopy. A small sample of powder product was placed on the Agilent Cary 630 FTIR spectrometer, with a 2 cm⁻¹ resolution. The instrument is fitted with a diamond ATR for solid sample analysis. Spectra are the Fourier transform of 16 scans for each sample.

Analysis of the results in Figure 2.9 shows the significant reduction of one peak in the ca. 2100 cm⁻¹ region. This peak is in the CO stretching frequency, the frequency of the peak lost in thermolysis is indicative of a weakly coordinated carbonyl group. A splitting occurs for the other large peak and its shoulder in the conversion from bidentate

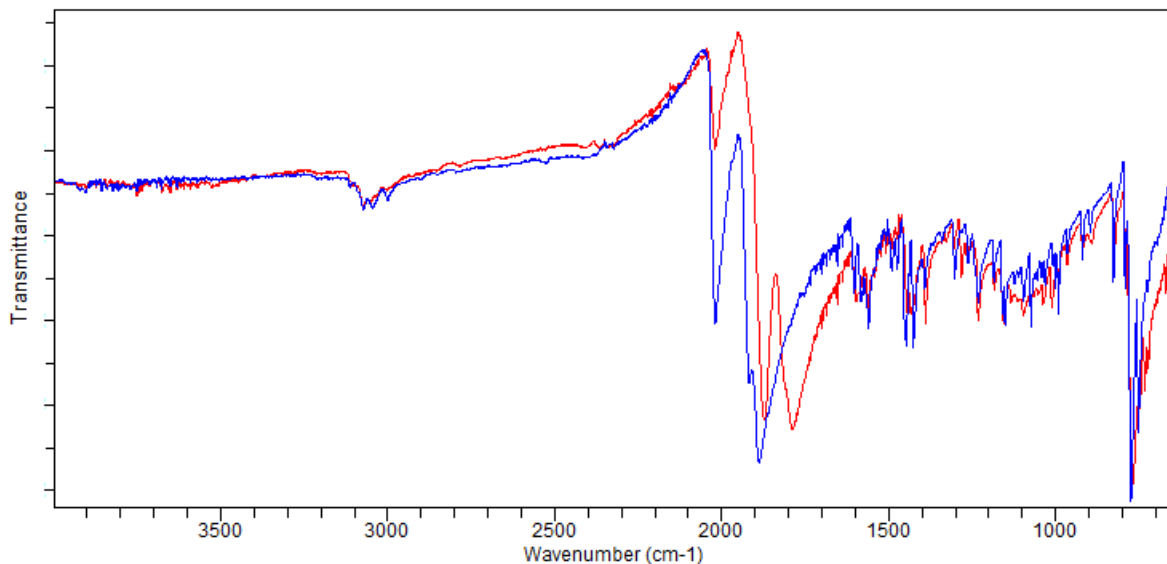


Figure 2.9 FTIR Spectra for complexes **2.1** (blue) and **2.2** (red).

to terdentate, from 1890 to 1790 cm⁻¹, indicating the further weakening of the metal carbonyl bonds remaining in the complex. This weakened bond is likely the carbonyl co-planar to the ligand, analysis of the x-ray crystal structure shows the CO bond to be 0.1 Å longer than that of the axial carbonyl. This identification is supported by the DFT methods discussed below.

FTIR spectra were predicted using molecular frequency calculations of DFT optimized structures. Prediction of this spectra was performed as a verification of the optimized structures discussed in subsection 2.3.2 above. The calculation identifies stretching or bending harmonic energies in optimized structures. The computed spectra in Figure 2.10 shows three peaks for **2.1**, at 2094, 2012, and 1990 cm⁻¹. The relative location of these peaks corresponds to those seen in Figure 2.10 for **2.1**, but are shifted by approximately 100 cm⁻¹ to higher energy relative to the experimental. This is characteristic of DFT calculations, which usually over-report frequencies by approximately 0.96 for B3LYP calculations.¹⁴² Similarly, for **2.2**, peaks are seen at 2000 and 1950 cm⁻¹,

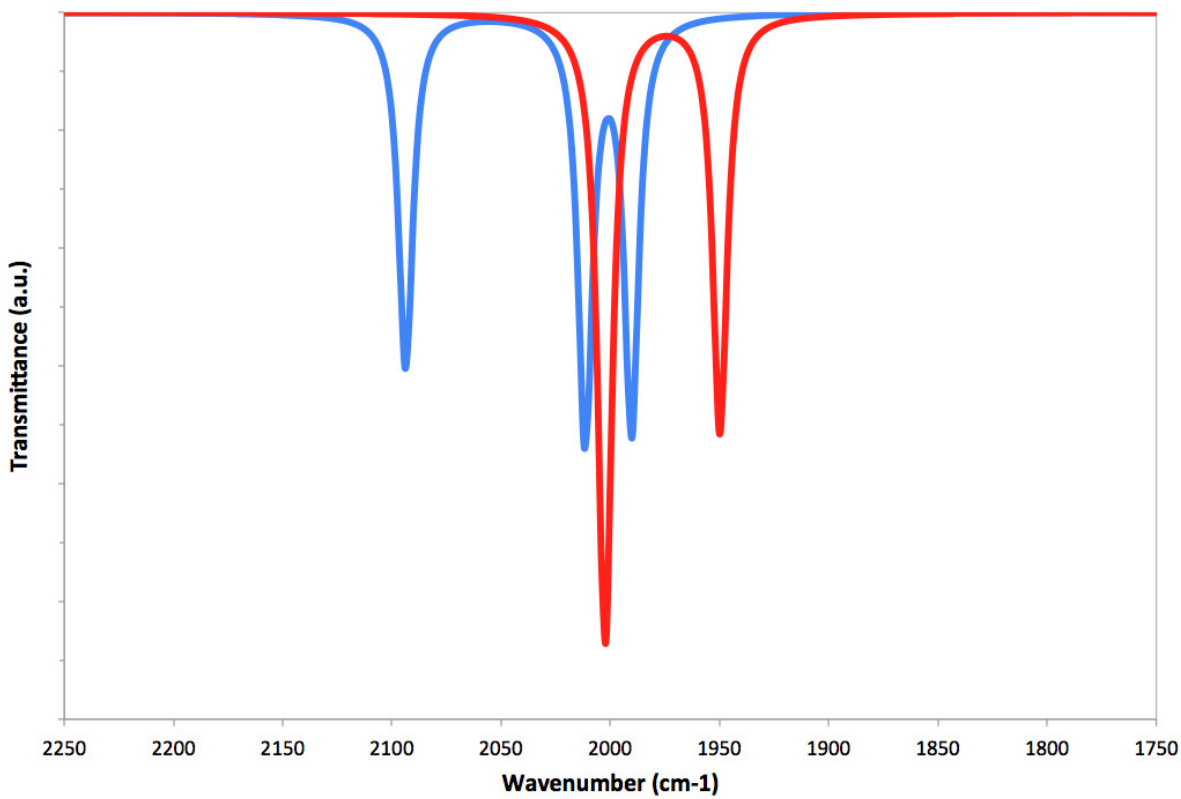


Figure 2.10 DFT predicted FTIR spectra for **2.1** (blue) and **2.2** (red).

compared to the 1890 and 1790 cm^{-1} peaks seen experimentally. This computed value reflects the shift to lower energy carbonyl stretching from **2.1** to **2.2**, and echoes the experimental spectra well.

Further analysis of other spectra were not successful in identification of any additional molecular properties, with the exception of a series of strong peaks appearing in the 1200-1300 cm^{-1} range for samples **2.7** and **2.8**, confirming the presence of the triflate anion from the $-\text{SO}_3^-$ group vibrations (Figure 2.11). Additionally, the small peak present at 2270 cm^{-1} in the terdentate sample corresponds to the weakly coordinated acetonitrile occupying the molecule's axial position.

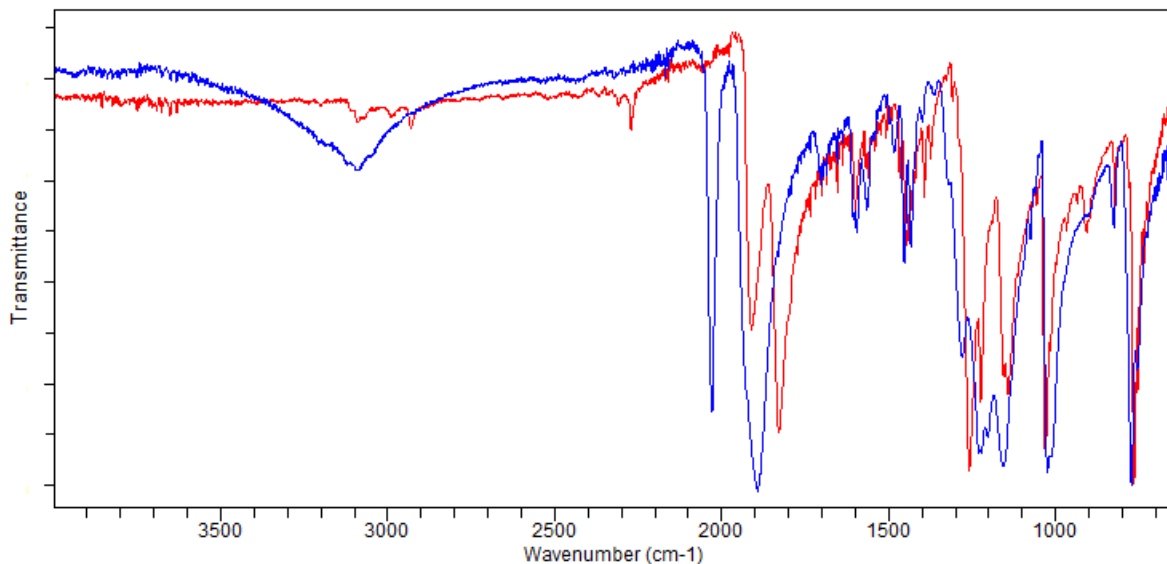


Figure 2.11 FTIR Spectra for complexes **2.7** (blue) and **2.8** (red).

2.3.4 Photophysical Properties

A striking observation upon the conversion of the bidentate species into the terdentate complexes is that these new compounds have a substantially darker colour that reflects a significant change in the photophysical properties. This effect was investigated using a combination of UV-visible spectroscopy and DFT modelling. Spectra were collected on a Agilent Cary 5000 UV-Vis-NIR Spectrophotometer. The stronger absorbance of the terdentate complexes compared to the bidentate precursors is evident in the UV-Vis spectra of these species, and is presented in Figure 2.12 and Figure 2.13. These spectra were obtained in Dimethylsulfoxide (DMSO) with approximate concentrations of 0.01 mM for bidentate, and an order of magnitude lower (0.001 mM) for the terdentate analogues. The terdentate complexes have more intense absorbance for higher energy ligand UV-based $\pi-\pi^*$ transitions (<400 nm) and certainly a richer visible absorption profile that involve the $d-\pi^*$ transitions. These features are responsible for the colour change observed.

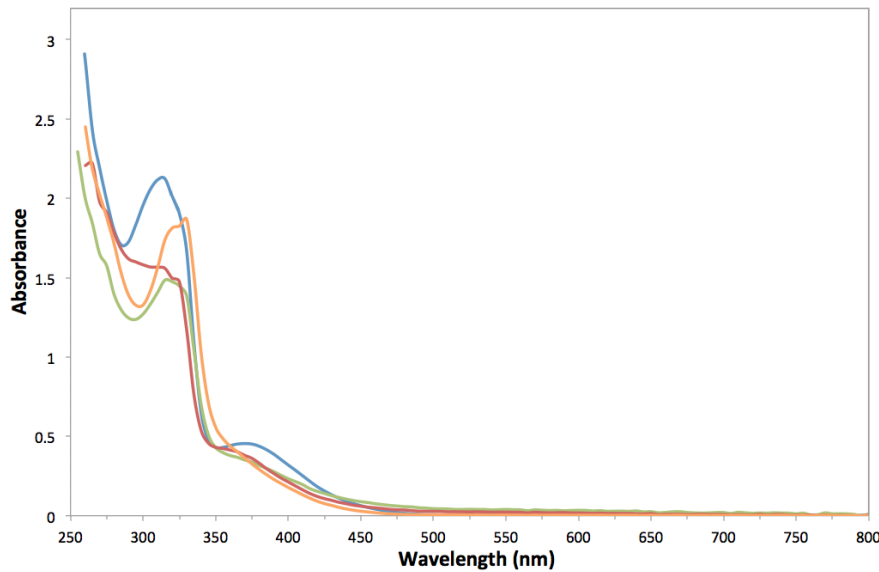


Figure 2.12 UV-Vis spectra for compounds **2.1** (blue), **2.3** (green), **2.5** (red), and **2.7** (orange) at 0.01 mM concentration.

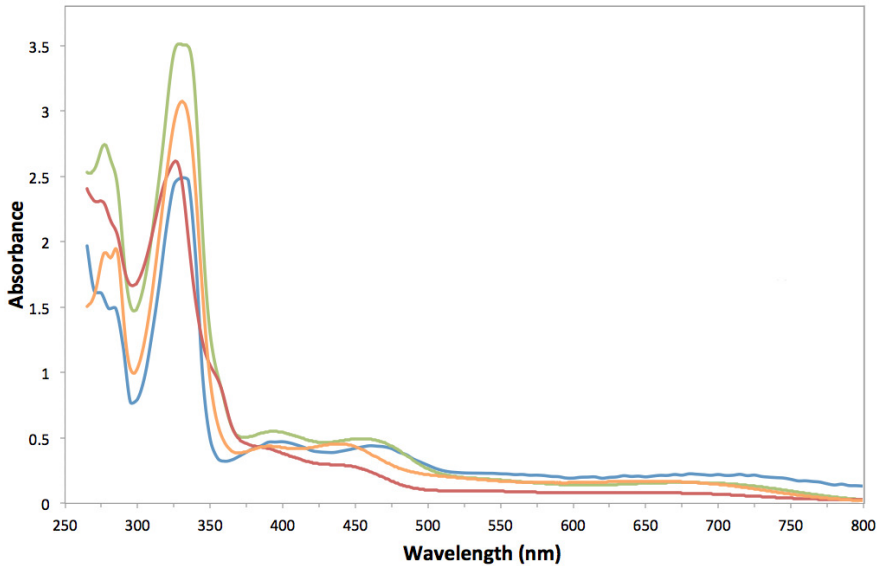


Figure 2.13 UV-Vis spectra for compounds **2.2** (blue), **2.4** (green), **2.6** (red), and **2.8** (orange) at 0.001 mM concentration.

The UV-Vis spectra were modelled using TD-DFT computations within Gaussian 09, using the B3LYP functional with the LanL2DZ basis set and effective core potentials for the rhenium atom, and the TZVP basis set for all lighter atoms. Solvent was simulated

using the integral equation formalized variant of the PCM solvation model, with DMSO as the solvent.

The resulting computed spectra were excellent matches to the experimental spectra. The similarity of the spectra between the bidentate species and as well as the terdentate species indicates that parallel electronic transitions appear within these two groups. Specifics will be discussed for the chloro compounds, **2.1** and **2.2**, but strong parallels exist for all species. Plots of experimental and computational data for these two complexes are presented in Figure 2.14 and Figure 2.15, respectively.

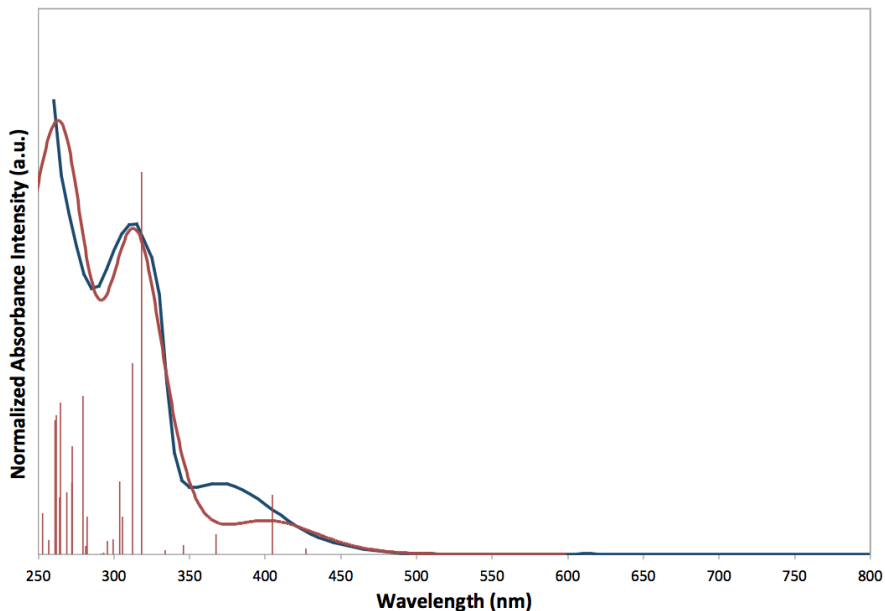


Figure 2.14 Plots of the experimental and computed UV-Vis spectra for compound **2.1**. The blue curve shows experimental result. The red vertical lines show the calculated transitions and relative intensities from the TD-DFT calculations, while the red curve shows the gaussian convolution with peak width at half height of 0.250 eV.

Common to all bidentate compounds were peaks at wavelengths of 315-320 nm, and peak shoulders near 350-375 nm (Figure 2.12). In the case of **2.1**, the computational results suggest that the experimental band centred at $\lambda = 315\text{-}320\text{ nm}$ ($31750\text{-}31250\text{ cm}^{-1}$) primarily arises from two electronic transitions. The first is from HOMO-3 to LUMO,

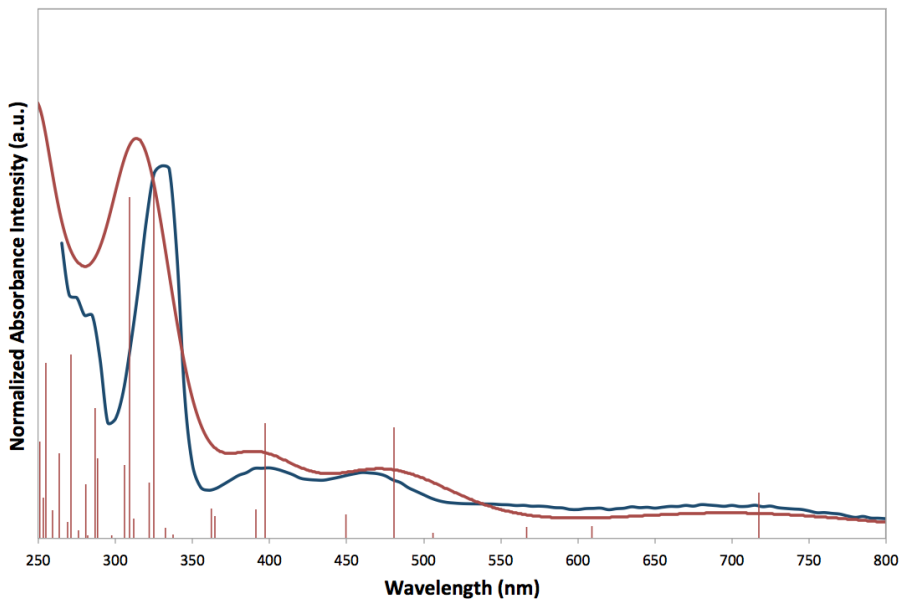


Figure 2.15 Plots of the experimental and computed UV-Vis spectra for compound **2.2**. The blue curve shows experimental result. The red vertical lines show the calculated transitions and relative intensities from the TD-DFT calculations, while the red curve shows the gaussian convolution with peak width at half height of 0.250 eV.

a $\pi-\pi^*$ transition, while the second major contribution is the excitation from HOMO to LUMO+2, which is a $d-\pi^*$ transition. The TD-DFT calculations suggest that the experimental band centred at $\lambda = 370$ nm (27030 cm^{-1}) corresponds to a calculated transition at approximately 400 nm, that is a $d-\pi^*$ (HOMO-1 to LUMO) absorbance. Computed plots of molecular orbitals are included in Appendix C, Molecular Orbitals Diagrams, Figures C.1 to C.8.

Like the bidentate samples, the spectra for the terdentate samples are quite similar to one another. In general, all of these species have much higher absorbance coefficients than their bidentate analogues; all contain long trailing absorptions across the wavelengths analysed. For terdentate complex **2.2**, the four experimentally observed UV-Vis absorptions observed are made up of six computed transitions. The computational model provided two equal and strong transitions appearing at 308 and 325 nm to

generate the experimental band centred at $\lambda = 330$ nm (30300 cm^{-1}). These arise from a transition from HOMO-5 to LUMO, a Cl lone-pair to terpy π^* orbital absorption, and from HOMO-3 to LUMO, which is a ligand centred $\pi-\pi^*$ transition. All of the lower energy transitions are dominated by MLCT bands. The experimental band centered at $\lambda = 400$ nm (25000 cm^{-1}) arises from an electronic transition from HOMO to LUMO+3 which is $d-\pi^*$ in nature. The absorbance centred at $\lambda = 460$ nm (21740 cm^{-1}) corresponds to two MLCT $d-\pi^*$ transitions; HOMO-2 to LUMO and HOMO-1 to LUMO+1. Finally, the broad experimental band 680-715 nm ($14700\text{-}14000\text{ cm}^{-1}$) arises from the electronic transition appearing at 718 nm, which is the excitation of a d -electron in the Re-centered HOMO to the ligand π^* LUMO.

2.3.5 Fluorescence

Fluorescence data was collected for **2.1** and **2.2** using an Agilent Cary Eclipse Fluorescence Spectrophotometer, using a 5 nm excitation slit and emission slit, using excitation wavelengths selected to correspond to the centre of UV-Vis absorption bands. Data was collected for spectra in N,N-dimethylformamide (DMF) to simulate the photocatalytic reaction environment (see chapter 3). Spectra are shown in Figure 2.16 for **2.1** and **2.2** with their UV-Vis absorption spectra for comparison. Data is normalized to equal concentration for each sample in fluorescence and absorbance.

Clearly the transformation from bidentate terpyridine to terdentate ligand has significant effect on the interactions of these Re compounds with visible light. While the terdentate sample is excited at various wavelengths (that should correspond to different absorption bands), the emission appears to be from one single band centred at ca. 485 nm. An emission band appears similarly in bidentate, centred at 480 nm, with a second, broad, weaker band appearing centred around 600 nm. The sharp peak observed at 420 nm is

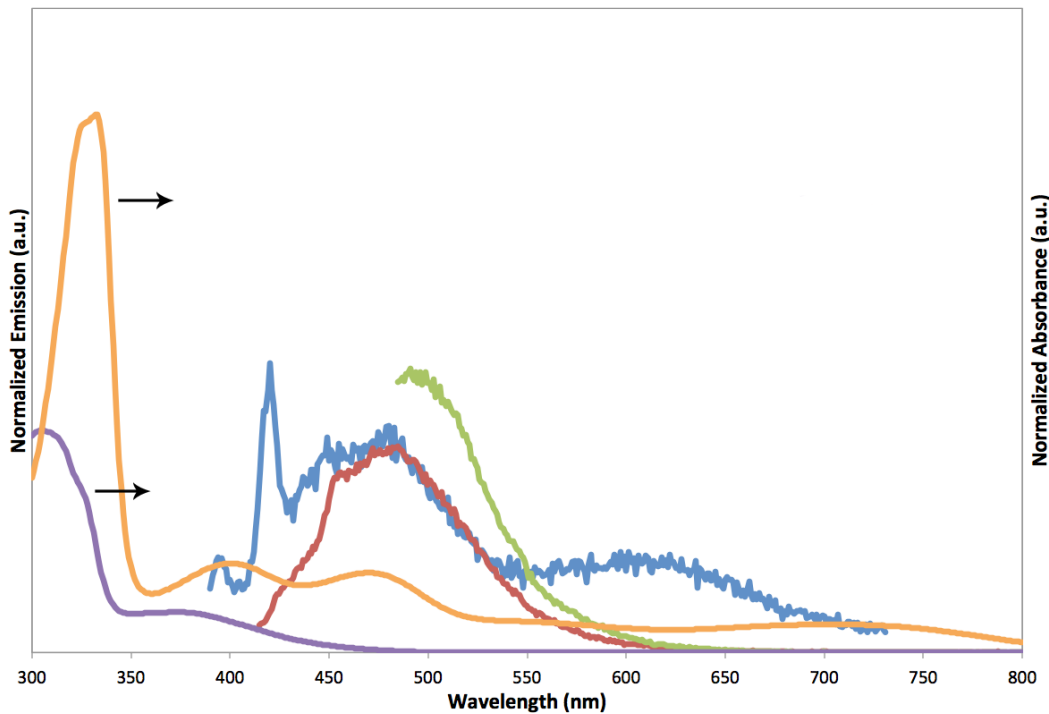


Figure 2.16 UV-Vis and fluorescence spectra for **2.1** and **2.2**. Fluorescence of **2.1** from excitation of 373 nm (blue), excitation of **2.2** by 400 nm (red) and 470 nm (green) are shown, along with the absorption spectra of **2.1** (purple) and **2.2** (orange).

present in the DMF solvent blank as well.

Interestingly, emission is not seen with the naked eye with 400 nm excitation for the terdentate, while emission from the bidentate emission is a very strong, white light. This may be due to self-absorbance in the terdentate samples, emission of 490 nm is easily absorbed by the molecule. In the bidentate, no absorbance bands correspond with emission bands shown, these appear to the naked eye as a white emission.

2.4 Conclusions

This work reported the first crystallographically authenticated rhenium(I) terpyridine terdentate complexes and thus expanded upon the prior limitations of Re coordina-

tion complexes. These terpyridine complexes are accessed via a simple, highly efficient, solid-state thermolysis pathway. They expand upon the known α -diimine photophysical properties, with enhanced metal to ligand, $d-\pi^*$ electronic transitions, occurring more frequently and with lower energy than in the associated bidentate compounds. These observations are supported by computational TD-DFT results, affording an expanded understanding of the transition bands. Modification of the bidentate and terdentate species has been shown, the synthetic success of a triflate moiety should facilitate further development of reactivity and provides an opportunity for synthetic and catalytic studies.

Chapter 3

Photocatalysis of CO₂

3.1 Introduction

Only 6 years after the photophysical properties of Re^I complexes using 2,2'-bipyridine were characterized,⁴⁶ Hawecker, Lehn, and Ziessel showed the effectiveness of the compound for the photocatalytic reduction of CO₂.⁶⁶ Since then, many have shown the efficacy of a wide range of α -diimino complexes for the reaction^{67,130,143} and expansion of the systems to bimetallic complexes with ruthenium and osmium as electron transfer agents has produced a wide range of results.^{112,116,144} The mechanism of reduction has been subject of some debate: while mechanisms have been proposed since Lehn et. al. soon after their original publication,⁶⁷ modifications have been submitted routinely over the past decades.^{87,116,117,145–149}

The development of a novel terdentate geometry and the associated increase in photon absorption at lower energies of the catalyst warranted investigation of the CO₂ reduction capabilities, having overcome the criticism of only absorbing high energy photons.¹²⁰ The terdentate complexes were tested and compared to the bidentate, and to the previously proven catalyst $\kappa^2(\text{bipy})\text{Re}(\text{CO})_3\text{Cl}$.

3.2 Photocatalytic Reactions with New Compounds

The photocatalytic cycle is, simply, a photon-induced MLCT, followed by the extraction of an electron from a sacrificial reductant. This negatively charged radical species sheds the halide anion, opening up a reaction site. Reduction of CO₂ yields any number of CO, H₂O, formate (HCO₂⁻), or bicarbonate (CO₃H⁻), depending on the mechanistic pathway (see Scheme 4.1). Further discussion and a proposal of a new mechanism geometry based on computational and experimental data can be read in chapter 4.

3.2.1 Conditions

Reaction conditions in use in literature have remained typically unchanged since the original papers. A mixture of DMF with either Triethanolamine (TEOA) or Triethylamine (TEA) at a 5:1 ratio is used to make a 1.0 mM solution of catalyst, with ‘excess’ (depending on reference, a 1.1 to 25 molar ratio) electrolyte salt (typically Et₄NX or *t*-Bu₄NX, where X = halide from catalyst) added as a stabilizer. Solutions are degassed by bubbling of CO₂ and a pure CO₂ headspace is left to form over the solution. The reaction of 4 mL of catalyst solution in a 30 mL sealed glass vial is monitored via Gas Chromatography (GC) analysis of the headspace, using a HP gas chromatograph with a 15 m CARBONPLOT column with 0.320 mm inner diameter and 1.50 μm film in a 40 °C oven. The instrument is fitted with a Thermal Conductivity Detector (TCD), and, while using He as a carrier gas, is able to resolve CO and CO₂ completely.

3.2.2 Experimental Results

Both bidentate and terdentate κ^n (terpy)Re(CO)_{5-n}X (n=2, 3) **2.1** and **2.2** complexes show no activity for CO₂ reduction. Modification of testing time, light source, product

analysis methods, solvent, sacrificial reductant, pH, presence of electrolyte, presence of H₂O, or variation of anion (X=Cl, Br, OTf, CN) shows no change of this inactivity. Testing of κ^2 (bipy)Re(CO)₃Cl under the same reaction and testing conditions shows production of approximately 6 mL CO from CO₂ (20% conversion) in 1 hour of photolysis with visible ($\lambda > 400$ nm) light, verifying the method and isolating the particular catalysts as the ineffective species.

3.2.3 Rationalization of Results

The lack of reactivity of the κ^2 (terpy)Re(CO)₃X motif of complexes contrasting to the activity of the originally published κ^2 (bipy)Re(CO)₃X indicates significant influence of the ligand on the reaction. Kurz *et al.* demonstrated the requirement for fluorescence for successful catalytic candidates.¹³⁰ The explanation for this is the requirement for a stable, long-lasting excited state, with lifetime greater than that of the timescale of the electron abstraction from the sacrificial amine. Observed fluorescence demonstrates the lack of non-radiative relaxation pathways, considered to be an analogue for the extended lifetime of the excited state. Sample **2.2** shows only poor fluorescence (see chapter 2, subsection 2.3.5). While the complex is able to absorb light across the spectrum, and has HOMO to LUMO transitions with high enough energyⁱ for the catalyzed reduction of CO₂ to CO, it appears as if the catalysis is not initiated due to a short excited state lifetime.

Explanation for the lack of CO production observed in the attempted photochemical reduction of CO₂ by bidentate sample **2.1** and others must come from some other area. These samples are quite fluorescent, emission from the powder sample can be seen with the naked eye with simulation by a 405 nm laser pen under ambient light environments.

ⁱElectrochemical reduction of CO₂ in similar environments takes 1.7-2.1 V, equivalent to HOMO-LUMO transitions from 590-750 nm.¹⁵⁰

Other substituted bipyridine ligands are known to be active for photocatalytic reduction,^{67,130} thereby suggesting the most likely conflicting feature of the terpyridine ligand to be the pendant arm itself.



Figure 3.1 A photograph of fresh (left) and aged (right) catalyst mixtures, showing the change from yellow to red in 5 days.

Importantly, two clues come from the reaction mixture: under intense visible light in the presence of CO_2 the compound bleaches from bright yellow (see the left vial, Figure 3.1) to a very faint yellow-green. Colour does not return after storage in the dark, bubbling of new CO_2 , or other manipulations. Secondly, a mixture of sacrificial amine, DMF, and catalyst **2.1** in ratios identical to what is required in the reaction mixture changes colour from a yellow to a deep red irreversibly after approximately five days at ambient conditions, as shown in Figure 3.1.

The most likely cause for the bleaching of the solution is the disassociation of terpyridine ligand from the metal centre. The colours seen in the catalyst are all due to metal-ligand interaction, and the UV-Vis spectrum of free terpyridine in solution is located solely in the UV range ($\lambda^{\max} \approx 285 \text{ nm}$).¹⁵¹ The labilization can be a photoinduced process.¹⁵²

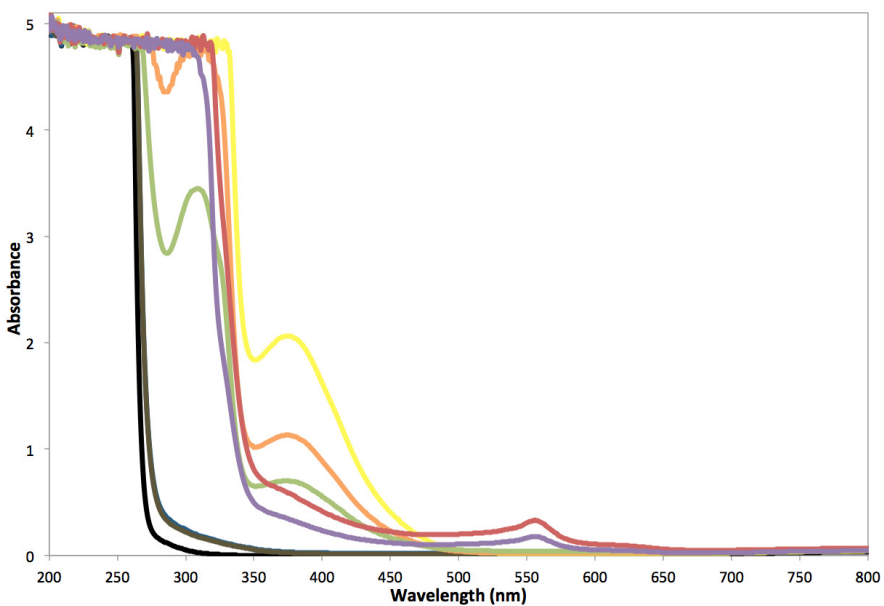
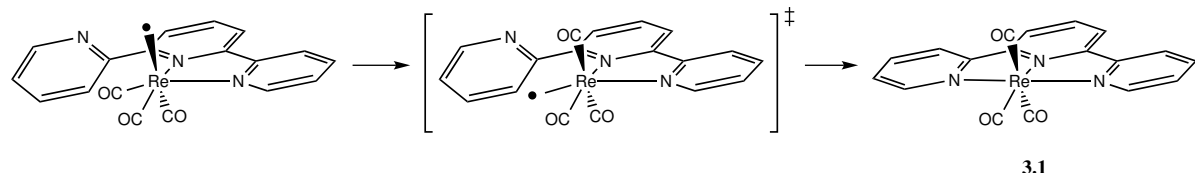


Figure 3.2 UV-Visible spectra of freshly prepared and aged catalyst mixture. DMF, DMF-TEOA (5:1), and DMF-TEOA + Et_4NCl (1 mM) are shown in black, blue and olive, respectively. Fresh catalyst is shown in yellow (1 mM catalyst), orange (0.5 mM) and green (0.25 mM). Aged catalyst is shown in red (1 mM) and purple (0.5 mM).

The UV-visible spectra was obtained for the red compound formed after 5 days of ageing, showing some distinctive modifications (see Figure 3.2). A peak appears at ca. 560 nm, and the metal to ligand $d-\pi^*$ peak at 470 nm is reduced. Additionally, the fresh catalyst has a valley in the spectrum at ca. 285 nm, while the aged sample does not and in fact has increased adsorption at energies above 310 nm.

Other complexes may be formed that deactivate the catalyst, including the forma-



Scheme 3.1 Formation of **3.1** from catalytic excimer via reorganization of carbonyls and chelation of the pendant arm.

tion of a cationic tridentate tricarbonyl complex, seen in Scheme 3.1. This species can be formed by the rearrangement of the carbonyl ligands from the *fac* orientation to a *mer*, migration of one carbonyl to the open site axial to the ligand achieves this reorganization. Once the *mer* species is formed, the open site on the metal centre is oriented towards the pendant arm of the terpyridine ligand, coordination of that group to the metal centre results in compound **3.1**. The UV-Visible spectra of this species is not isolated, however, DFT predicted UV-Vis is shown in Figure 3.3, and compared to the experimental red product, these spectra do not correlate. This reorganization may still occur in the reactant solution, but it does not appear to be the primary deactivation pathway.

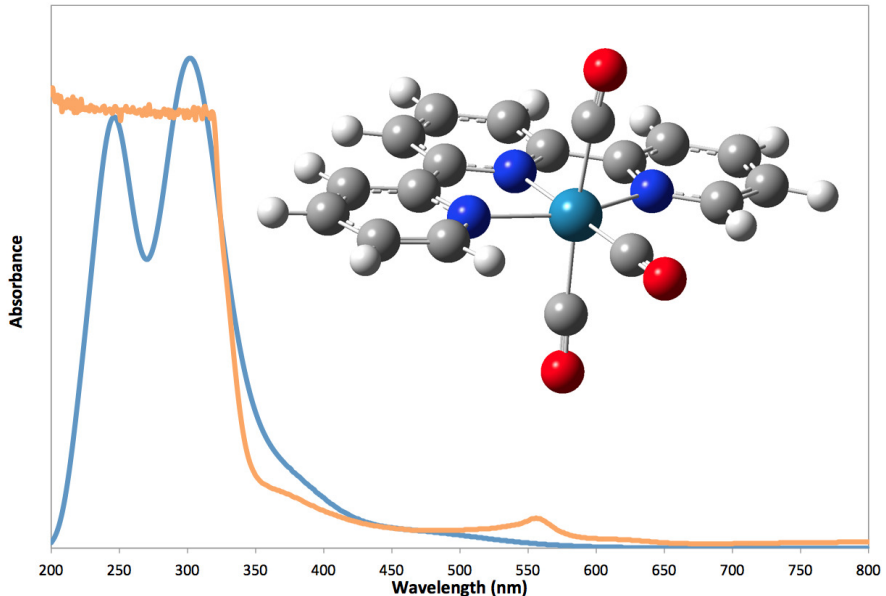


Figure 3.3 Computational structure (inset) and predicted UV-Vis absorption spectra of $[\kappa^3\text{-(terpy)-Re}(\text{CO})_3]^+$ and experimental spectra of the aged catalytic mixture (orange).

Another deactivation product may be the formation of triethanolamine-catalyst adducts.¹²⁷ In the presence of DMF, TEOA has been shown to bind to the open site of the excimer via the amine's oxygen atom. This is susceptible to insertion of CO_2 to form a $-\text{OC(O)C}-$

$\text{CH}_2\text{CH}_2\text{N}(\text{CH}_2\text{CH}_2\text{OH})_2$ group. DFT studies on these two compounds suggest that they may be a coloured species, with predicted UV-Vis showing lower energy absorption than the catalyst itself (a red shift), demonstrated in Figure 3.4. The experimental red mixture UV-Vis spectra is overlaid, showing lack of correlation to the Ishitani compounds.

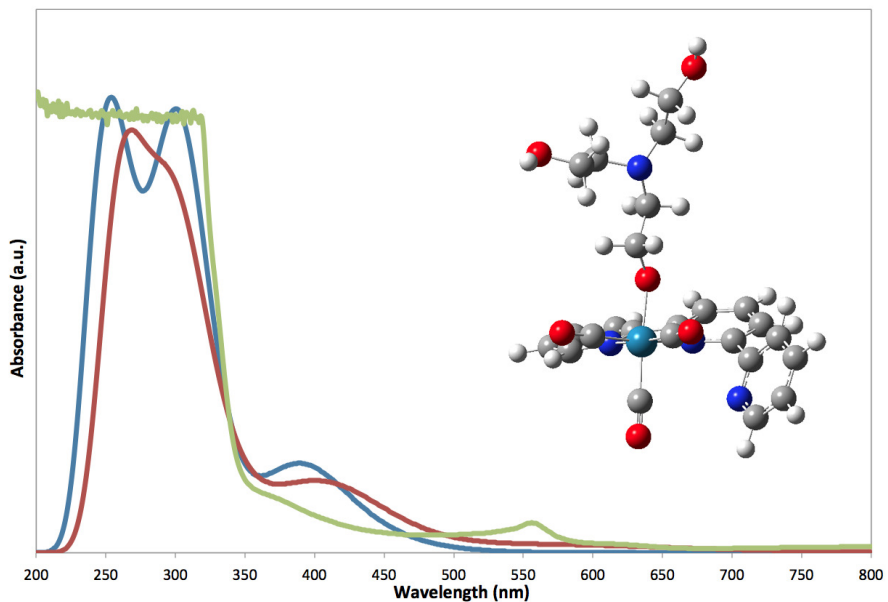


Figure 3.4 Computational structure (inset) and DFT predicted UV-Vis absorption spectra for **2.1** (blue), the TEOA complex proposed by IshitaniFigure 3.4 (red), and experimental spectra of the aged catalytic mixture (green).

Neither the tricarbonyl terdentate nor the Ishitani complexes correlate to the observed spectra in Figure 3.2. Identification of a compound solely by its spectra is not possible, however, some characteristics could be predicted. It is likely that there is a significant modification of the environment around the metal centre, previous observed electronic transitions that occur at that energy are due to metal d to ligand π^* interactions. Ligand π to π^* transitions appear at much higher energy, and modification of those interactions could explain the lack of valleys observed in the UV region (at 285 nm). Further determination of the complex is not possible with the collected data.

Attempts to isolate this red compound were unsuccessful. It appears to be highly soluble in the reaction mixture, not allowing for isolation via solvent extraction. DMF and TEOA are high-boiling point solvents, any attempts to remove solvent via distillation (even at low pressure) required temperatures approaching the thermolysis temperature for synthesis of the terdentate compounds. Further investigation is required to isolate the product.

3.3 Conclusions

Experimental data shows the inactivity of these catalysts for photoreduction of CO₂ under a range of experimental conditions. These same conditions show conversion using κ^2 (bipy)Re(CO)₃Cl as the photoreductant, signifying the validity of experimental setup. The inactivity may be due to formation of inactive side-products or ligand labilization (for the case of bidentate catalyst) or due to the short excited state lifetime of the terdentate catalyst.

Catalyst mixtures appear to form a new compound after ageing. Although isolation was not achieved, this red product was investigated via UV-Vis spectroscopy, the spectra was compared to DFT calculated spectra for two potential deactivation products. The spectra do not align, suggesting that the red product is some as of yet unknown compound.

Chapter 4

Mechanism of CO₂ Reduction

4.1 Introduction

Within two years of the appearance of the originally reported bipyridine rhenium (I) catalyst, experimental studies on the mechanism of the photocatalytic reduction of CO₂ were available in the literature.^{70,120} Studies continue on the mechanism up to the present day,^{68,116,145,153–158} utilizing new investigative techniques as they become available to elucidate transition states and transient intermediates *in situ*.

The mechanistic studies performed analyze CO₂ reduction both photocatalytically and electrocatalytically on Re compounds. The electrocatalytic activity was demonstrated by Hawecker *et. al.* only a year after the photochemistry first appeared.¹⁵⁹ Both methods involve similar cycles, and have been treated interchangeably by some authors.^{145,148,149} The difference between electrocatalytic and photocatalytic methods is the production of the excimer species, not the reduction at the active site. Electrochemical methods have been employed with the hope of utilizing CO₂ and H₂O together for the direct formation of methane and oxygen, however this problem is highly complex and the target remains elusive.^{160,161}

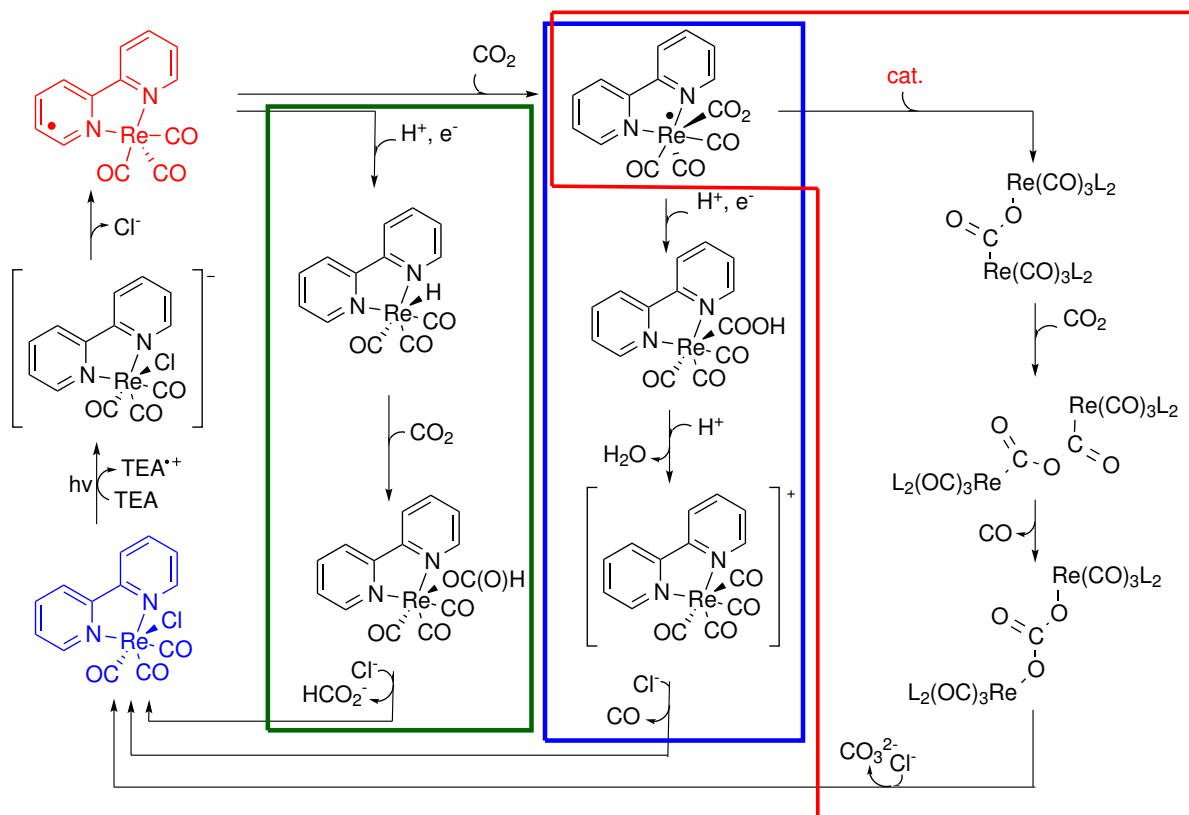
Investigation includes the use of DFT methods to elucidate geometries of intermediates and transition states for the multi-step cycle. Transition metal catalysis is a non-trivial problem computationally, particularly when considering a metal from the lower period. These elements contain a large amount of electrons, many of which can be involved in non-covalent interactions with the ligands and catalyzed products. Obtaining good approximate wave functions for these complex large systems becomes non-trivial and computationally expensive. Likely for this reason, no broad review of the mechanisms of CO₂ reduction by Re^I catalysts, investigated by DFT methods, has ever been made available in the literature.

This section will provide the first complete DFT mechanistic study, from excimer formation, through key intermediates of CO₂ binding and reduction, to the release of products and reformation of the catalyst. Various mechanistic pathways will be investigated, and experimental observations will be considered with the computational results. A new mechanism geometry will be proposed, this tackles previously unexplained properties of the reactions.

4.2 Mechanism Pathways

Prior work in the literature has proposed three general mechanistic pathways for the photoreduction of CO₂.^{68,87,145,155} In general, as seen in Scheme 4.1, these pathways result in the formation of CO and H₂O, formate (HCO₂⁻), or bicarbonate (HCO₃⁻) anions. The formation of bicarbonate proceeds via the formation of a CO₂ bridged dimer that undergoes an insertion reaction to ultimately produce bicarbonate and a molecule of CO. Production of formate requires the formation of a Re-H complex, which undergoes CO₂ insertion. The formation of CO without bicarbonate or formate by-products occurs via the coordination of CO₂ to an open site on the metal, followed by a double proton addition

and the release of a molecule of H_2O prior to the loss of one of the four carbonyl groups to open up the axial site for halide re-coordination. This is essentially the Reverse Water-Gas Shift Reaction (RWGSR), wherein protons are made available from decomposition of the sacrificial amine instead of from the decomposition of H_2 .¹⁶² These three mechanistic pathways will be referred to as the ‘bicarbonate’ mechanism, the ‘formate’ mechanism, and the ‘water-gas shift’ mechanism, respectively.



Scheme 4.1 An overview of the mechanistic pathways of photochemical CO_2 reduction. Catalyst is shown in blue, and the excimer species in red. The bicarbonate mechanism is boxed in red, the formate mechanism in green, and the water-gas shift mechanism in blue.

Each of the mechanistic pathways identified in Scheme 4.1 was studied, using DFT methods. Structures (using 2,2'-bipyridine as the bidentate ligand, and triethylamine as

the sacrificial reductant) were optimized to ground or transition states using TurboMole 6.5 software,^{163,164} with the TPSS meta-GGA XC functional.¹⁶⁵ This functional shows good results with organometallic complexes, while maintaining reasonable calculation times. The B3LYP functional is noted for its underestimating of transition state barriers, a complaint not levelled against TPSS.¹³⁷ The def2-TZVP all electron basis set was used for all atoms.^{135,166} The TurboMole program utilizes a number of algorithms and techniques to significantly speed up the calculation times, without compromising accuracy.^{167–175} Grimme's dispersion correction (version 3) was included in the calculations.¹⁷⁶ Intermediates and transition states were verified by frequency analysis,^{172,177,178} with further verification of transition states by performing dynamic reaction coordinate calculations to determine the Intrinsic Reaction Coordinates (IRCs). The effects of solvation were calculated using the Conductor-like Screening Model (COSMO) implemented in TurboMole,¹⁷⁹ which is a continuum solvation model implicitly surrounding the solute molecule. Code was developed to assist with automating and managing the computational jobs (see chapter 5).

Many of the intermediates have been synthesized in various studies,^{155,180–182} indicating their reasonable stability. While individual portions of the mechanisms have been studied computationally in the past,^{146–148} no overarching study has compared methods relative to each other. Furthermore, while the formation of CO with H₂O is the most anticipated pathway (due to the lack of formation of bicarbonate or formate in most studies), no literature pathway exists to explain the addition of CO₂ to the open site of the radical catalytic species without a three body reaction step (catalyst, CO₂ and H⁺ together) or without formate reorganization. Furthermore, no mechanism proposed thus far explains the ¹²CO to ¹³CO isotopic exchange demonstrated by Lehn's group in 1986.⁶⁷ These reaction features are ignored by the studies, which prefer to focus only on

the reduction of CO₂, starting from the catalyst-CO₂ adducts and ending with release of CO.

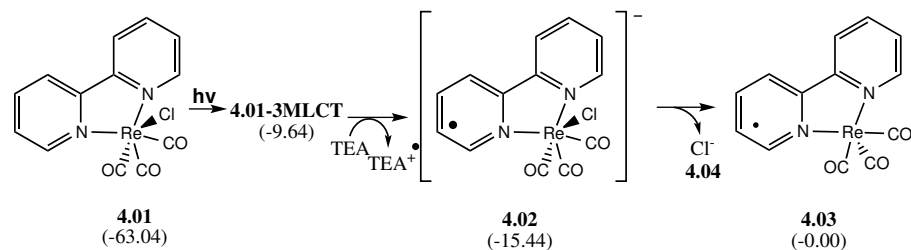
4.2.1 Excimer Formation and Decomposition of the Sacrificial Amine

All of the mechanistic pathways require the formation of a common excimer species, the radical 17e⁻ complex (Scheme 4.2). This occurs through the absorption of an incident photon with enough energy to promote an electron from the metal *d*-orbital to the ligand π^* orbitals of the ground state catalyst, **4.01**, forming the triplet Metal-Ligand Charge Transfer (3-MLCT) complex ³**4.01**^{MLCT}. This excitation requires approximately 50 kcal/mol, sourced from absorbed light. The pseudo-oxidized, electron-deficient metal atom extracts an electron from the sacrificial amine present in the reaction solution to return to the Re^I state (**4.02**). However, this complex is formally a radical anion with the lone electron located in the ligand π system, thus a halide (**4.04**) is lost to return to the neutral radical excimer species in solution, **4.03**. This extraction to form the radical anion catalyst and the radical cation amine is highly endothermic in the gas phase, costing over 80 kcal/mol, but in DMF it is exothermic by 5 kcal/mol. The difference in energies demonstrates the importance of performing calculations in a simulated solution; steps that may have insurmountable energy barriers in the gas phase become possible once solvation is considered.

A modest endothermic dissociation of the chloride (15.44 kcal/mol in DMF) allows for the formation of the triplet 17 e⁻ excimer species **4.03**, from which the pathways discussed in following subsections may diverge.

It is important to note that some studies suggest the solvent coordinates with the excimer species.^{87,158} This solvent coordination is expected to stabilize the excimer species

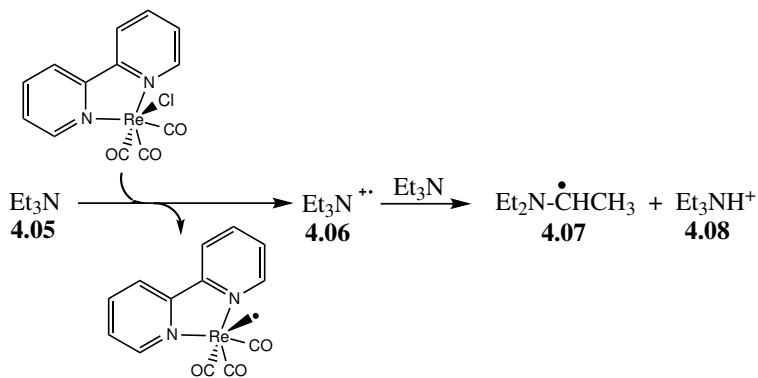
in solution prior to reaction with CO₂.¹⁸³ The coordination provides approximately 11 kcal/mol of stabilization (calculated via DFT). However, this event has no bearing on the overall reaction energies, as the coordination and subsequent loss of solvent is an energetically neutral occurrence and was not examined in detail.



Scheme 4.2 Formation of the excimer species via absorption of a photon and oxidation of the sacrificial amine. Energy in kcal/mol relative to the excimer **4.03** is shown in brackets for each compound.

The decomposition route of the sacrificial amine was first identified by Kalyansundarem in 1978,¹⁶² and is summarized in Scheme 4.3. Although this work showed the decomposition of TEOA, the mechanism for decomposition of TEA is analogous. This decomposition is critical due to the protons it provides to the reaction mixture, and the presence of a simple second electron abstraction from the decomposition product. Upon absorption of a photon by the catalyst, the amine **4.05** is converted to the radical cationic species (Et₃N^{+,•}, **4.06**). This undergoes a proton transfer to a second molecule of the sacrificial reductant. The transfer removes a proton from the carbon α to the central nitrogen, leaving it a neutral radical species (forming **4.07**). This is then able to react in the catalytic cycle to provide a second electron and form the ethene-diethylamino compound **4.26**. Triethylammonium is produced as well (**4.08**), which is a proton source for the formate and water-gas shift mechanistic pathways. This step is slightly exothermic, with energy releases of 1 kcal/mol in gas phase, and nearly 3 kcal/mol in DMF.

Energies of each step of the reaction are listed in Table 4.1. The values show a sig-

**Scheme 4.3** Decomposition pathway for the sacrificial amine.

nificant ‘uphill’ series of steps requiring significant energy input. This energy is supplied by the incident photons; this process is a photocatalyzed activation. The reaction typically requires incident light of 400 nm,⁶⁶ this high energy input allows for the excitation pathway to be followed. The energy of each intermediate and the steps are shown in Figure 4.1.

Table 4.1 Energies for the reaction steps in the photoinduced excimer formation pathway

Steps	Energy(gas) ^a	Energy(dmf) ^b
4.01 → $\text{t}_{\text{ext}}\text{bf}^3\text{4.01MLCT}$	42.81	53.40
4.01 ^{3MLCT} + 4.05 → 4.02 + 4.06	81.45	-5.80
4.02 → 4.03 + 4.04	50.82	15.44
4.06 + 4.05 → 4.07 + 4.08	-1.08	-2.92

^a TPSS energy in kcal/mol.

^b TPSS energy in kcal/mol with COSMO solvation in DMF.

Some small geometry changes occur signifying the change in electron structure in the formation of the excimer species. One metric analyzed in polyaromatic non-innocent ligand redox reactions is the bonding distance between aromatic rings.¹⁸⁴ From ground state, through triplet MLCT complex to the excited radical, the C-C_(bpy) distance decreases from 1.47 Å to 1.42 Å to 1.42 Å respectively. This 0.05 Å decrease is noted in

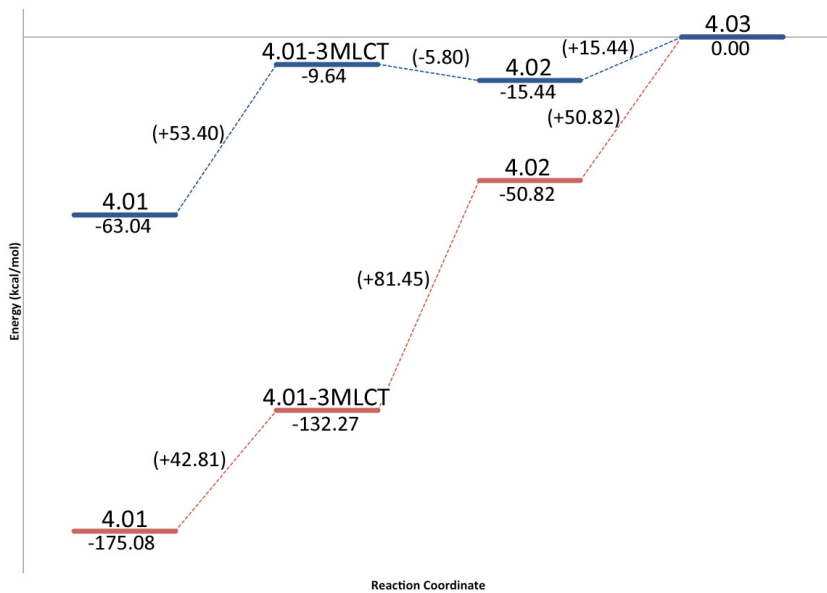


Figure 4.1 Potential Energy Surface for the production of the excimer. Gas phase energies in red, DMF solvated energies in blue. A larger version can be seen in Appendix D, Figure D.2.

many previous experiments and calculations for anion radicals.^{184–188} Other key bond lengths and angles include the ligand N-Re bonds and CO-Re bonds, the addition and subtraction of electrons to and from the complex impact the bonding. As the reaction proceeds, for example, the calculated Re-N distance in solvated structures decreases from 2.19 Å in the ground state catalyst to 2.14 Å in the neutral radical excimer. Similarly, the distance from the metal to the axial carbonyl decreases from 1.92 to 1.89 Å in the same circumstances. Bond length changes of 0.05 Å are large enough to demonstrate a change has occurred in the electron configuration around the metal centre.

4.2.2 The ‘Bicarbonate’ Pathway

The bicarbonate pathway is shown in the orange box in Scheme 4.1, with details shown in Scheme 4.4, starting from the excimer species. This pathway has been studied in the

literature, but many details of the mechanism have not yet been explored. Typical computational analysis consists of investigation from the formed CO₂ linked dimer, through the release of CO, terminating at the carbonate linked dimer. Studies typically build the dimer as a tri-molecular step, or start with a Re–Re bound catalyst dimer and the insertion of CO₂.¹⁴⁸ However, the formation of the [L₂Re(CO)₃]₂ is exceptionally slow in the presence of solvent, with a rate constant 8 orders of magnitude below the formation of the solvent-stabilized radical •L₂Re(CO)₃(solv) complex,¹⁸³ and the [L₂Re(CO)₃]₂ dimer is considered completely unreactive to CO₂.¹⁴⁵

Table 4.2 shows the potential energy change in each step of the reaction. The potential energy diagram is shown in Figure 4.3. The computed intermediate and transition state structures are shown in Figure 4.2.

Table 4.2 Energies for the reaction steps in the ‘carbonate’ pathway

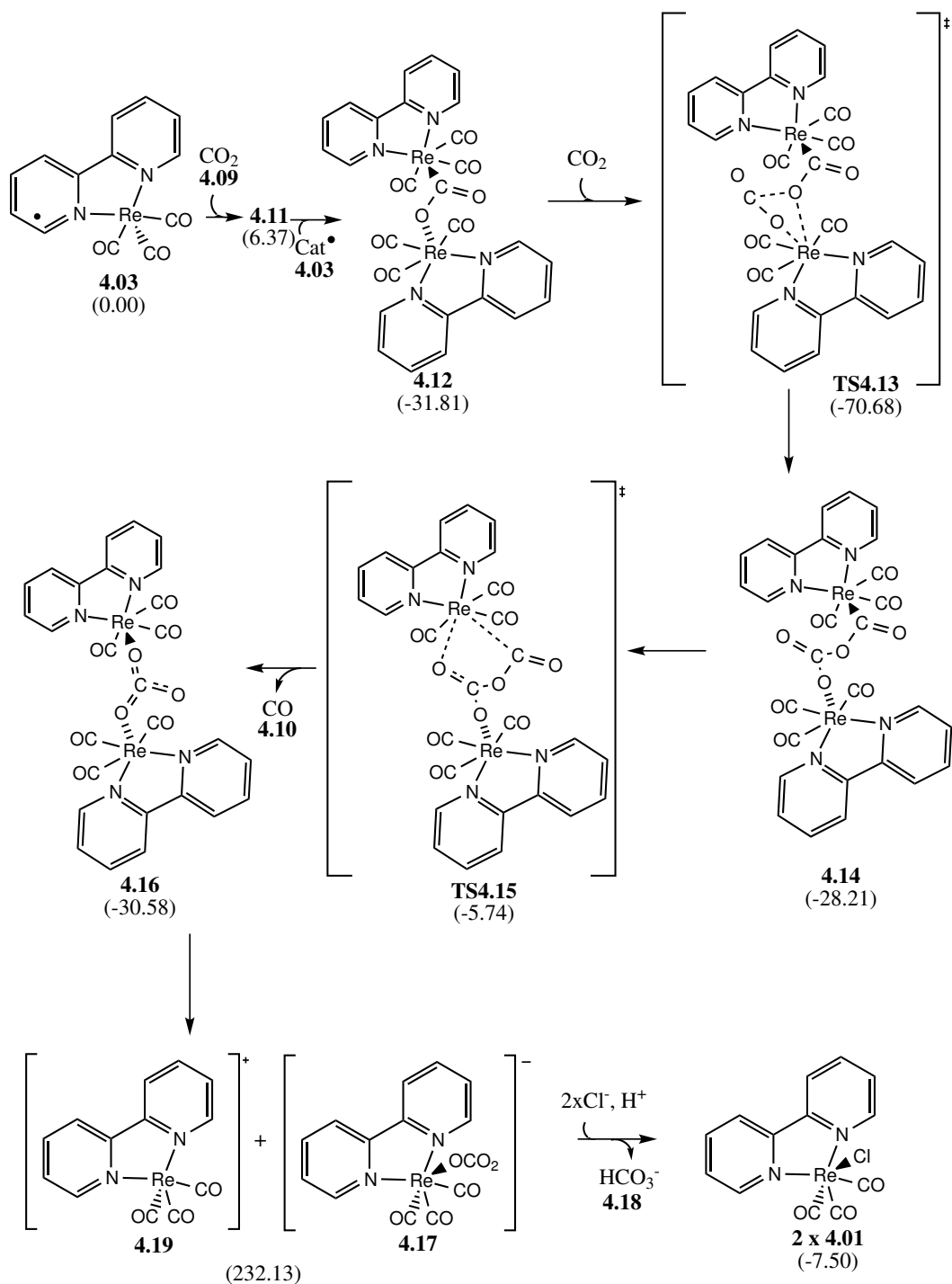
Steps	Energy(gas) ^a	Energy(dmf) ^b
4.03 + 4.09 → 4.11	-0.25	6.37
4.11 + 4.03 → 4.12	-31.56	-42.39
4.12 + 4.09 → TS4.13	-33.27	-34.66
TS4.13 → 4.14	45.91	42.47
4.14 → TS4.15	21.10	22.46
TS4.15 → 4.16 + 4.10	-24.36	-24.84
4.16 → 4.17 + TS4.19	317.95	262.71
4.17 + TS4.19 + 4.04(×2) → 4.01(×2) + 4.18	-180.55	-239.63

^a TPSS energy in kcal/mol.

^b TPSS energy in kcal/mol with COSMO solvation in DMF.

The mechanism begins with the addition of a CO₂ molecule to the excimer **4.03**, forming **4.11**. This is a very weakly bound species when solved in a simulated DMF environment; in the gas phase this transition complex will not solve. Energies for the gas phase for this compound are calculated as single point energies from the solvated structure. The DMF solved structure has a Re-C bond length of 2.51 Å, and O-C-O

add last
struct



Scheme 4.4 The ‘bicarbonate’ mechanistic pathway. Energy in kcal/mol relative to the excimer **4.03** is shown in brackets for each compound.

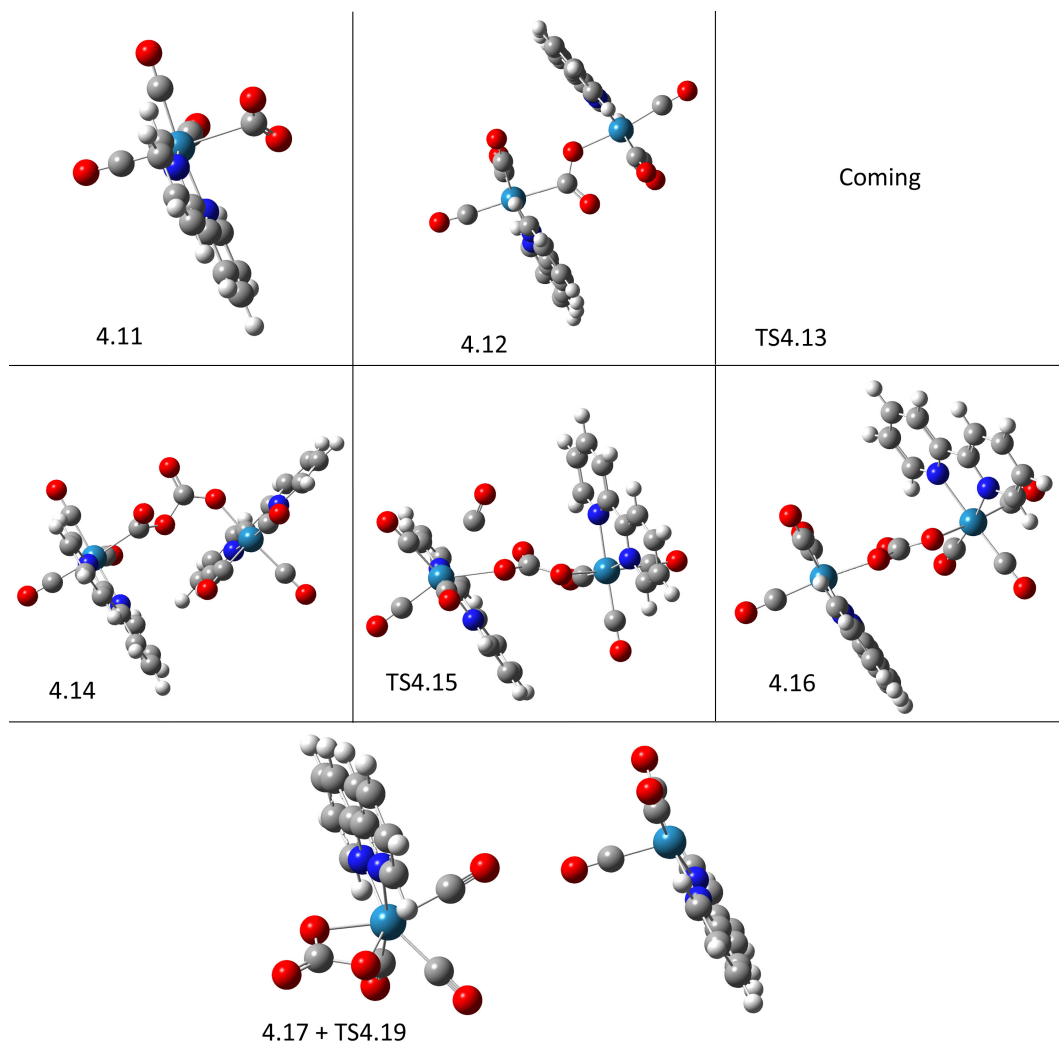


Figure 4.2 DFT calculated structures for the ‘bicarbonate’ mechanistic pathway. Atoms are coloured as follows: carbon - grey, nitrogen - blue, oxygen - red, hydrogen - white, rhenium - teal.

bonding angle of 142° , when compared to the Re–C distances of rhenium carbonyls of *ca.* 1.9 \AA , this is a very weak bond. The formation of this complex requires only 6.37 kcal/mol, the radical species is not satisfied with the addition of CO_2 and requires further electron contribution to become more stable. This unstable complex is able to extract a hydrogen from triethylammonium (Et_3NH^+ , **4.08**) to continue with the ‘water-

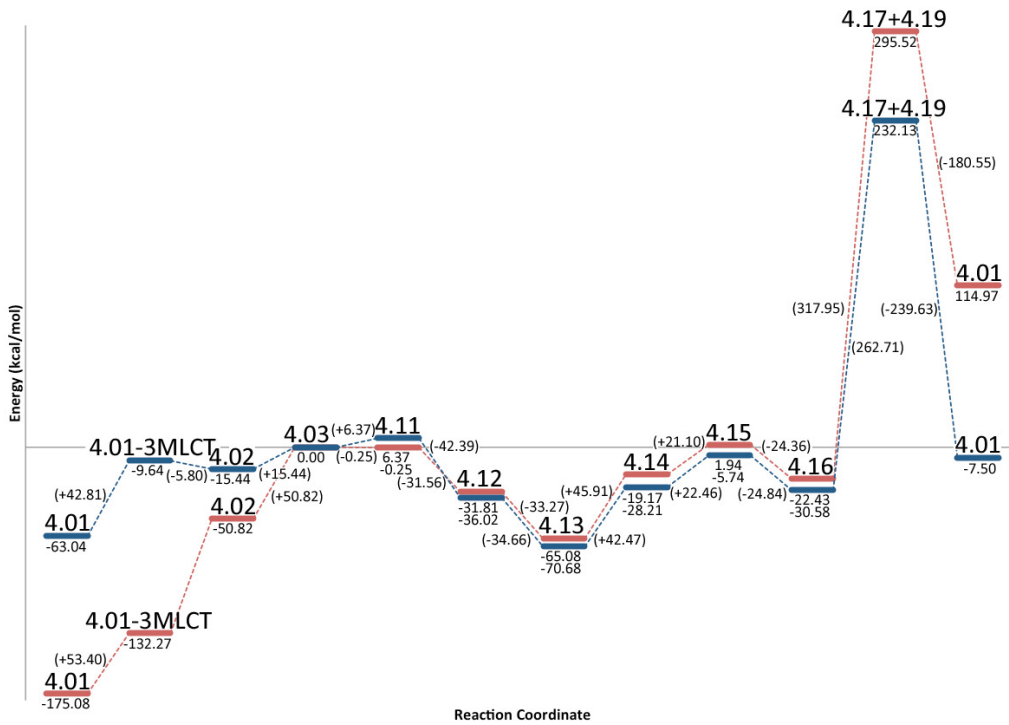


Figure 4.3 Potential Energy Surface for the bicarbonate mechanistic pathway. Gas phase energies in red, DMF solvated energies in blue. A larger version is available in Appendix D, Figure D.7.

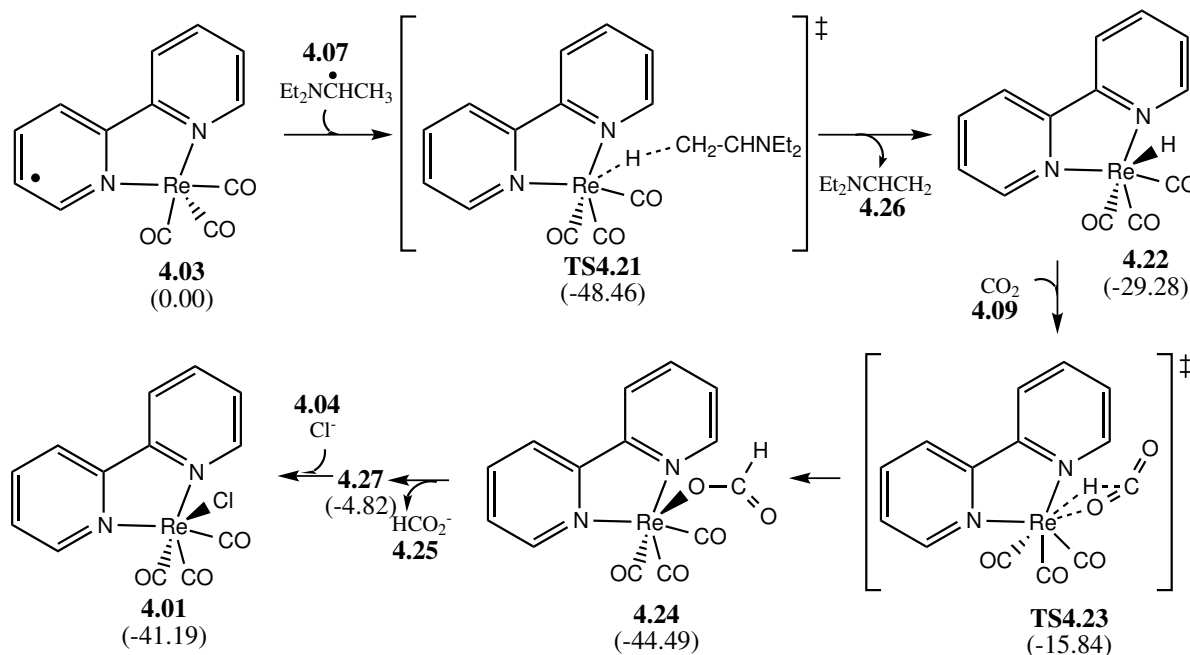
gas' pathway (see below subsection 4.2.4), or combine with a second molecule of the excimer to form a dimer **4.12**. This dimer formation is exothermic by 42.4 kcal/mol in DMF. The quenching of the radical forms much stronger bonds between the metal atoms and the linking CO_2 . The Re-C distance has shortened from the 2.51 Å seen in **4.11** to 2.26 Å. This is still longer than the Re-CO bonds, which is expected due to the lack of π back-bonding observed with carbonyl ligands, however, it corresponds with similar published crystal structures of Re-C bond lengths for sp^2 carbons.¹⁸⁹ The Re-O bond is 2.13 Å, a value that remains constant for Re-O through the intermediates in the reaction pathway.

After the dimer **4.12** has been formed, a second molecule of CO_2 is inserted via tran-

sition state **4.13** to form the Re-C(O)-O-C(O)-O-Re complex **4.14**. This C₂O₄ linker contains C–O single bonds of length 1.28 Å, and C=O double bonds of 1.44 Å, longer than expected by about 0.1 Å for both sp²-carbon oxygen single or double bonds.¹⁹⁰ Bond angles are typically just under the idealized 120° expected as well. Due to the linker, the two catalyst ligand bipyridines have moved from a nearly co-planar geometry to a nearly perpendicular geometry. Re-C and Re-O bonds remain constant in length compared to **4.12**. The formation of a 5 membered ring transition state structure **4.15** costs 22 kcal/mol. This leads to the release of the CO and the formation of a carbonate linked dimer, **4.16**, resulting in a net energy decrease of -2.4 kcal/mol, and returning the catalyst ligands to a more co-planar orientation. The carbonate dimer species is left to decompose to a catalyst cation **4.19** with an open site, and the carbonate adduct **4.17**. This carbonate dianion may pick up a proton before or after the disassociation to the catalyst cationic species, resulting in the released of the bicarbonate species to solution (**4.18**) when the catalyst is returned to ground state **4.01** with addition of a chloride. The decomposition of the bicarbonate dimer species has a barrier of 262 kcal/mol in DMF. This is due to the charge separations that occur, while solvation stabilizes these charged species it does not accurately simulate a system with an ionic strength similar to what could be expected in the experimental reaction. The Gibbs energy for this step was calculated to be -11.4 kcal/mol in solution, with an additional -17 kcal/mol for the anion exchange, signifying the thermodynamic favourableness of this transformation. The presence of excess molar equivalents of an electrolyte such as tetraethylammoniumchloride ensures a surplus of chloride anions are in solution and are an additional force for conversion, according to Le Châtelier's principle.

4.2.3 The ‘Formate’ Pathway

In comparison to the catalytic dimer formed in the bicarbonate pathway above, the formate formation occurs via a much simpler mechanism. This mechanism is shown in the green box in Scheme 4.1, with details shown in Scheme 4.5. The addition of a hydrogen to the open site axial to the metal occurs via the simultaneous electron and proton transfer from a by-product of the reduction of the amine. CO_2 inserts into this metal hydride bond, resulting in the formate ligand bonded through the oxygen center.^{191–193} Separation of the weak metal-oxygen bond allows for the substitution of the halide to the cationic metal centre.



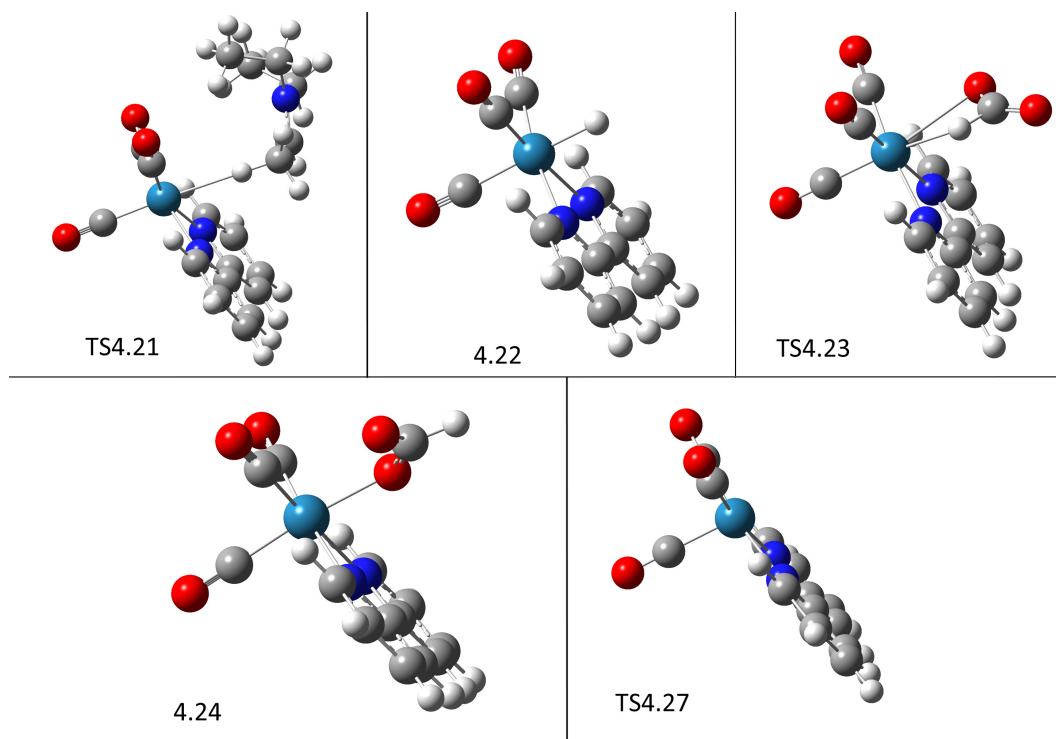
Scheme 4.5 The ‘formate’ mechanistic pathway. Energy in kcal/mol relative to the excimer **4.03** is shown in brackets for each compound.

Table 4.3 shows the potential energy change in each step of the reaction. The computed intermediate and transition state structures are shown in Figure 4.4.

After formation of the excimer **4.03**, the radical species extracts a hydrogen atom

Table 4.3 Energies for the reaction steps in the ‘formate’ pathway

Steps	Energy(gas) ^a	Energy(dmf) ^b
4.03 + 4.07 → TS4.21	-63.61	-67.08
TS4.21 → 4.22 + 4.26	41.05	37.23
4.22 + 4.09 → TS4.23	21.24	14.02
TS4.23 → 4.24	-33.94	-28.66
4.24 → 4.25 + TS4.27	140.39	39.67
TS4.27 + 4.04 → 4.01	-141.77	-36.37

^a TPSS energy in kcal/mol.^b TPSS energy in kcal/mol with COSMO solvation in DMF.**Figure 4.4** DFT calculated structures for the ‘formate’ mechanistic pathway. Atoms are coloured as follows: carbon - grey, nitrogen - blue, oxygen - red, hydrogen - white, rhenium - teal.

from the oxidized chain of the sacrificial amine **4.07** in transition state **4.21**, a step exothermic by 67.1 kcal/mol in the gas phase and 63.6 kcal/mol in DMF. This is due to the satisfaction of the radical states and removal of the charge on the amine. The radical

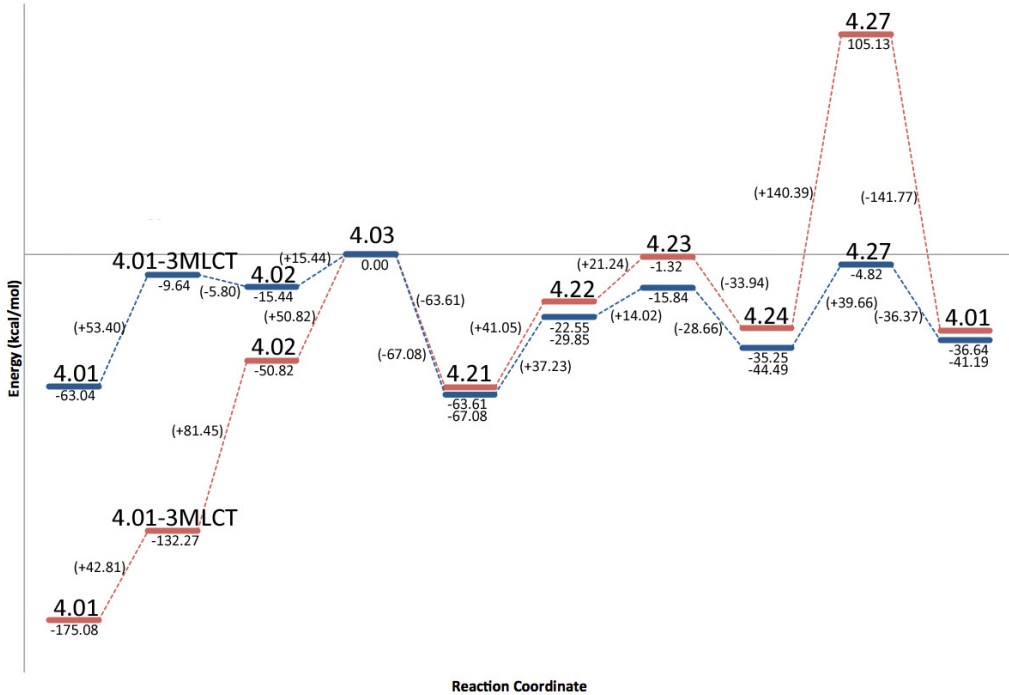


Figure 4.5 Potential Energy Surface for the formate mechanistic pathway. Gas phase energies in red, DMF solvated energies in blue. A larger version can be seen in Appendix D, Figure D.6.

amine (**4.07**) had been previously formed (see subsection 4.2.1). Extraction of the proton and electron pair allows for the formation of the ethene, completing the decomposition of the amine to the final neutral, singlet molecule **4.26**. Relaxation of this transition state results in the hydrogen extraction from the radical species, yielding the formation of the hydride complex **4.22**.

This hydride complex is able to insert a molecule of CO₂ into the metal-hydrogen bond, in transition step **4.23**, with a 14.4 kcal/mol barrier to transition state formation. CO₂ insertion to metal hydrides is commonly observed, most mechanisms in CO₂ reduction in similar ruthenium systems employ this addition.¹⁹³ The Re-H bond length is 1.76 Å, compared to the length of the Re-Cl bond from the ground state **4.01** species of 2.51 Å. This bond length difference reflects the observations on anion change from Cl

to Br (as discussed in chapter 2, subsection 2.3.2), the anion size is the critical factor in this variation. When a molecule of CO₂ approaches, the transition state of a pseudo-septacoordinate species **4.23** forms. The Re-H bond increases in length to 2.16 Å, the Re-O bond is 2.88 Å, and the O-Re-H angle is very tight, at only 45.3°. This step completes with 28.66 kcal/mol energy release to form the formato anion complex **4.24**.

The formato anion **4.24** contains a Re-O bond of 2.15 Å, consistent with previously discussed rhenium - oxygen bonds. This formate dissociates with a chloride addition, the exchange is endothermic by less than 3 kcal/mol overall, but the charge separated transition state formation is endothermic by nearly 40 kcal/mol in DMF (or 140 kcal/mol in gas phase). As discussed with the bicarbonate mechanism, this large cost is due to the charge separation that occurs. The calculated Gibbs energy for the formation of the charge separated transition state is -12.7 kcal/mol in solvent, showing the thermodynamic favourableness of this exchange. Further reactions of the formato anion in solution are not investigated, but the anion may remain deprotonated in the slightly basic environment.¹²⁷

It is possible that the mechanistic cycle restarts with **4.24** absorbing a photon instead of substituting for the chloride. This would not affect the next catalytic cycle; either anion is lost in formation of the excimer.

Some attempts were made at performing the CO₂ binding reaction by alternative geometries. While direct σ bonding from a metal to an oxygen atom in the CO₂ molecule (as η^1 -OCO) has been observed in a few systems (including photoreduction of CO₂ on other metal systems),^{194–196} this geometry is rare.^{197–199} Attempts to coordinate CO₂ in an η^1 -OCO geometry failed to converge both in gas and solution phase, as CO₂ was ejected from the complex. Binding of CO₂ to the metal through π coordination of the C=O bond is more common,^{198,199} but these structures failed to solve in the current DFT system as well.

4.2.4 The ‘Water-Gas Shift’ Pathway

The water-gas shift mechanism involves the addition of two protons from the reductant to a CO₂ molecule bound to the metal centre, as shown in the red box in Scheme 4.1. The mechanism is shown in greater detail in Scheme 4.6. The first proton addition yields an acid species, this is dehydrated via the second addition of a proton and the release of one molecule of H₂O. The resulting tetracarbonyl cationic species is able then to release an axial carbonyl to return to the ground state. While any of the carbonyl groups could be labile, either of the carbonyl ligands at the axial positions are the ones actively replaced by the halide to return to the starting catalyst.¹⁸⁰

Table 4.4 shows the potential energy change in each step of the reaction. The potential energy surface is shown in Figure 4.7. The computed intermediate and transition state structures are shown in Figure 4.6.

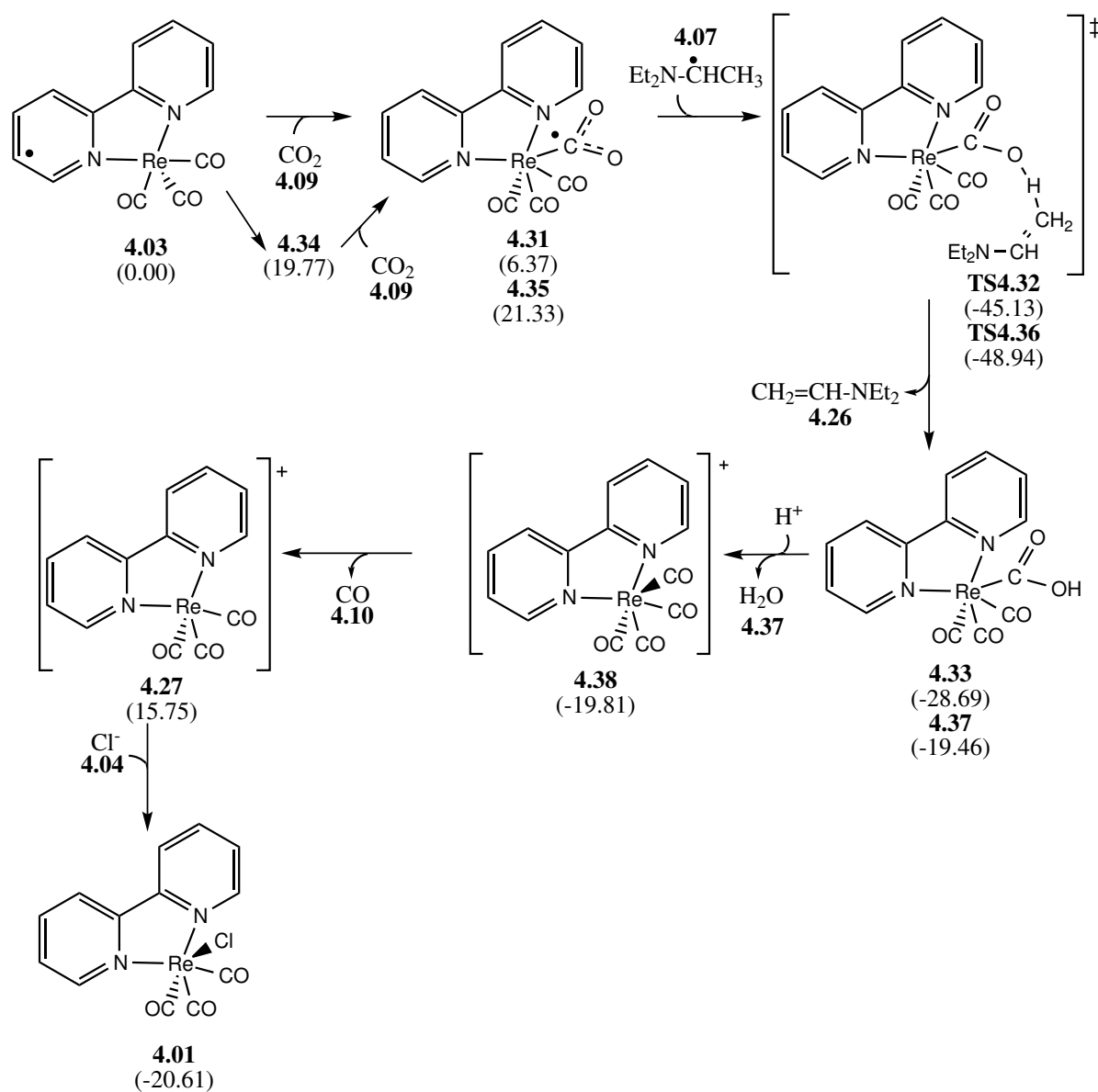
Table 4.4 Energies for the reaction steps in the ‘water-gas shift’ mechanism

Steps	Energy(gas) ^a	Energy(dmf) ^b
4.03 + 4.09 → 4.31	-0.25	6.37
4.31 + 4.07 → TS4.32	-34.68	-46.72
TS4.32 → 4.33 + 4.26	15.33	11.64
4.33 → 4.38 + 4.39	-6.51	8.88
4.38 → 4.27 + 4.10	40.89	35.57
4.27 + 4.04 → 4.01	-141.77	-36.37

^a TPSS energy in kcal/mol.

^b TPSS energy in kcal/mol with COSMO solvation in DMF.

This mechanistic pathway appears to begin by the same addition of CO₂ that is seen in the bicarbonate mechanism (see subsection 4.2.2), forming **4.11**. As before, the complex is only weakly coordinated, and requires solvation effects to solve computationally. The added CO₂ is able to extract a hydrogen from the previously-reduced sacrificial amine **4.07** with a net energy change of -35.1 kcal/mol in DMF, again allowing the formation of



Scheme 4.6 The ‘water-gas shift’ mechanistic pathway. Energy in kcal/mol relative to the excimer **4.03** is shown in brackets for each compound.

the ethene amine **4.26**. The newly formed acid species **4.32** dehydrates in the presence of a second proton (via **4.33**) to form water **4.37** and the tetracarbonyl cationic species **4.38**. This is endothermic by 8.9 kcal/mol in solution, but the ΔG is -15 kcal/mol. This tetracarbonyl cation exchanges a CO molecule for a Cl^- to return to **4.01**, with a

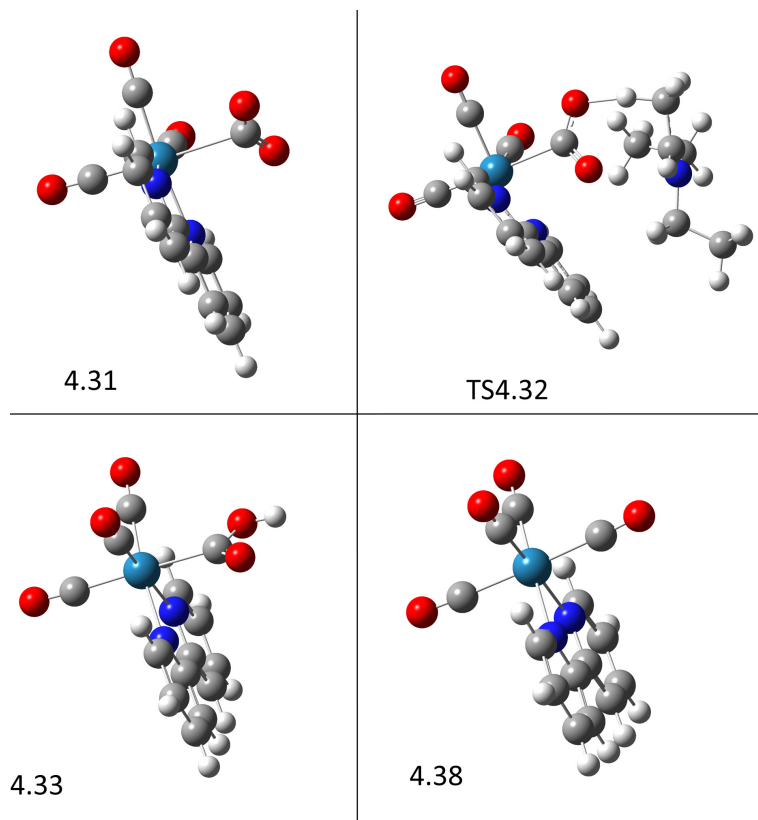


Figure 4.6 DFT calculated structures for the axial ‘water-gas shift’ mechanistic pathway. Atoms are coloured as follows: carbon - grey, nitrogen - blue, oxygen - red, hydrogen - white, rhenium - teal.

0.8 kcal/mol energy release.

Typically, this reaction had been thought to proceed on the axial site of the catalyst, mirroring the pathways discussed above. However, due to the ease of migration of carbonyl groups in organometallic complexes, it is proposed that the ‘water-gas shift’ mechanism does not occur axial to the ligand, but begins with relocation of a CO_2 ligand to the axial position (see Scheme 4.7), followed by the coordination of CO_2 into the now vacant planar open site, forming **4.35**. Potential energies for this reaction are shown in Table 4.5, and the potential energy diagram is shown in Figure 4.9. DFT computed structures are shown in Figure 4.8.

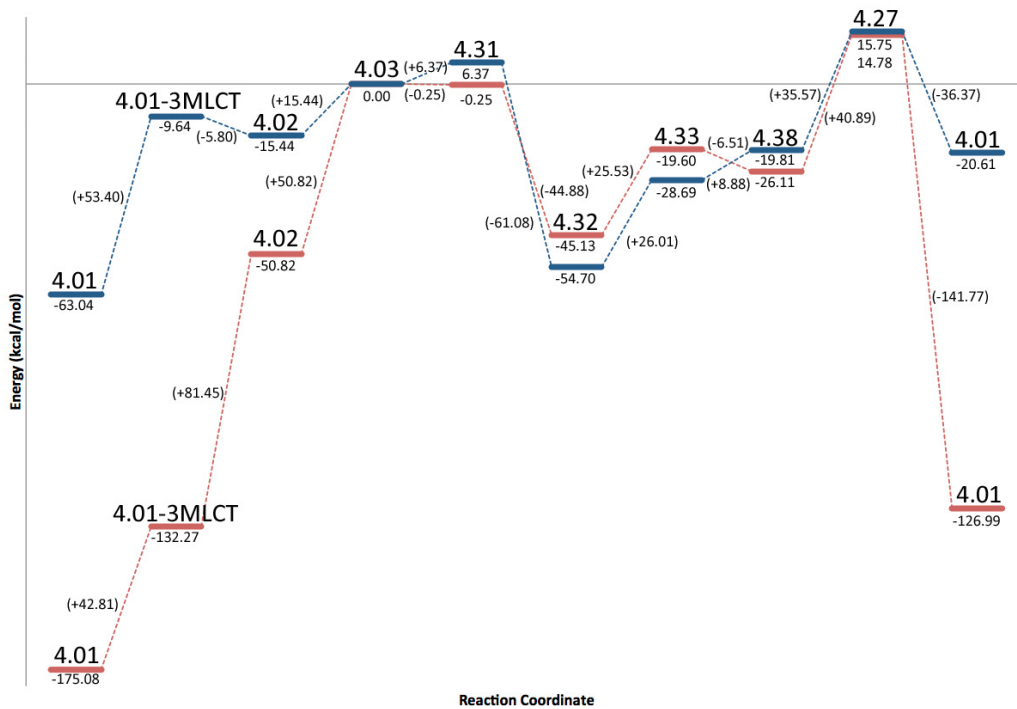
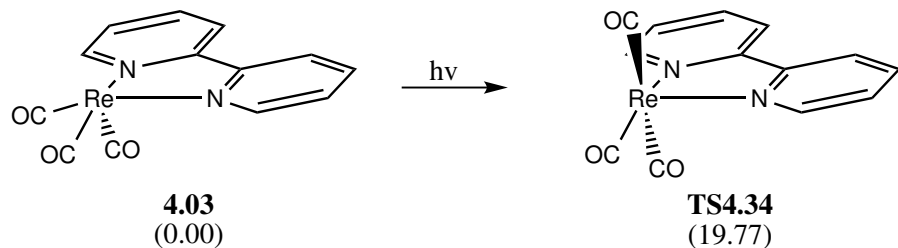


Figure 4.7 Potential Energy Surface for the axial geometry of the water-gas shift mechanistic pathway. Gas phase energies in red, DMF solvated energies in blue. A larger version can be seen in Appendix D, Figure D.3.

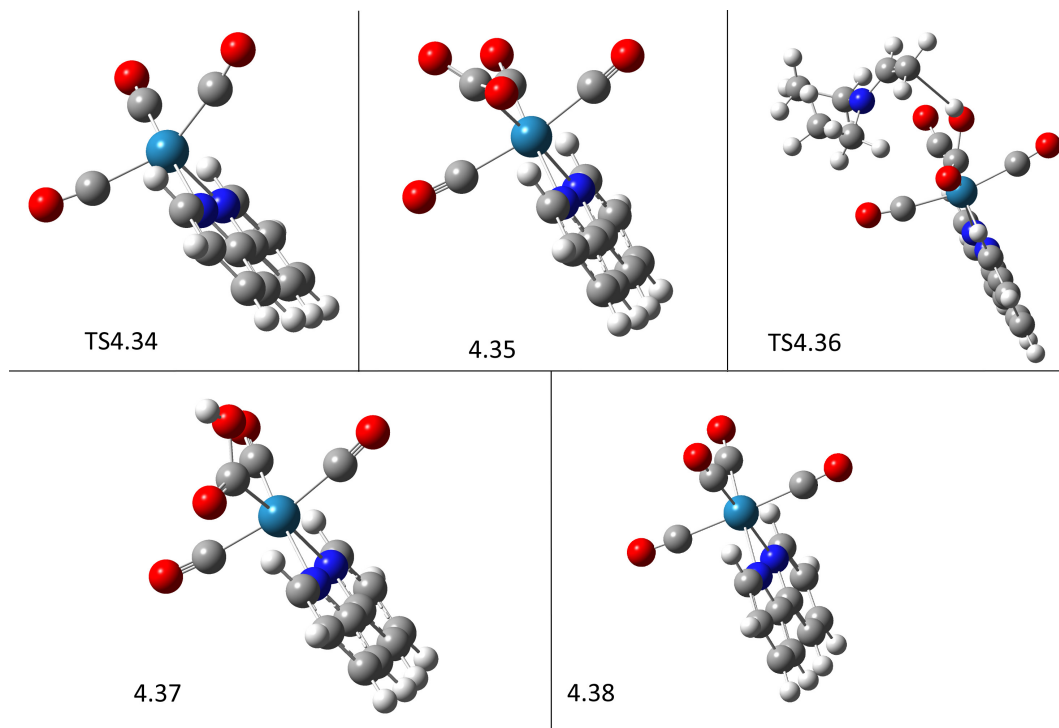


Scheme 4.7 Rearrangement of carbonyl and open site. Energy in kcal/mol relative to the excimer **4.03** is shown in brackets for each compound.

This CO_2 bound in the plane of the ligand then undergoes hydrogen addition and dehydration to produce a molecule of H_2O , continuing as before. Once reduced to the tetracarbonyl cluster, the catalyst could shed any CO ligand and pick up a chloride anion to return to the neutral ground state. However, labilization of one of the two axial

Table 4.5 Energies for the reaction steps in the ‘equatorial’ geometry

Steps	Energy(gas) ^a	Energy(dmf) ^b
4.03 → TS4.34	23.37	19.77
TS4.34 + 4.09 → 4.35	4.79	1.56
4.35 + 4.07 → TS4.36	-36.36	-49.13
TS4.36 → 4.37 + 4.26	-3.39	8.34
4.37 → 4.38 + 4.39	-14.52	-0.35
4.38 → 4.27 + 4.10	40.89	35.57
4.27 + 4.04 → 4.01	-141.77	-36.37

^a TPSS energy in kcal/mol.^b TPSS energy in kcal/mol with COSMO solvation in DMF.**Figure 4.8** DFT calculated structures for the equatorial ‘water-gas shift’ mechanistic pathway. Atoms are coloured as follows: carbon - grey, nitrogen - blue, oxygen - red, hydrogen - white, rhenium - teal.

carbonyls is the most favoured, formation of the planar coordinated chloride complex is not expected.¹⁸⁰

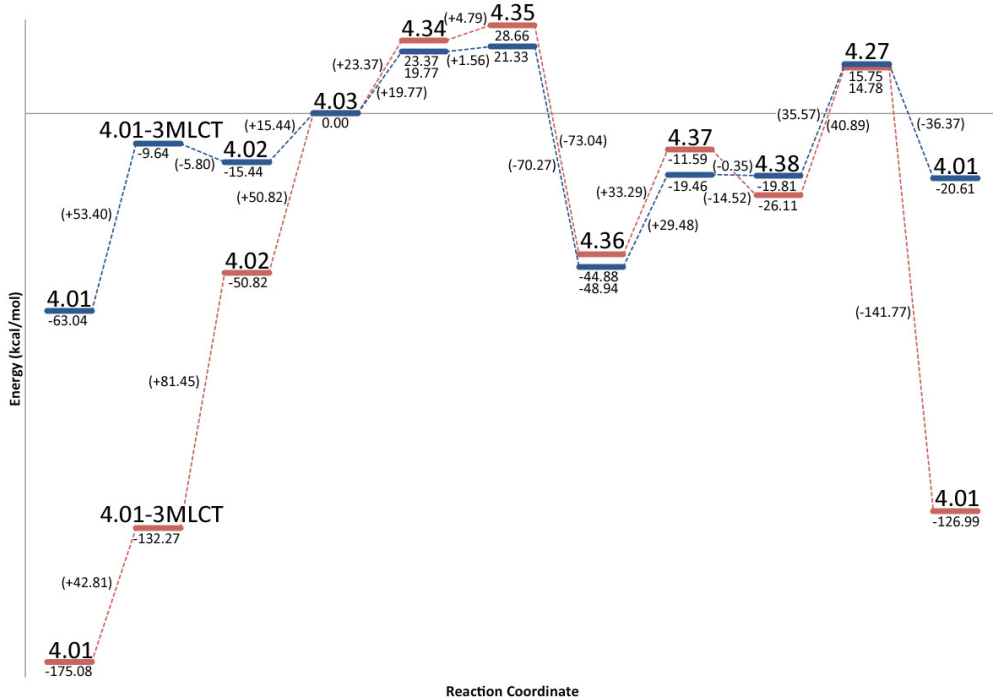


Figure 4.9 Potential Energy Surface for the planar geometry of the water-gas shift mechanistic pathway. Gas phase energies in red, DMF solvated energies in blue. A larger version can be seen in Appendix D, Figure D.4.

This newly proposed mechanism provides an explanation to a previously unexplained phenomenon. The exchange of carbonyl groups on the catalyst for ^{13}CO when using $^{13}\text{CO}_2$ in the photoreduction is documented as early as Hawecker *et al* in 1986.⁶⁷ It was shown that complete exchange occurs with very few catalytic turnovers. Furthermore, Koike *et al.* demonstrated that photochemical ligand substitution occurs at only axial sites relative to the α -imino ligand,¹⁵⁴ no exchange occurs at the equatorial site, nor can the *fac*- $(^{12}\text{CO})_2^{13}\text{CO}$ be expected to shift the ^{13}CO to the equatorial position in the time-frame of the reaction. Thus the isotopic exchange does not proceed by independent uptake of produced ^{13}CO , instead the conversion to the ^{13}CO complex must be inherent in the reduction mechanism.

This modified geometry does not violate any previously published experimental mechanism work. These studies typically focus on photophysical or spectroscopic analysis to determine intermediates. The analysis methods used define molecular composition; they are not structural characterization techniques. Re-evaluation of the spectral data within these newly defined parameters does not invalidate the work, mechanistic descriptors published (such as kinetics) are still valid within the new geometry.

Additionally, this provides an explanation for the lack of CO₂ reduction by (terpy)- κ^2 -Re(CO)₃Cl discussed in chapter 3. While the carbonyl group is transitioning to the axial site, before a molecule of CO₂ has been coordinated to the complex, the catalyst is in optimal geometry for chelation of the pendant arm (see Scheme 3.1) as discussed in chapter 3. It was previously shown that the tridentate catalyst is inactive for CO₂ photoreduction, the formation of a κ^3 complex modifies the photophysics, deactivating the catalyst's reactivity.

4.3 Comparison Between Mechanistic Pathways

Previous studies in literature had only analyzed one of the mechanistic pathways (or a subsection thereof), without a fuller analysis of the competitiveness of each pathway relative to the others. Discussion on the tenability of each potential pathway relied on the *in situ* observation of intermediates or transition states, the success (or lack thereof) of synthesis of the intermediates, and the relative production of by-products in the mechanistic trials.

The overall potential energy diagrams for each of the mechanistic pathways given in Scheme 4.1 are shown in Figure 4.10. Individual mechanistic pathways, and separate potential energy diagrams for gas phase and DMF solvated structures are listed in Appendix D. This figure shows the difficulty in determining the most likely reaction pathway

based on computational analysis alone. The difference in energy consumption between mechanisms is quite small, with the largest barriers belonging to the final disassociation of the product and coordination of chloride.

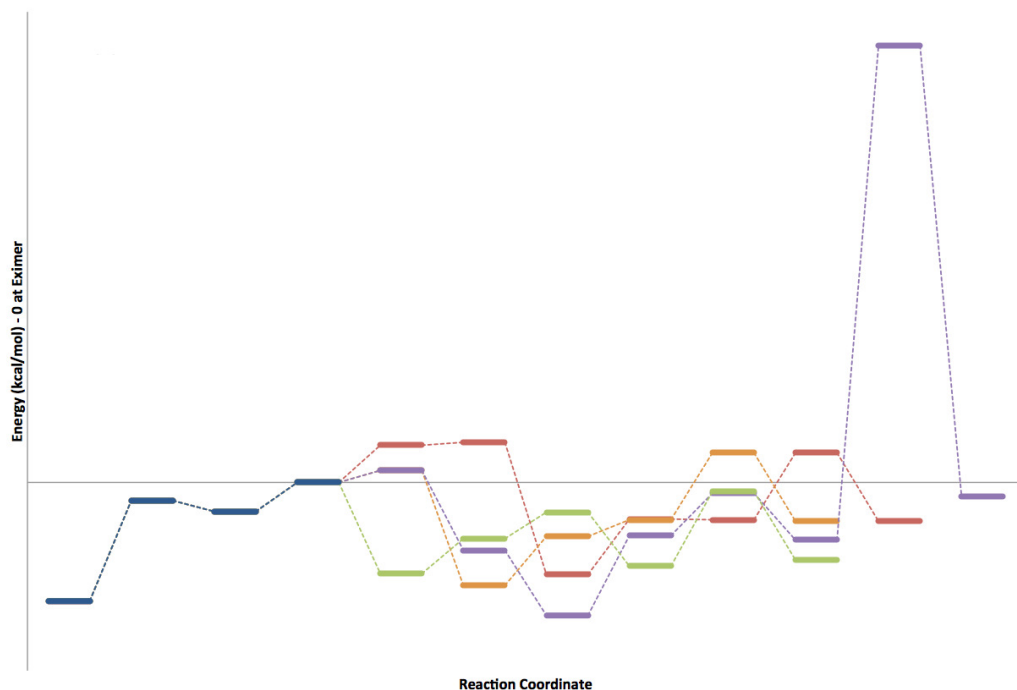


Figure 4.10 An overview of the energies of the three mechanistic pathways of photochemical CO₂ reduction in DMF. Excimer formation is shown in blue, the planar water-gas shift mechanism in red, the axial water-gas shift in orange, the bicarbonate in purple, and the formate in green.

Experimental data shows that each of the mechanisms is feasible and could occur in certain conditions. Both the formate and water-gas routes have the maximum transition energy barrier for the final disassociation of the product and coordination of chloride. This barrier is artificially high, the charge separation that occurs is impacted significantly by the basic pH and the presence of electrolyte in solution experimentally. These factors are not taken into consideration in the calculations. Gibbs energies were calculated for these steps, the average ΔG values are around -12 kcal/mol for the production of the

transition state, signifying a thermodynamically favoured reaction.

Due to the similarity in potential energy profiles for these reactions, analysis of experimental data must be undertaken to accurately predict which pathway dominates the photoreduction of CO₂. The energy requirements of each pathway is not the only indicator of mechanistic preference. Studies have shown the rate differs between pathways, with the formation of certain intermediates being so slow as to nearly block the progression of the redox reaction. Utilization of modified reaction conditions (TEA vs. TEOA, changing solvent mixture, presence or absence of H₂O, presence or absence or modification of electrolyte) can provide a range of reduction products, by-products, and intermediates.^{66,67,70,87,127,145}

4.4 Conclusions

Three feasible mechanistic pathways for the photocatalytic reduction of CO₂ were investigated in detail using consistent DFT methods, allowing for their comparison. Mechanistic steps not previously elucidated were demonstrated, showing the full mechanistic cycle from ground state excitation through the reaction of the excimer with CO₂ to the final release of product and reforming of catalyst.

A modified geometry for the production of CO and H₂O by the ‘water-gas’ mechanism was proposed. This new geometry does not conflict with previously published experimental data, and provides explanation for previously reported phenomenon. It aligns with the previously demonstrated inactivity of terpyridine catalysts, in contrast to the highly active bipyridine analogue. This new geometry provides an avenue for the isotopic exchange of carbonyl ligands from ¹²CO to ¹³CO when the reduction is carried out with ¹³CO₂.

Chapter 5

TurboControl

The analysis of the mechanism using computational methods required a significant amount of manual set-up and analysis work of computational input and output files. The calculations required hundreds different molecules, intermediates, or transition state candidates to be calculated in multiple different environments, with the final mechanism employing 38 species in gas and solvated systems. These calculations typically require intervention or set-up of intermediate steps to be able to fully elucidate all of the required information, for example, the set-up of frequency calculations after a geometry optimization to ensure ground state or transition state geometries.

Additionally, while TurboMole contains much faster optimization code for DFT calculations, the user interface is exceptionally user-unfriendly and involves an abrasive interactive text prompt environment. This contrasts to Gaussian 09, which is significantly more popular, particularly due to the user-friendliness of the GaussView graphical user interface (GUI), despite concerns about the speed of optimization of large or complex molecules.

These two factors prompted the development of a new program, TurboControl, written in Python, with the goal of combining the user friendliness of GaussView on top of the

optimization efficiency of TurboMole. This program allows a user to prepare the input files in GaussView, modify them slightly in any text editor available to them, then run a batch calculation on the files. TurboControl monitors the computational jobs, resubmitting for frequency calculations when optimization is complete if requested, and using the TurboMole tools available when required to ensure ground state or first transition state geometries are discovered. TurboControl then creates a single output file, providing the energy and first frequency vibration of each molecule. Additional commands can instruct TurboControl to run in a solution, do single-point energy calculations, or gather more in-depth thermodynamic information from the outputs using TurboMole’s tools.

TurboControl provides this hands-off management of jobs allowing the user to spend more time in data analysis, experimental work, or to be able to produce data at a significantly higher rate compared to the manual setup and monitoring of jobs. TurboControl also contains a single job initiation script entitled TurboGo to allow for the use of the input files without the overhead of the job managing.

This section will describe the development, features and usage of the TurboControl code in more detail.

5.1 Development

TurboControl began as a script for the simple setup and submission of jobs in TurboMole from Gaussian input files. The jobs were submitted to the ‘wooki’ computing cluster managed by the Woo lab, available at the University of Ottawa. This computing cluster consists of approximately 1000 CPU cores, running the CentOS distribution of Linux available in the Rocks software distribution. The GridEngine queuing system ensures fair usage of computing cores for each user, and maximizes throughput by managing computational jobs.

TurboControl initially submitted jobs and monitored their successful completion or failure. Development quickly expanded to include automatic resubmission for frequency analysis of geometry optimization jobs, required to determine the success of finding an energy minima (stationary point) instead of a transition state. TurboMole contains multiple ways of determining the ground state frequency of a geometry optimized molecule, TurboControl is granular enough to utilize whichever method is requested, or will default to a particular method if none is requested explicitly. While some methods are parallel calculations in TurboMole, others are able to utilize only a single processor core. Resubmitting jobs to the cluster's queue after each step ensures computational resources are not wasted, they are able to be shared appropriately by the queue.

As the complexity of the mechanistic study (see chapter 4) increased to include analysis of thermodynamic data, calculation of transition states, calculation in solution phases, and more, the capabilities of TurboControl were developed to meet these increased demands.

TurboControl is now able to handle large batches of input, with jobs of varying complexity and monitor them through successful completion or failure of the TurboMole calculation. Analysis of the computational jobs is performed to simply highlight DFT energies, first computed normal mode frequencies, and thermodynamic properties (if requested).

Development of TurboControl contained extensive testing at every step. Each function was tested as extensively as possible, including edge cases, error cases, and null inputs. This testing minimizes runtime errors, reducing the frequency of crashes of the code. Some code was unable to be subjected to programmed testing, the code interacting with the TurboMole scripts directly has been tested manually by developing test use cases. Test coverage can be seen in Appendix E, Code Details.

Code was written to be ‘object oriented’, that is, the code treats every molecule and job as an object, with defined properties, functions, and methods to manipulate these objects. This is a well defined coding style utilized when dealing with many items of similar type that contain data, when that object can be manipulated, activated, or modified. The data in the object is not modified directly, changes to the data is accessed via ‘methods’ that are properties of the object.

The code was written to be compliant with popular best practices, especially those designed for the Python language and described in ‘PEP8’.²⁰⁰ Deviations from the style guide were minimized and permitted only in special cases. Proper in code documentation was included as well, using both docstrings and inline comments.²⁰¹ This ensures code readability and simplifies future development by any author. The entire project is approximately 5500 lines of code, including tests, helper scripts, licence, and readme files.

5.2 Usage

TurboControl is available freely on the internet, and is a fully open-source project.²⁰² The code may be downloaded by anyone and be installed and used without prior permission for personal, academic, or commercial purposes, provided that the original software license remains with the code. TurboControl works only with the stated versions of software in the ‘readme’ file available with the code on the internet (and included in Appendix E). The software requires no installation prior to use, and has very few dependencies beyond the typically installed packages on a Unix or Linux system.

TurboControl and TurboGo are not quantum mechanical packages themselves, they require a properly licensed installation of TurboMole to perform calculations. Additionally, while GaussView may be used to prepare the input files, modification of the files by

hand in a text editor is required to access most features, GaussView is not required for the use of TurboControl.

5.3 Conclusions

TurboControl and TurboGo are two scripts developed to maximize throughput and minimize operator involvement in large computational studies utilizing TurboMole. Development of these scripts is not limited to the scope of the thesis, an open source licence and source code freely available on the internet mean this project may be adopted and further developed by others who are interested in its use. The scripts are not quantum chemical packages themselves, a fully licensed copy of the TurboMole software is required for their usage.

Chapter 6

Conclusions

The target Re^I terdentate terpyridine compounds were successfully synthesized and fully characterized. The experiments resulted in the first crystallographically verified *mer*- κ^3 -(N, N', N'')-Re(CO)₂X complexes. These terpyridine complexes are accessed via a simple, highly efficient, solid-state thermolysis pathway. These complexes expand the previously known α -diimino photophysical properties, with enhanced metal to ligand *d*- π^* electronic transitions than the associated bidentate compounds. These experimental observations are supported by computational TD-DFT results, providing a deeper understanding of frontier molecular orbital environments for these complexes.

The synthesized catalysts were tested for the photoreduction of CO₂. The α -triimino catalysts show no activity for the reduction of CO₂, in contrast to the known excellent bipyridine compounds, potentially due to the lack of fluorescence of the terdentate complexes, and the chelating ability of the pendant arm in the bidentate 2,2':6,2''-terpyridine ligand. These catalysts may be suitable for electrocatalytic reduction of CO₂, further investigation will be required.

Reaction mechanisms of the photocatalytic reduction of CO₂ by bipyridine catalysts were studied successfully with DFT methods. This study was the first to show the en-

tire catalytic cycle, from eximer formation to CO₂ insertion and to catalyst reformation. This study also resulted in the proposed new geometry for the production of CO with no carbonate or formate anions. This new geometry does not conflict with known experimental studies, yet avoids three-body mechanistic steps previously seen in literature. This geometry provides explanation for previously unexplained phenomenon of ¹³CO ligand exchange in few turnovers.

Development of a tool for the rapid submission and automated job monitoring for the TurboMole program facilitated the mechanism investigation by maximizing computational throughput while minimizing set-up and analysis time for the user. The scripts increase the ‘black box’ nature of TurboMole, increasing the usability to include those unfamiliar with the program, and take advantage of the high performance of TurboMole relative to other computational suites. An open source licence and freely available source code mean this project may continue with other developers in the future

Appendix A

Experimental Procedures

Experimental synthesis and characterization data for the compounds discussed in this thesis are shown below by compound number:

A.1 General Methods

Synthesis reactions were set-up in a glovebox under a nitrogen atmosphere and performed under an inert atmosphere. Solvents were sparged with nitrogen and then dried by passage through a column of activated alumina using an apparatus purchased from Anhydrous Engineering. Deuterated chloroform and deuterated acetonitrile was dried using activated molecular sieves. Rhenium starting materials were purchased from Strem Chemicals and used as received. All other chemicals were purchased from Aldrich and used without further purification. NMR spectra were run on Bruker Avance 400MHz spectrometers with CD_3CN or CDCl_3 as solvent and internal standard. Elemental analyses were performed by Midwest Microlab LLC, Indianapolis IN. Solid state reactions were carried out in a Lindberg Blue M Mini-Mite Tube Furnace (model TF55035A-1). Infrared spectra were collected using an Agilent Technologies Cary FT-IR spectrome-

ter using a diamond ATR attachment. UV-Vis spectra were collected using a Agilent Technologies Cary 5000 UV-Vis spectrometer. TGA was performed on a TA Q5000 IR instrument: approximately 10-15 mg of each sample was placed in a ceramic sample pan which was heated at a rate of 5 °C/min up to 150 °C, followed by a rate of 2 °C/min to 300 °C while being purged with N₂ at a flow rate of 25 mL/min. GC was performed using a HP gas chromatograph with a 15 m CARBONPLOT column with 0.320 mm inner diameter and 1.50 μ film in a 40 °C oven. The instrument is fitted with a TCD at 220 °C.

A.2 Computational Methods

For the UV-Vis and experimental correlation study, the structures of all species were optimized using Gaussian 09¹³³ employing the B3LYP^{131,132} exchange-correlation (XC) functional. The LanL2DZ basis set/effective core potential¹³⁴ was used on Re and, the all-electron TZVP basis set¹³⁵ for the remaining lighter atoms. Frequency analysis of all structures was used to confirm the nature of the stationary points. Solvent effects were computed using the integral equation formalism variant of the PCM solvation model within Gaussian 09 for both the ground state and excited state TD-DFT calculations with DMSO as the solvent.^{138,139} The UV-Vis absorption spectra were extracted using the Chemissian software.²⁰³ In these calculations, a pseudo-Voigt band shape was employed with a default average band width at half-height of 2000cm⁻¹.

For the mechanism study, the ground and transition state structures and energies of all species were obtained by using TurboMole 6.5 software^{163,164} with the TPSS meta-GGA XC functional.¹⁶⁵ The def2-TZVP basis set was used for all atoms.^{135,166} The TurboMole program contains a number of optimizations to the original DFT algorithms,¹⁶⁷⁻¹⁷⁵ decreasing the calculation time without compromising accuracy. Grimme's dispersion cor-

rection (version 3) was included in the calculations.¹⁷⁶ Intermediates and transition states were verified by frequency analysis.^{172,177,178} The effects of solvation was calculated using the Conductor-like Screening Model (COSMO) implemented in TurboMole,¹⁷⁹ which is a continuum solvation model implicitly surrounding the solute molecule.

A.3 X-ray Crystallography

Crystals were mounted on thin glass fibers using paraffin oil. Prior to data collection crystals were cooled to 200.15K. Data were collected on a Bruker AXS SMART single crystal diffractometer equipped with a sealed Mo tube source (wavelength 0.71073 Å) APEX II CCD detector. Raw data collection and processing were performed with APEX II software package from BRUKER AXS53.²⁰⁴ Diffraction data for sample **3** was collected with a sequence of 0.5° ω scans at 0, 120, and 240° in ϕ . Due to lower unit cell symmetry in order to ensure adequate data redundancy, diffraction data for **1**, **2** and **8** were collected with a sequence of 0.5° ω scans at 0, 90, 180 and 270° in ϕ . Initial unit cell parameters were determined from 60 data frames with 0.3° ω scan each collected at the different sections of the Ewald sphere. Semi-empirical absorption corrections based on equivalent reflections were applied.²⁰⁵ Systematic absences in the diffraction data-set and unit-cell parameters were consistent with triclinic P $\bar{1}$ ($\mathcal{N}^{\mathcal{O}}2$) for compounds **1**, **2** and **8**, monoclinic C2/c ($\mathcal{N}^{\mathcal{O}}15$) for compound **3**. Solutions in the centrosymmetric space groups for all compounds yielded chemically reasonable and computationally stable results of refinement. The structures were solved by direct methods, completed with difference Fourier synthesis, and refined with full-matrix least-squares procedures based on F^2 .

Solutions for **1** and **2** revealed that both these structures contain two compound molecules per asymmetric unit.

Initial refinement results for the compound **1** suggested presence of two non-merohedrally twinned domains. Two independent orientation matrices were found using CELL_NOW software.²⁰⁶ Data set was re-integrated with two independent orientation matrices and consecutive model refinement was performed using HKLF5 format reflection data file. Twinning domain ratio coefficient (BASF) was successfully refined to 0.3794.

On the final model refinement stage for compound **2** thermal motion parameters for coordinated CO (-C(33)=O(3)) and Cl (Cl(2)) moieties as well as presence of unusually strong residual electron density peaks in one of the compound molecules suggested a positional CO / Cl disorder not related by symmetry. Disorder was successfully modeled with refined occupation ratio at one position CO / Cl = 70%:30%. Disorder of the second position was inversed in such way that overall occupancy summed up to one full CO and one full Cl ligands in the first coordination sphere of Re metal center. Set of geometrical (SADI) and thermal motion (SIMU, DELU) restraints were applied to achieve acceptable molecular fragment geometries and thermal motion parameter values.

For all the compounds hydrogen atoms positions were initially assigned from the residual electron density peaks coordinates. However, after initial placement all hydrogen atoms were treated as idealized contributions during the refinement. All scattering factors are contained in several versions of the SHELXTL program library, with the latest version used being v.6.12.²⁰⁷

X-Ray crystal structures are shown in Appendix B

A.4 (**terpy- $\kappa^2\text{-N,N'}$**)Re(CO)₃Cl (**2.1**)

Re(CO)₅Cl (201 mg, 0.556 mmol) and 2,2:6,2 terpyridine (129 mg, 0.553 mmol) were mixed in 60 mL of toluene. The reaction mixture was heated to 100C for 1 hour under N₂. During this time the solution turned a bright red. Upon cooling a yellow precipitate

was formed. The solution was filtered, and the solid was washed with diethyl ether, and dried under vacuum. Compound **1** is a bright yellow powder that was isolated in 70 % yield (208 mg). Crystals were obtained from chloroform with addition of a small amount of hexanes as counter solvent. TGA: 8 % mass loss from 240-280 °C. FTIR: 2019, 1981, 1889 cm⁻¹ (*v* C=O). ¹H NMR (CD₃CN, 400 MHz): δ 9.06 (ddd, J=5.6, 1.7, 0.8 Hz, 1H), 8.77 (ddd, J=4.9 Hz, 1H), 8.49 (td, J=8.2, 1.5 Hz, 2H), 8.28 (t, J=7.9 Hz, 1H), 8.22 (td, J=8.1, 1.6 Hz, 1H), 7.96 (td, J=7.8, 1.8 Hz, 1H), 7.79 (dt, J=7.8, 1.1 Hz, 1H), 7.80 (dd, J=7.7, 1.0 Hz, 1H), 7.63 (ddd, J=7.6, 5.5, 1.2 Hz, 1H), 7.55 (ddd, J=7.6, 5.0, 1.0 Hz, 1H). Elemental analysis calculated (%) for [C₁₈H₁₁ReClN₃O₃]: C 40.11, H 2.06, N 7.80, found C 39.96, H 2.09, N 7.69.

A.5 (terpy- κ^3 -N,N',N'')Re(CO)₂Cl (2.2)

Compound **2.1** (101 mg, 0.187 mmol) was placed in a tube furnace and heated to 240 °C under N₂ flow for 60 minutes. A black solid was collected (90 mg) at 94 % yield based on the formula for **2**. Crystals were obtained from chloroform with addition of a small amount of hexanes as counter solvent. FTIR: 1872, 1788 cm⁻¹ (*v* C=O). ¹H NMR (CD₃CN, 400 MHz): δ 8.70 (ddd, J=4.7, 1.8, 0.9 Hz, 2H), 8.65 (dt, J=8.0, 1.0, 1.0, 2H), 8.47 (d, J=7.8 Hz, 2H), 8.03 (t, J=7.8 Hz, 1H), 7.95 (td, J=7.7, 7.7, 1.9 Hz, 2H), 7.43 (ddd, J=7.5, 4.8, 1.2 Hz, 2H). Elemental analysis calculated (%) for [C₁₇H₁₁ReClN₃O₂]: C 39.96, H 2.17, N 8.22, found C 39.62, H 2.09, N 7.99.

A.6 (terpy- κ^2 -N,N')Re(CO)₃Br (2.3)

Re(CO)₅Br (191 mg, 470 mmol) and 2,2:62 terpyridine (129 mg, 0.553 mmol) were allowed to react under conditions analogous to the preparation of **1**. A bright yellow

powder was obtained, 0.223 g (0.382 mmol, 81 %). FTIR: 2012, 1910, 1886 cm⁻¹ (*v* C=O). ¹H NMR (CD₃CN, 400 MHz): δ 9.07 (ddd, J=5.6, 1.6, 0.9 Hz, 1H), 8.77 (ddd, J=4.6, 1.5, 0.8 Hz, 1H), 8.52 – 8.48 (m, 2H), 8.28 (t, J=7.9 Hz, 1H), 8.21 (td, J=8.0, 1.6 Hz, 1H), 7.97 (td, J=7.8, 1.8 Hz, 1H), 7.80 – 7.75(m, 2H), 7.63 (ddd, J=7.6, 5.5, 1.2 Hz, 1H), 7.55 (ddd, J=7.7, 4.9, 1.1 Hz, 1H). Elemental analysis calculated (%) for [C₁₈H₁₁ReBrN₃O₃]: C 37.06, H 1.90, N 7.20, found C 36.94, H 1.92, N 7.00.

A.7 (terpy- κ^3 -N,N',N'')Re(CO)₂Br (2.4)

Compound **2.3** (182 mg, 0.312 mmol) was placed in an tube furnace and heated to 230 °C under N₂ flow for 60 minutes. A black solid was collected, 0.155 mg (0.279 mmol, 89 % yield). Crystals were obtained from chloroform with addition of a small amount of hexanes as counter solvent. FTIR: 1873, 1794 cm⁻¹ (*v* C=O). ¹H NMR (CD₃CN, 400 MHz): δ 8.95 (d, J=5.4 Hz, 2H), 8.24 (t, J = 8.1Hz, 4H), 8.05 (dd, J=8.2, 7.7 Hz, 1H), 7.90(td, J=7.9, 1.7 Hz, 2H), 7.63 (ddd, J=7.3, 5.5, 1.2 Hz, 2H). Elemental analysis calculated (%) for [C₁₇H₁₁ReBrN₃O₂]: C 36.76, H 2.00, N 7.57, found C 36.66, H 2.00, N 7.50.

A.8 (terpy- κ^2 -N,N')Re(CO)₃CN (2.5)

To **2.3** (60 mg, 0.103 mmol), AgCF₃SO₃ (40 mg, 0.299 mmol) was added in 10 mL CH₂Cl₂. The reaction was stirred 18 h and kept dark under N₂ atmosphere. Solution was filtered to remove salts, then reduced in volume. Cold diethyl ether was used to precipitate product. Yellow-grey powder (**7a**) was collected by filtration, yielding 48mg (88 %). Crystals were grown from saturated chloroform with hexanes as countersolvent for X-ray crystallography. FTIR: 2013, 1905, 1884 cm⁻¹ (*v* C=O). ¹H NMR (CD₃CN,

400 MHz): δ 9.08 (dd, $J=5.40$, 0.49 Hz, 1 H), 8.78 (dd, $J=5.10$, 0.59 Hz, 1 H), 8.53 (dd, $J=8.18$, 0.93 Hz, 1 H), 8.50 (d, $J=8.23$ Hz, 1 H), 8.30 (t, $J=7.90$ Hz, 1 H), 8.23 (td, $J=7.94$, 1.57 Hz, 2 H), 7.98 (td, $J=7.76$, 1.71 Hz, 1 H), 7.80 (dd, $J=7.79$, 1.03 Hz, 1 H), 7.77 (d, $J=7.74$ Hz, 0 H), 7.64 (ddd, $J=7.50$, 5.50, 1.08 Hz, 1 H), 7.55 (ddd, $J=7.62$, 4.92, 0.98 Hz, 2 H). Elemental analysis calculated (%) for [C₁₉H₁₁N₄O₃Re]: C 43.10, H 2.09, N 10.58, found C 40.06, H 2.06, N 9.85.

A.9 (**terpy- κ^3 -N,N',N''**)Re(CO)₂CN (2.6)

Compound **2.5** (108 mg, 0.204 mmol) was placed in an tube furnace and heated to 220 °C under N₂ flow for 60 minutes. A black solid was collected, 88 mg (0.175 mmol, 86 % yield). ¹H NMR (CD₃CN, 400 MHz): δ 8.60(ddt, $J=4.8$, 1.7, 0.8, 0.8 Hz, 2H), 8.48 (dq, $J=8.0$, 1.0 Hz, 2H), 8.37 (dd, $J=7.9$, 0.8 Hz, 2H), 8.07 (dd, $J=8.0$, 7.6 Hz, 1 H), 7.94 (ddd, $J=7.9$, 7.5, 1.8 Hz, 2H) 7.43 (ddd $J=7.4$, 4.8, 1.2 Hz, 2H). Elemental analysis calculated (%) for [C₁₈H₁₁N₄O₂Re]: C 43.11, H 2.21, N 11.17, found C 40.26, H 2.67, N 9.60.

A.10 (**terpy- κ^2 -N,N'**)Re(CO)₃OTf (2.7)

To **2.1** (80 mg, 0.148 mmol), AgCF₃SO₃ (46 mg, 0.179 mmol) was added in 10 mL CH₃CN. The reaction was stirred 18 h and kept dark. Solution was filtered to remove salts, then reduced in volume. Cold diethyl ether was used to precipitate product. Yellow-grey powder (**7a**) was collected by filtration, yielding 38 mg (40 %). Crystals were grown from saturated chloroform with hexanes as countersolvent for X-ray crystallography. FTIR: 2030, 1895, 1890 cm⁻¹ (ν C=O), 1280, 1228, 1204 cm⁻¹ (ν SO₃). ¹H NMR (CD₃CN, 400 MHz): δ 9.05 (ddd, $J=5.5$, 1.6, 0.8 Hz, 1H), 8.79 (ddd, $J=4.9$, 1.8, 1.1 Hz, 1H), 8.57

(dd, $J=8.1$, 0.9 Hz, 1H), 8.54 (dt, $J=8.2$, 1.1 Hz, 1H), 8.37 (t, $J=7.9$ Hz, 1H), 8.31 (td, $J=8.0$, 1.6 Hz, 1H), 8.03 (td, $J=7.7$, 1.7 Hz, 1H), 7.87 (dd, $J=7.8$, 1.0 Hz, 1H), 7.75 (dt, $J=7.8$, 1.1 Hz, 1H), 7.72 (ddd, $J=7.4$, 5.9, 1.1 Hz, 1H), 7.61 (ddt, $J=7.7$, 4.8, 0.5, 0.5 Hz, 1H). Elemental analysis calculated (%) for $[C_{19}H_{11}ReN_3O_6F_3S]$: C 34.97, H 1.70, N 6.44, found C 31.80, H 1.73, N 5.33.

Alternately, to **1** (72 mg, 0.134 mmol) was added 10 mL CF_3SO_3H (excess) and temperature was increased to 100 °C for 20 minutes. A black solution was neutralized with addition of 5% Na_2CO_3 in H_2O . Product was extracted with $CHCl_3$, then dried under vacuum to yield a brown solid (**7b**) (47 mg, 54 %).

A.11 (**terpy- κ^3 -N,N',N''**)Re(CO)₂OTf (2.8)

To **2.2** (77 mg, 0.143 mmol), $AgSO_3CF_3$ (47 mg, 0.183 mmol) was added in 15 mL CH_3CN . Solution was refluxed for 6 h in the dark under N_2 atmosphere. Solution was filtered, then reduced to minimal volume. Cold diethyl ether was added dropwise to precipitate product. Collected by filtration and washed with additional cold ether, yielding 75 mg (120 mmol, 80 %). Crystals grown from saturated methylene chloride, with hexanes as countersolvent for x-ray crystallography. FTIR: 1910, 1829 cm^{-1} (v C=O), 1259, 1224, 1143 cm^{-1} (v SO₃). ¹H NMR (CD_3CN , 400 MHz): δ 8.91(ddd, $J=5.6$, 1.6, 0.7 Hz, 2H), 8.32 (d, $J=8.0$ Hz, 2H), 8.28 (ddd, $J=8.1$, 1.4, 0.8 Hz, 2H), 8.19 (dd, $J=8.8$, 7.4 Hz, 1H), 8.02 (td, $J=7.9$, 1.5 Hz, 2H) 7.46 (ddd $J=7.6$, 5.6, 1.3 Hz, 2H). Elemental analysis calculated (%) for $[C_{18}H_{11}ReF_3SN_3O_5]$: C 34.62, H 1.78, N 6.37, found C 31.02, H 1.82, N 7.11.

Appendix B

X-ray Crystal Structures

Multiple views of each x-ray crystal structure (including full unit cell) as discussed in chapter 2 are shown in Figures B.1 to B.5.

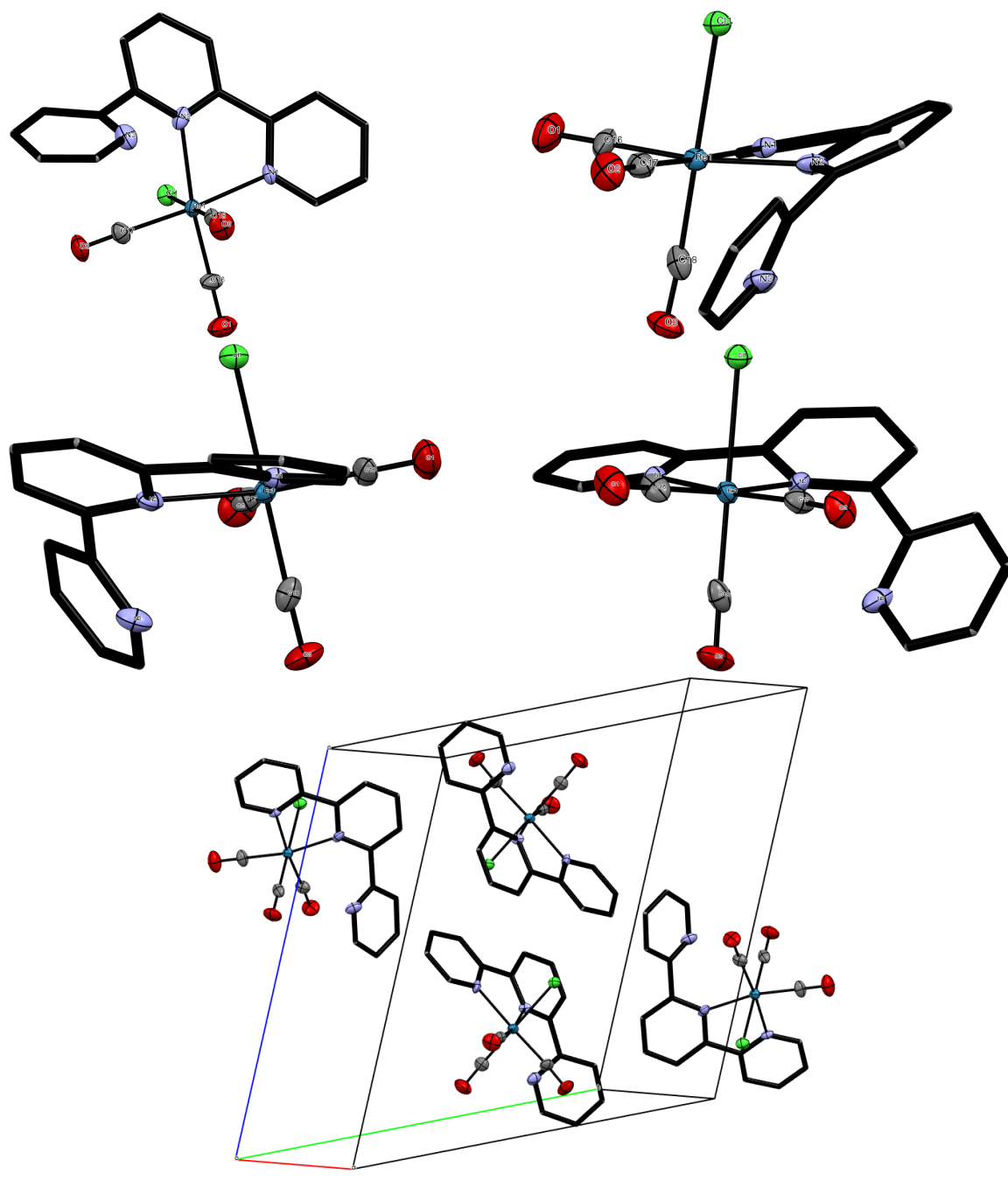


Figure B.1 X-ray crystal structure of **2.1**. Co-crystallized chloroform, hydrogen atoms, and thermal ellipsoids of ligand carbon atoms are omitted for clarity.

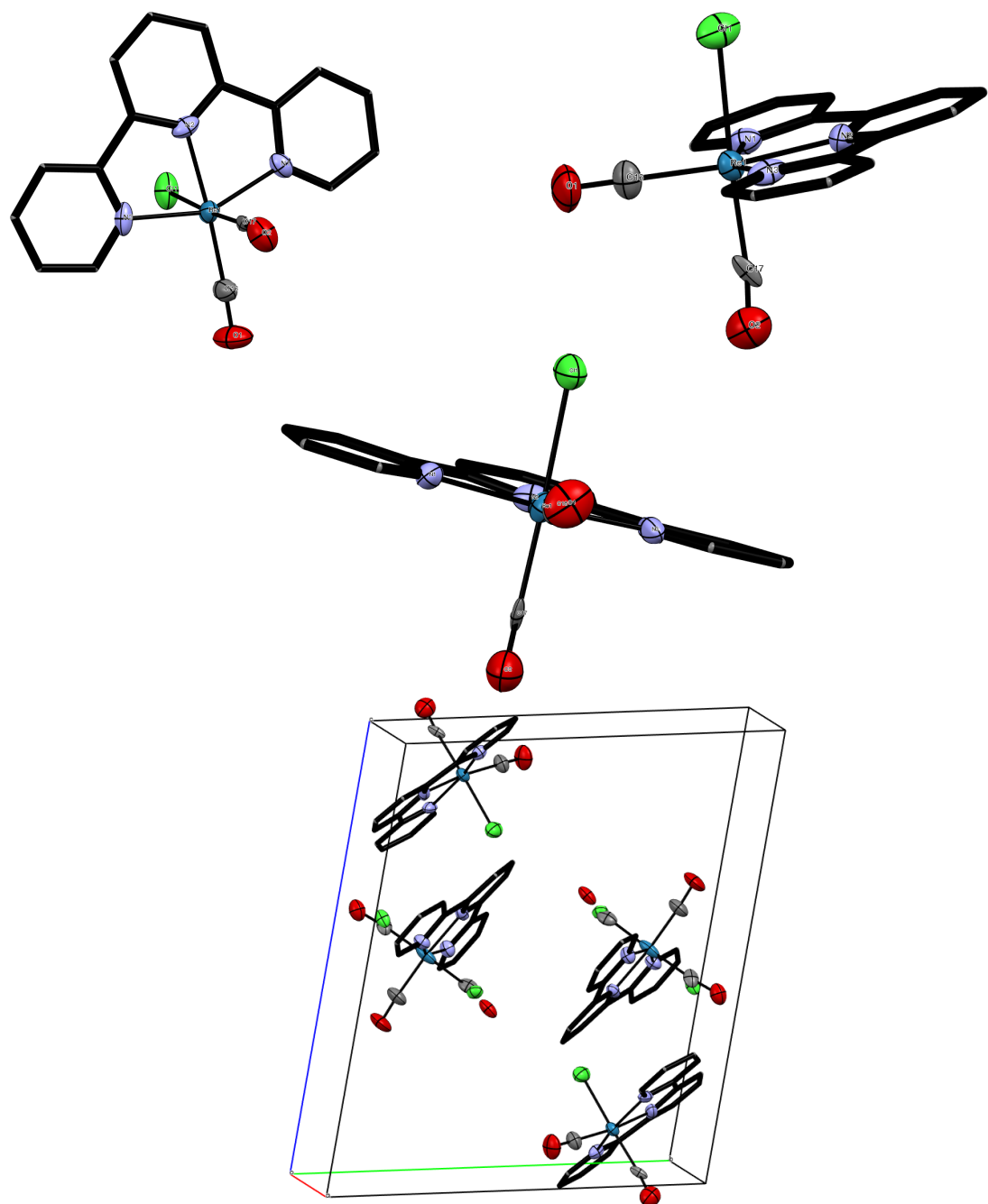
(a) Full unit cell representation of **2.2**.

Figure B.2 X-ray crystal structure of **2.2**. Co-crystallized chloroform, hydrogen atoms, and thermal ellipsoids of ligand carbon atoms are omitted for clarity.

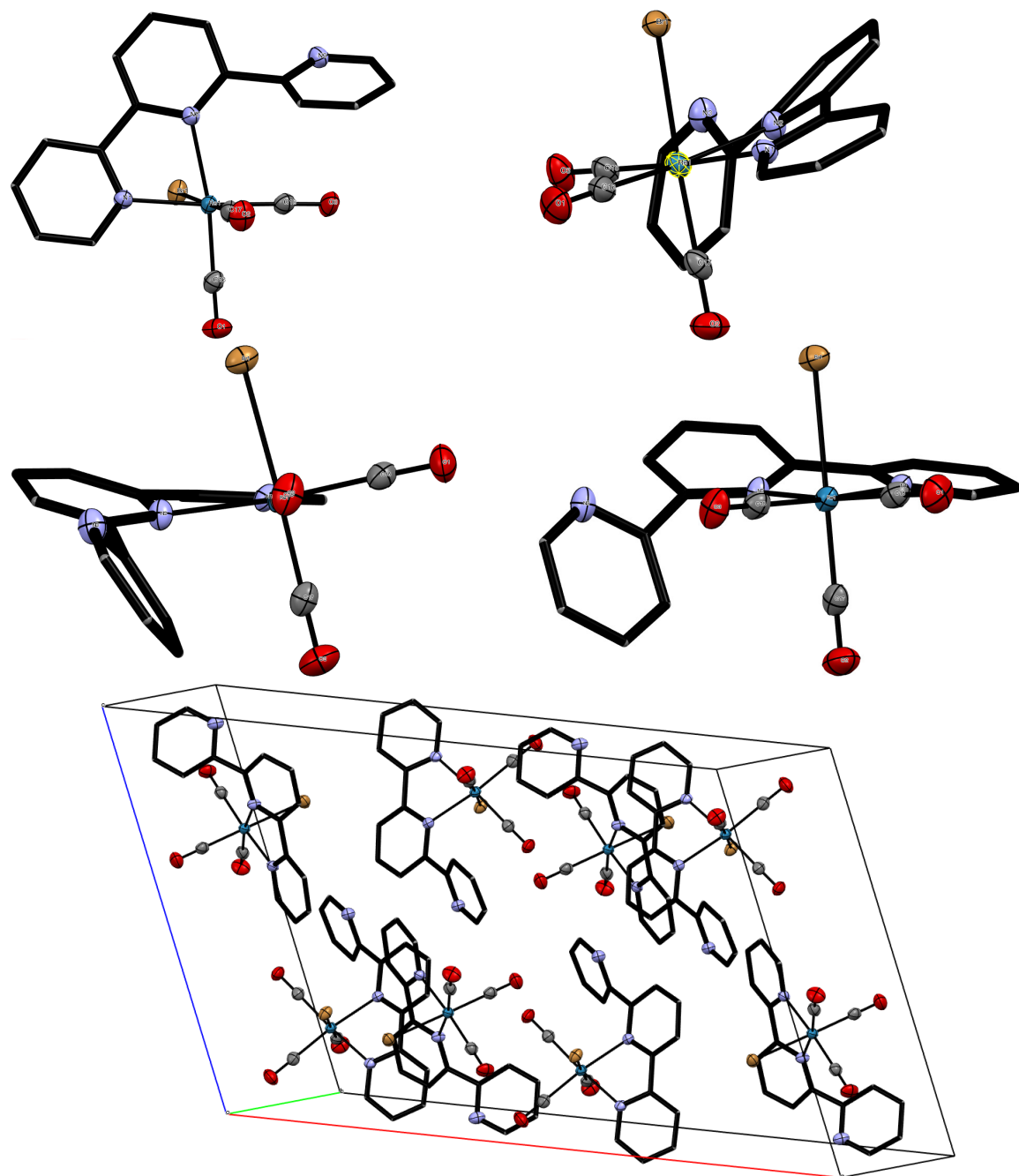
(a) Full unit cell representation of **2.3**.

Figure B.3 X-ray crystal structure of **2.3**. Hydrogen atoms, and thermal ellipsoids of ligand carbon atoms are omitted for clarity.

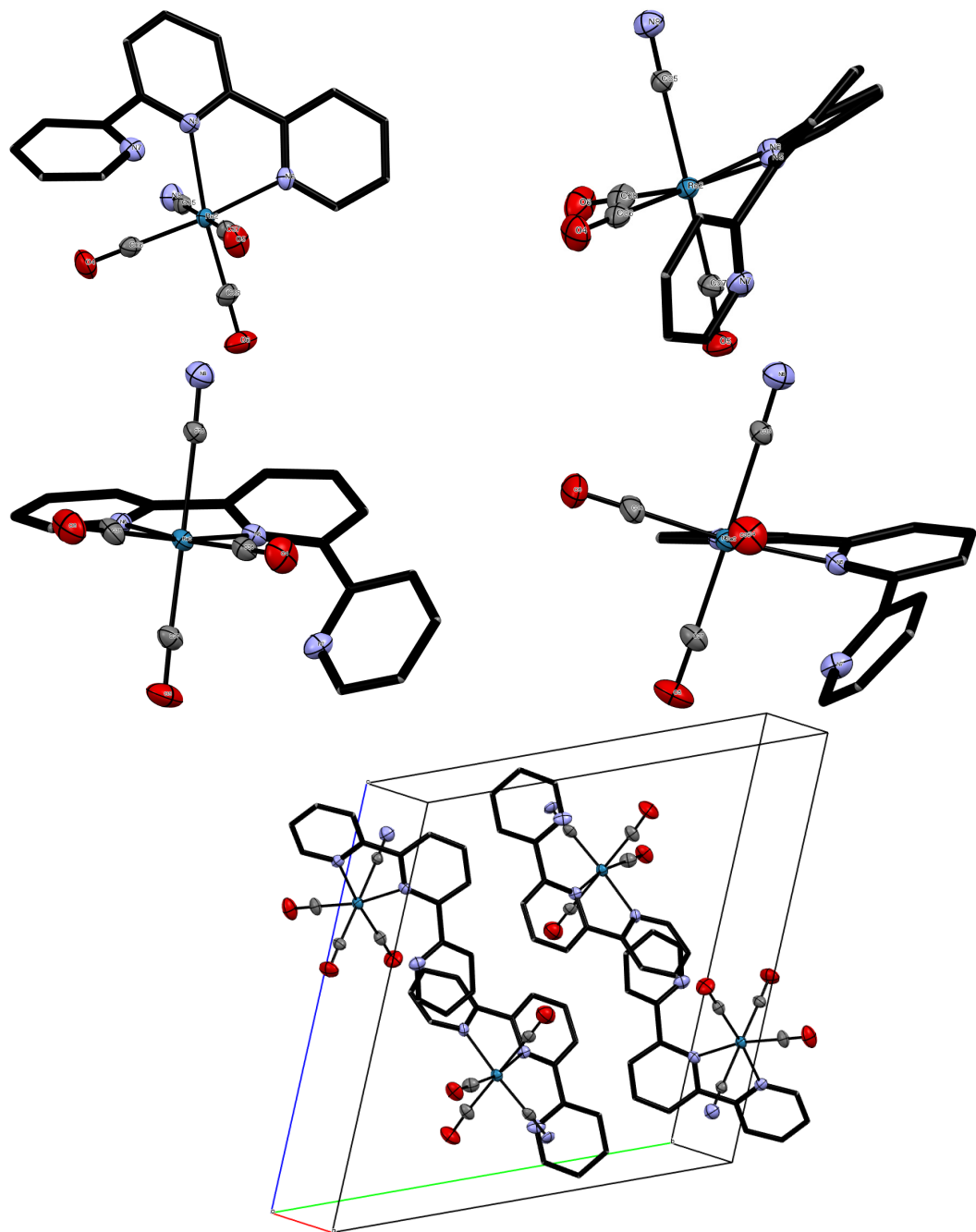
(a) Full unit cell representation of **2.5**.

Figure B.4 X-ray crystal structure of **2.5**. Hydrogen atoms, and thermal ellipsoids of ligand carbon atoms are omitted for clarity.

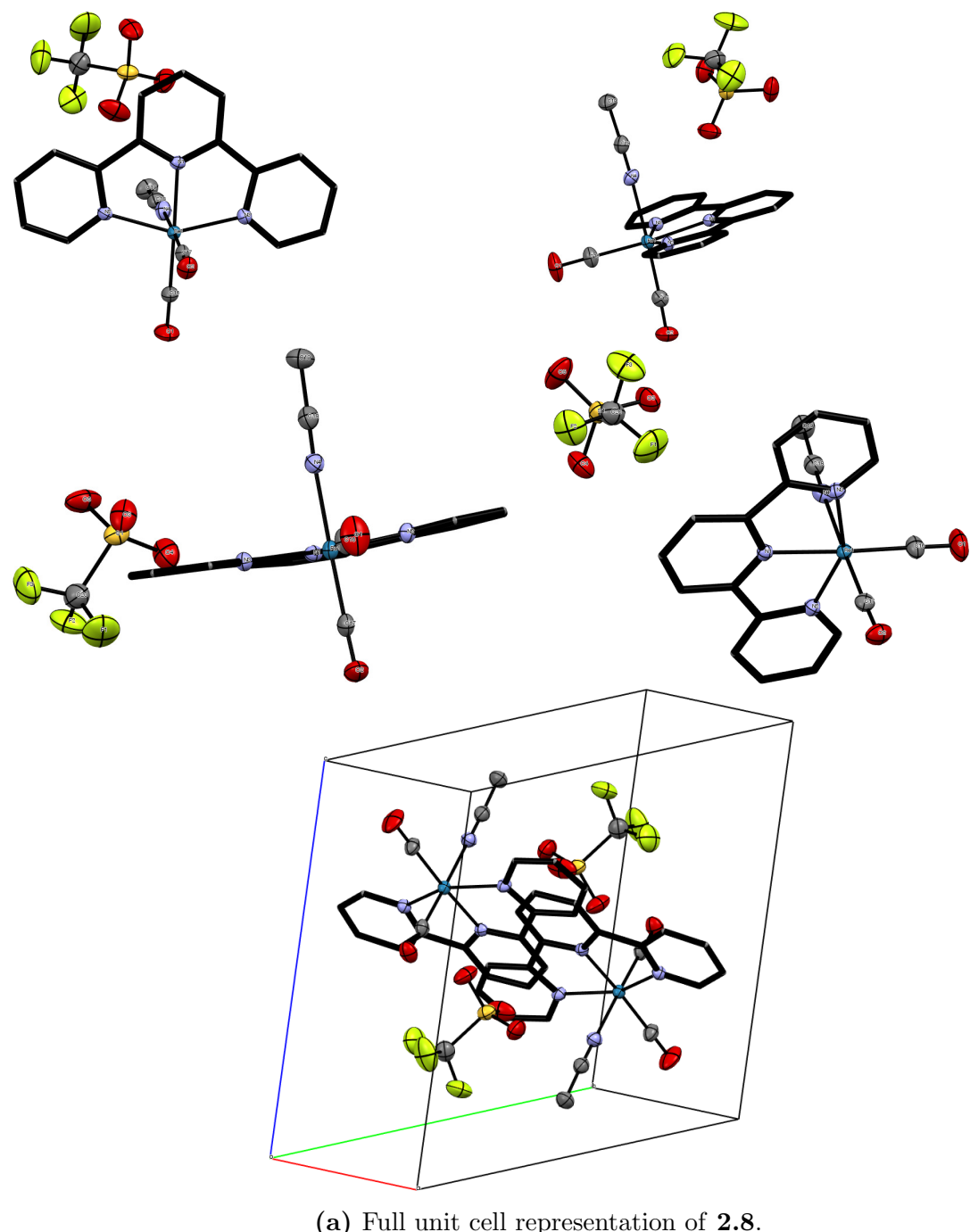
(a) Full unit cell representation of **2.8**.

Figure B.5 X-ray crystal structure of **2.8**. Hydrogen atoms, and thermal ellipsoids of ligand carbon atoms are omitted for clarity.

Appendix C

Molecular Orbitals Diagrams

Frontier Molecular Orbitals (MOs) for each compound discussed in this thesis are listed below in Figures C.1 to C.8. These orbitals are generated with the Chemissian program²⁰³ from the output of calculations performed in Gaussian 09.¹³³

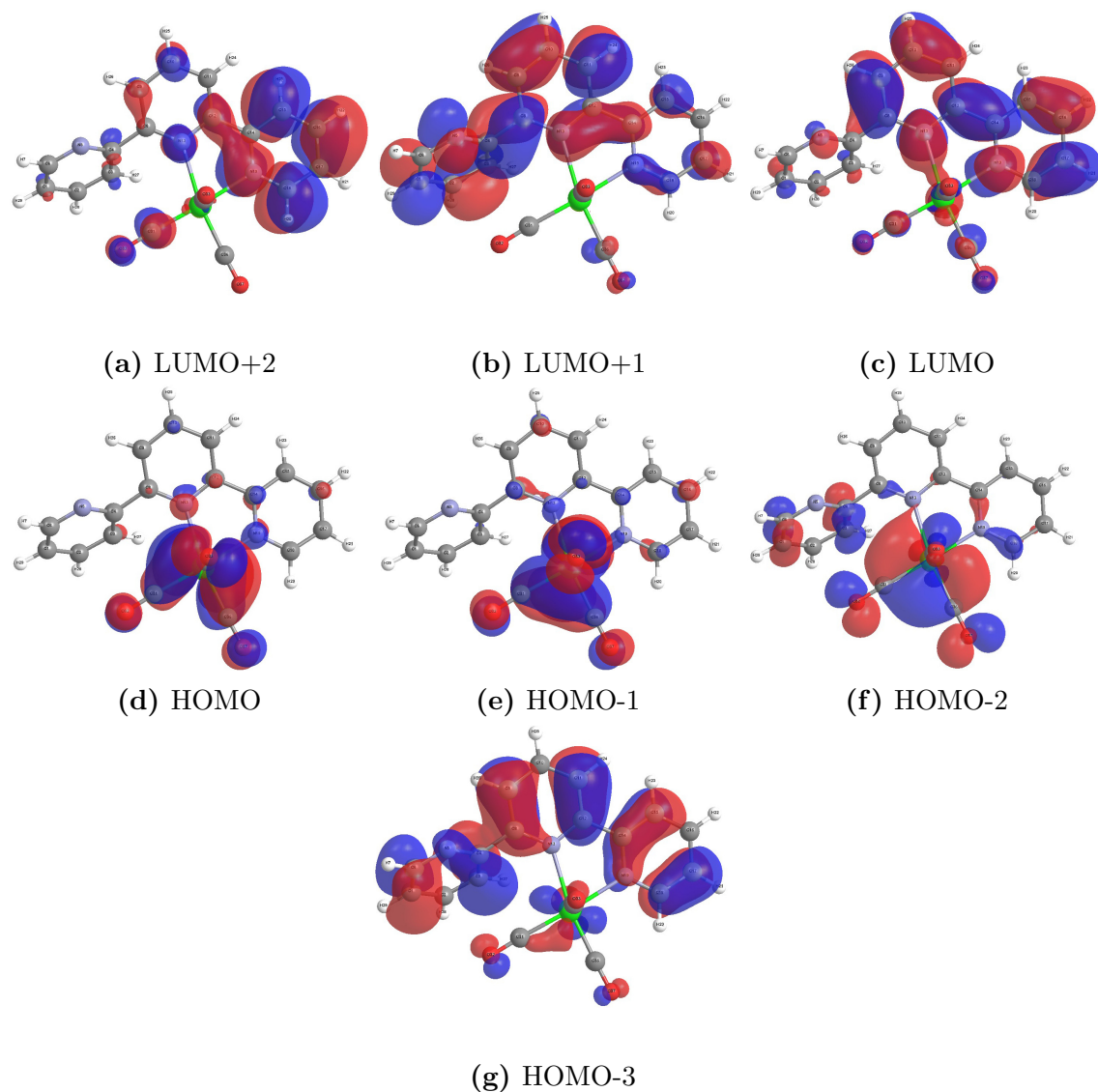


Figure C.1 Isosurface plots of the frontier molecular orbitals HOMO-3 to LUMO+2 of **2.1**.

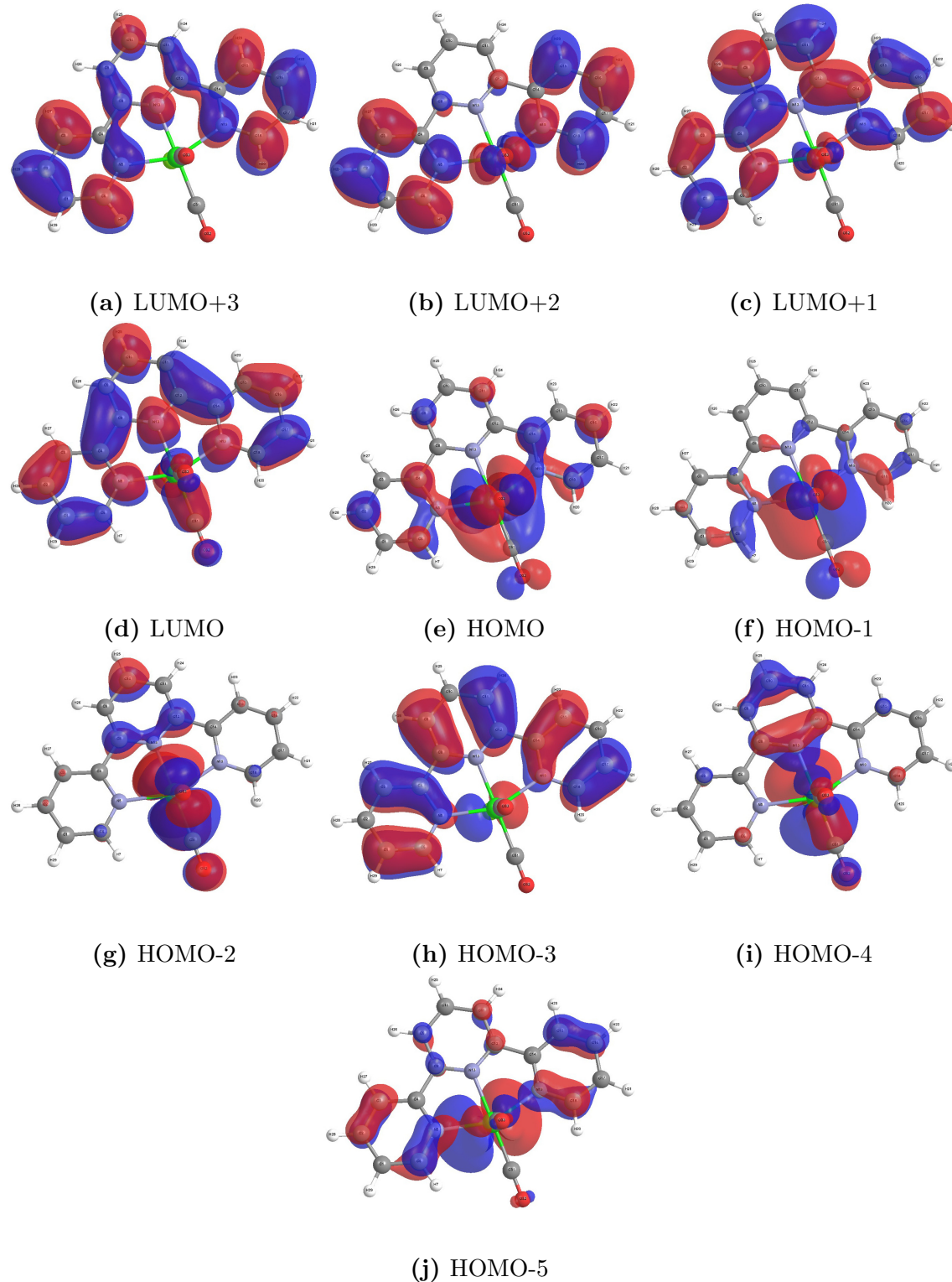


Figure C.2 Isosurface plots of the frontier molecular orbitals HOMO-5 to LUMO+3 of **2.2**.

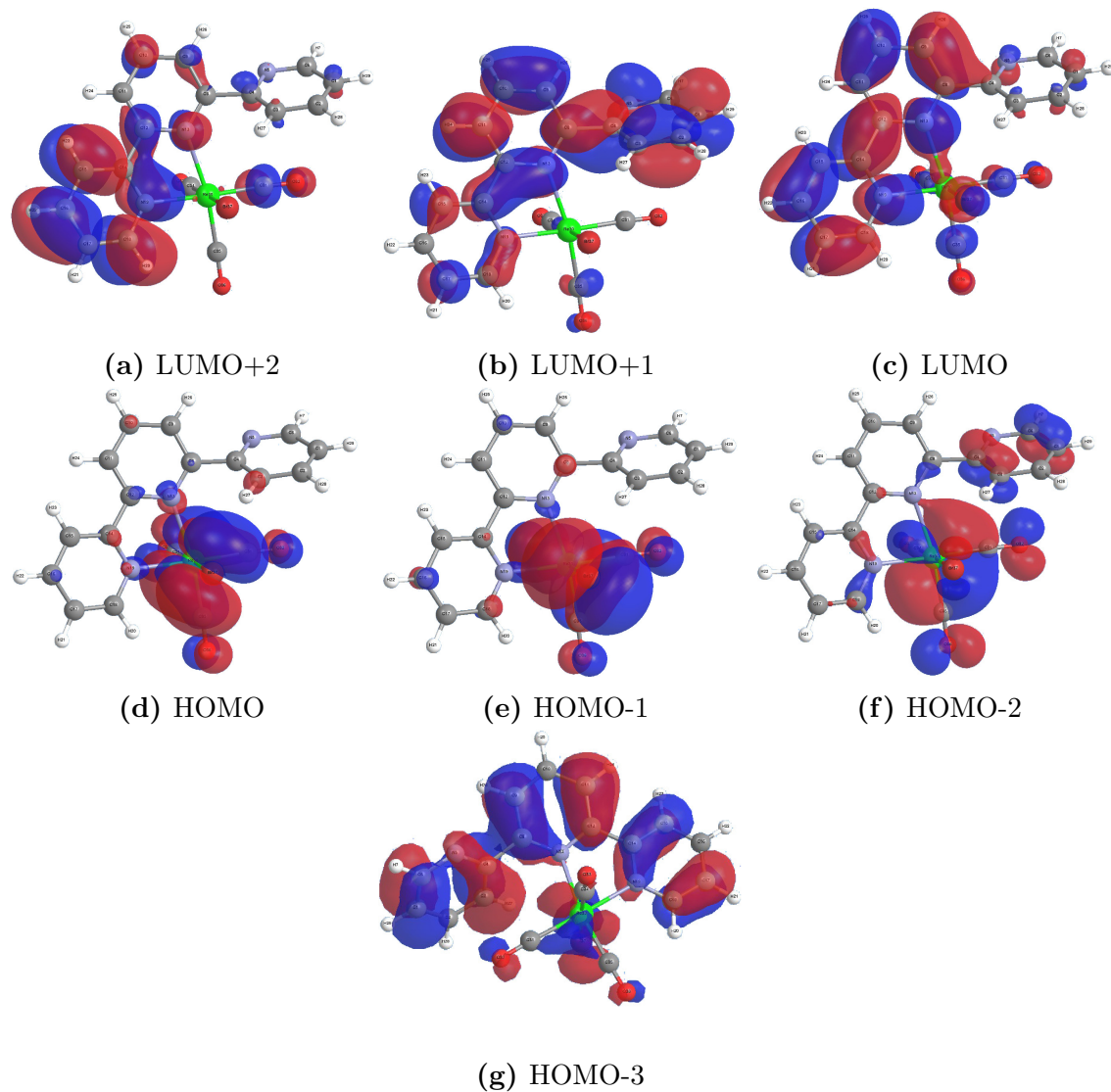


Figure C.3 Isosurface plots of the frontier molecular orbitals HOMO-3 to LUMO+2 of **2.3**.

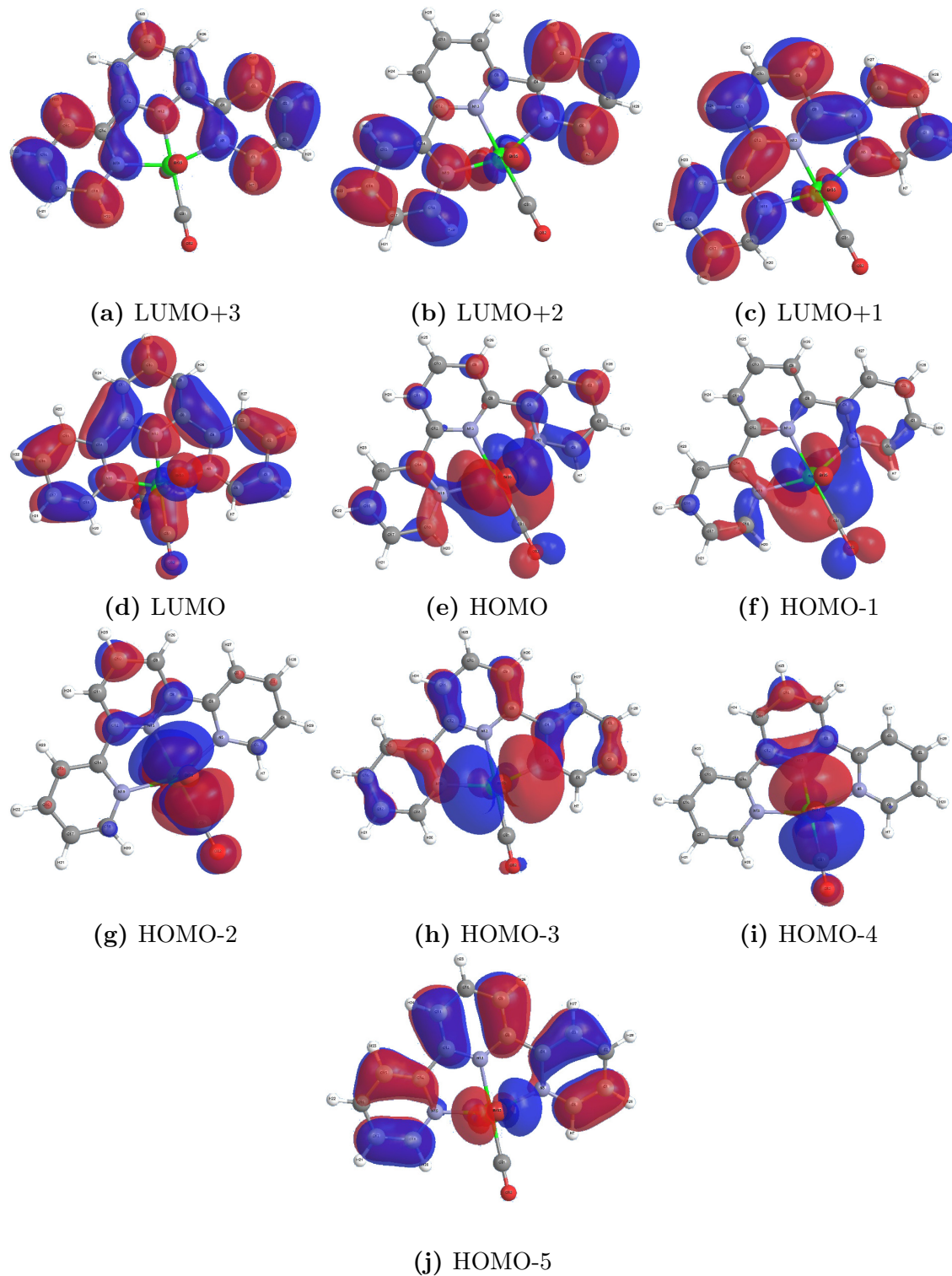


Figure C.4 Isosurface plots of the frontier molecular orbitals HOMO-5 to LUMO+3 of 2.4.

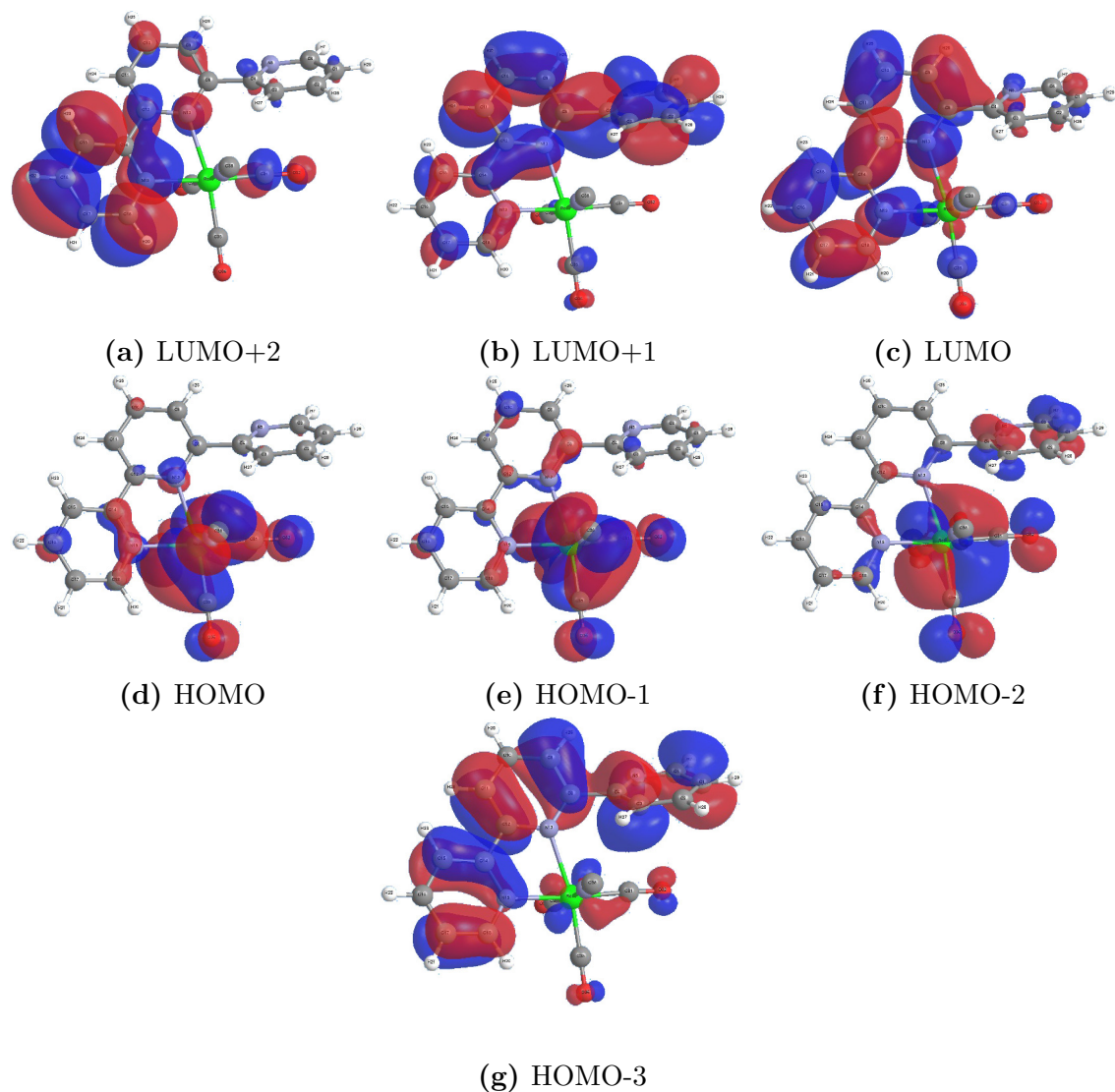


Figure C.5 Isosurface plots of the frontier molecular orbitals HOMO-3 to LUMO+2 of **2.5**.

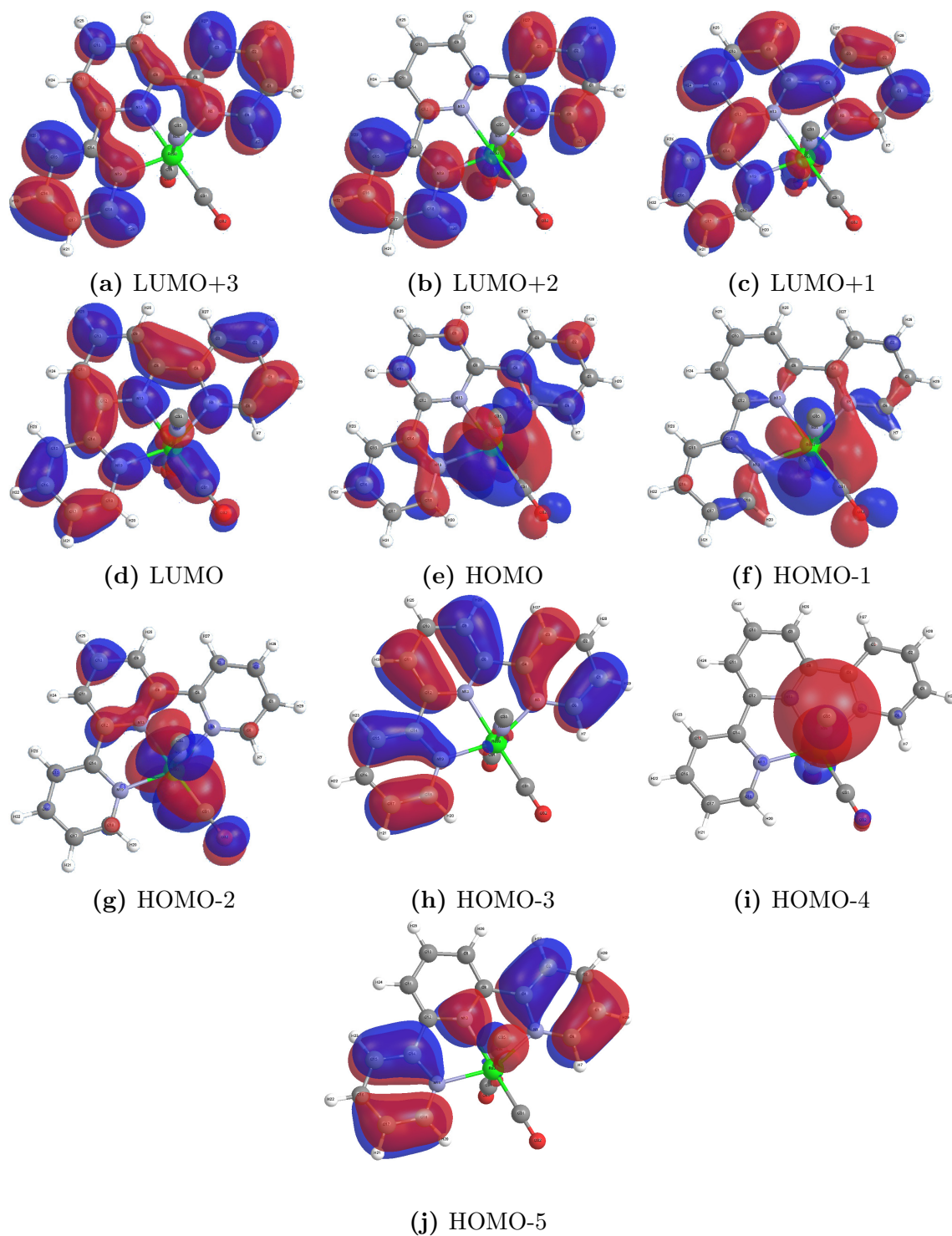


Figure C.6 Isosurface plots of the frontier molecular orbitals HOMO-5 to LUMO+3 of 2.6.

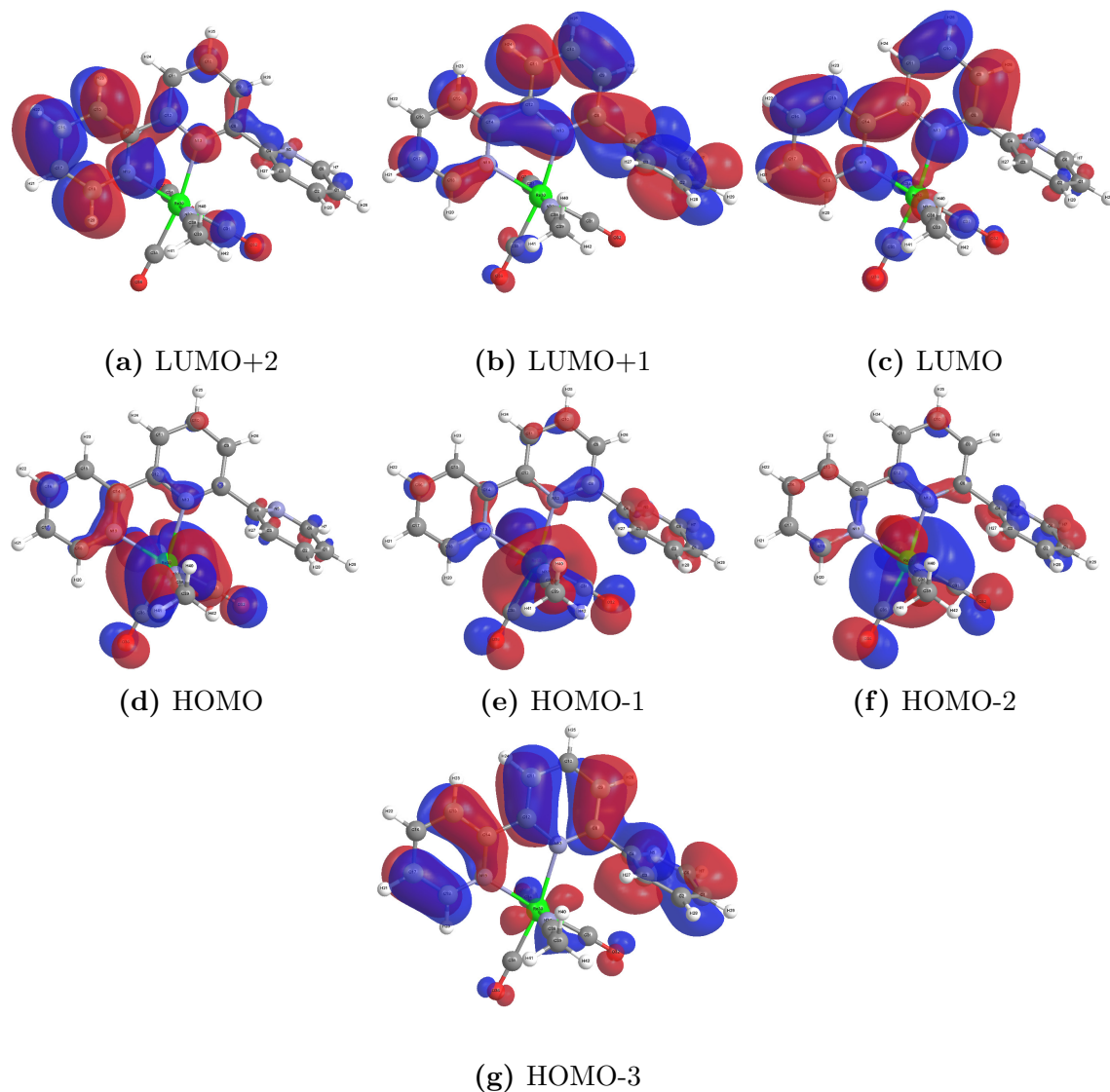


Figure C.7 Isosurface plots of the frontier molecular orbitals HOMO-3 to LUMO+2 of **2.7**.

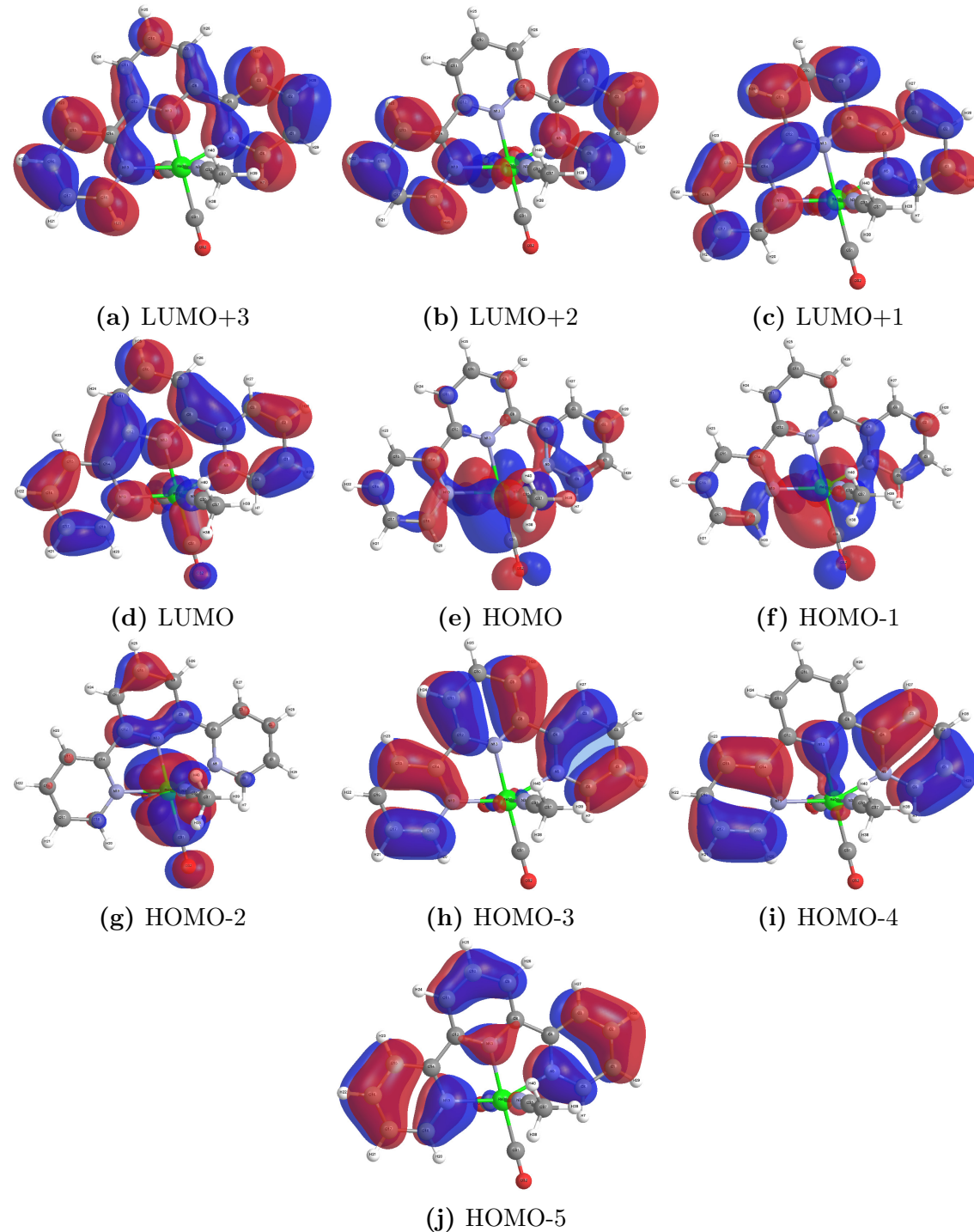


Figure C.8 Isosurface plots of the frontier molecular orbitals HOMO-5 to LUMO+3 of **2.8**.

Appendix D

Reaction Potential Energy Diagrams

Potential energy diagrams for the reactions discussed in chapter 4 are listed below in Figures D.1 to D.9.

Reaction Potential Energy Diagrams

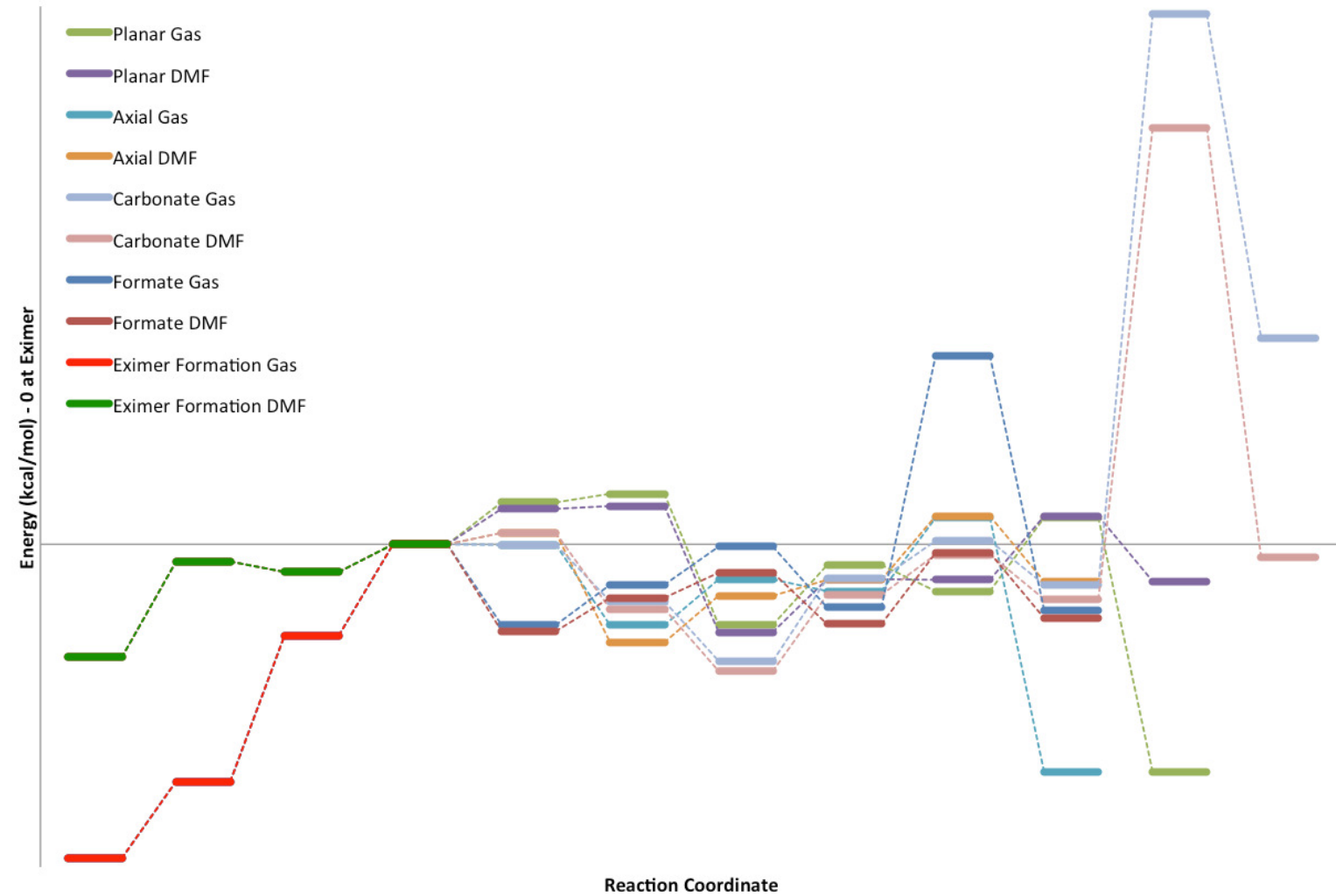


Figure D.1 An overview of the energies of the three mechanistic pathways of photochemical CO_2 reduction.

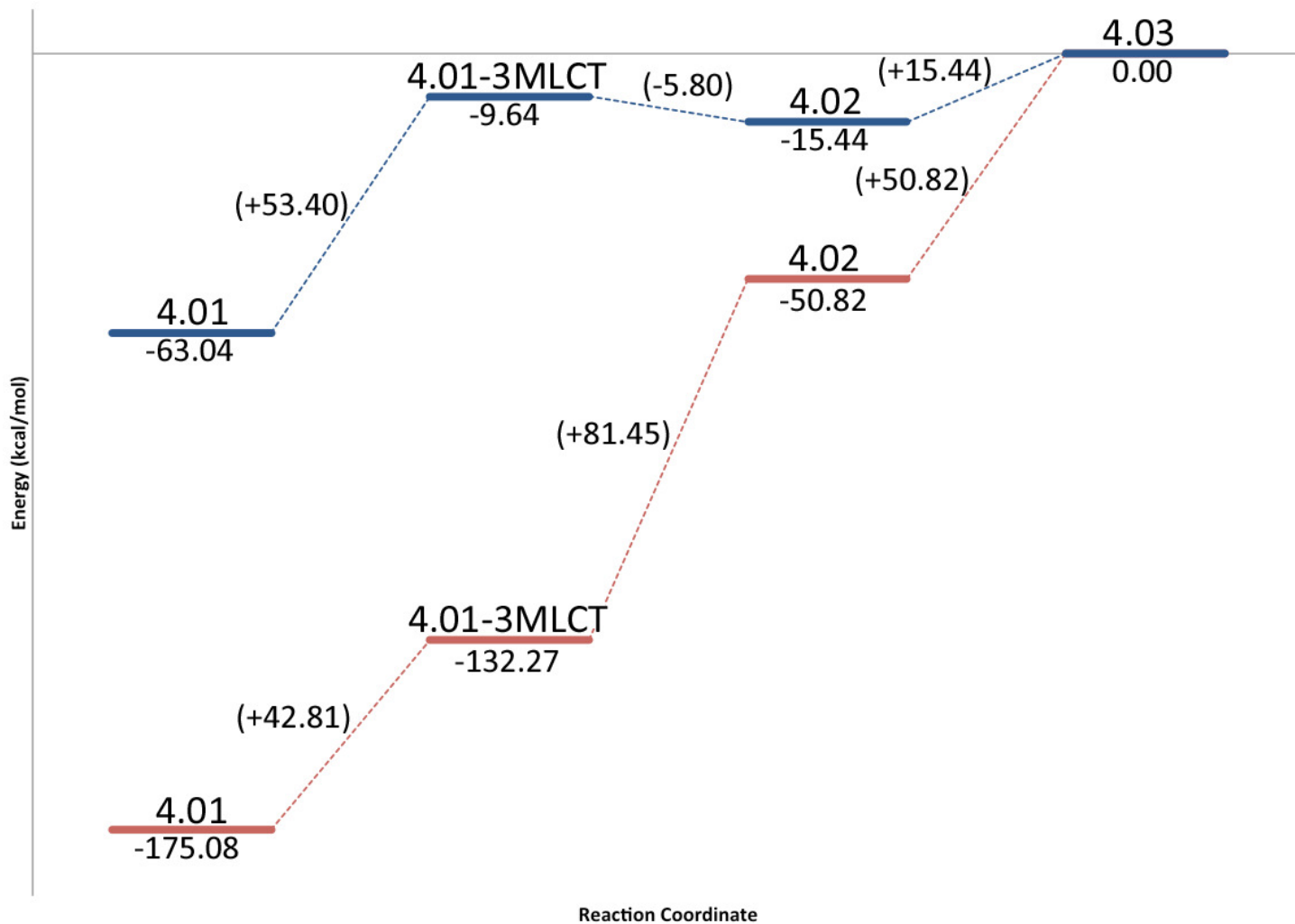


Figure D.2 Potential Energy Surface for the production of the excimer. Gas phase energies in red, DMF solvated energies in blue.

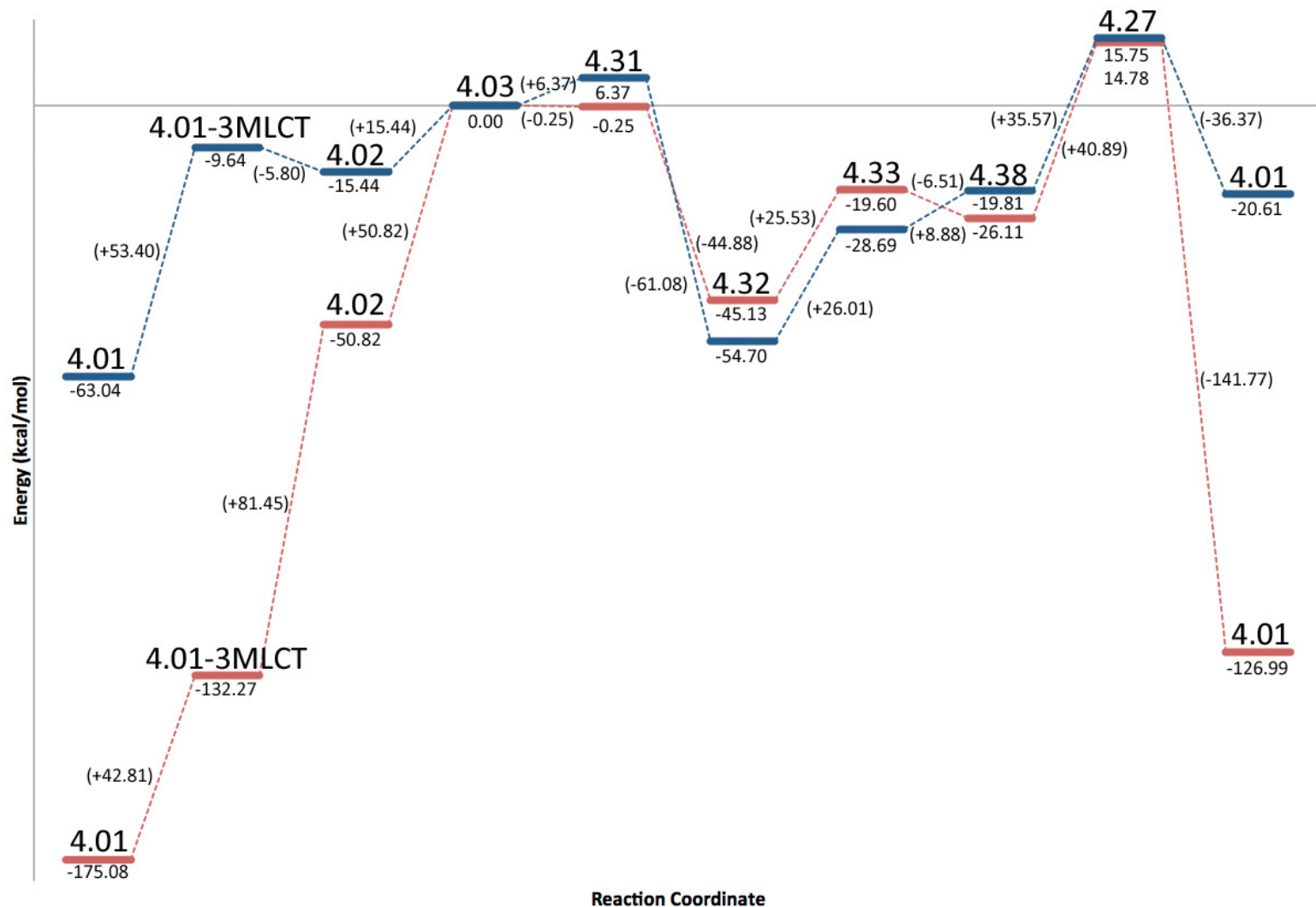


Figure D.3 Potential Energy Surface for the axial geometry of the water-gas shift mechanistic pathway. Gas phase energies in red, DMF solvated energies in blue.

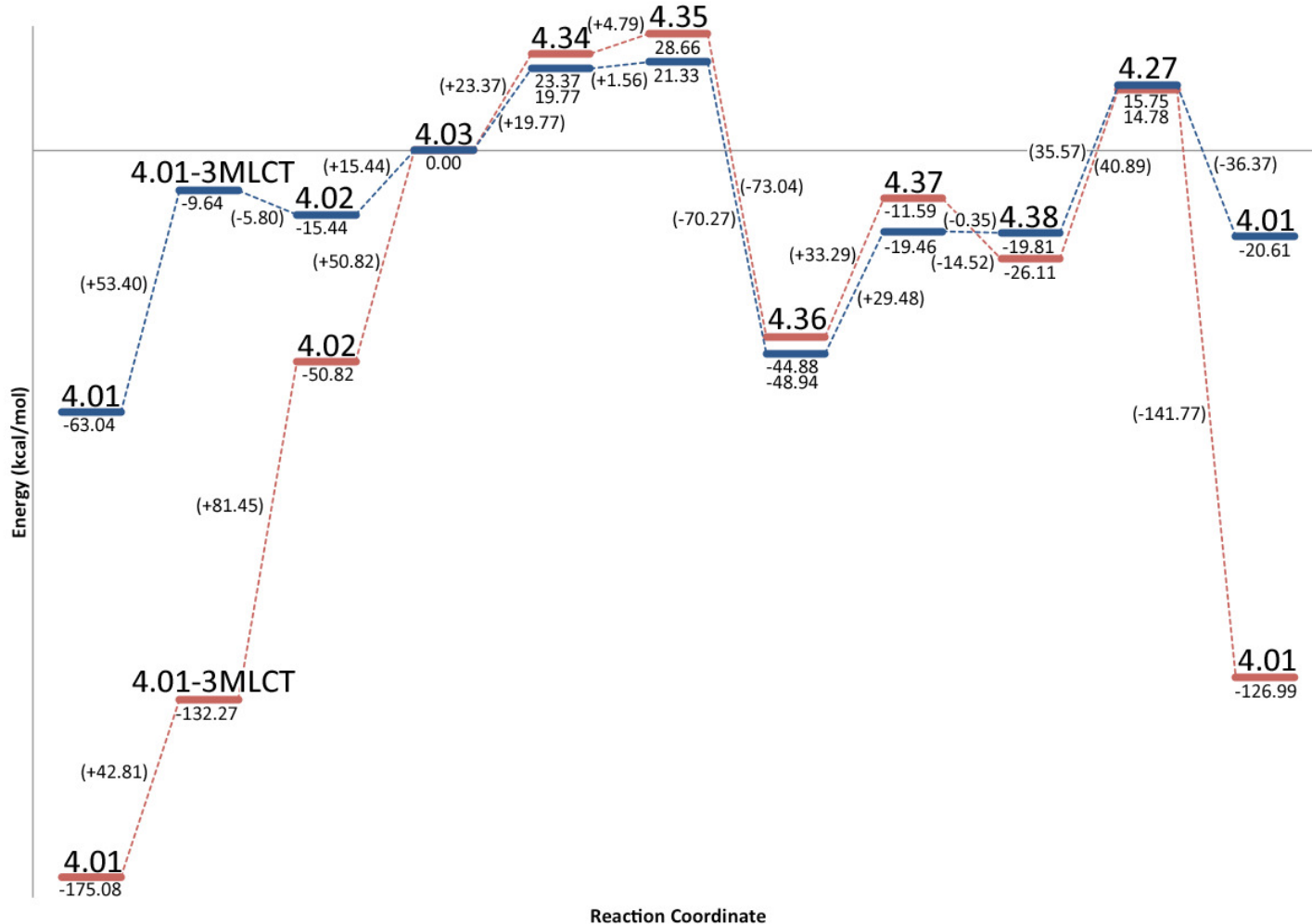


Figure D.4 Potential Energy Surface for the planar geometry of the water-gas shift mechanistic pathway. Gas phase energies in red, DMF solvated energies in blue.

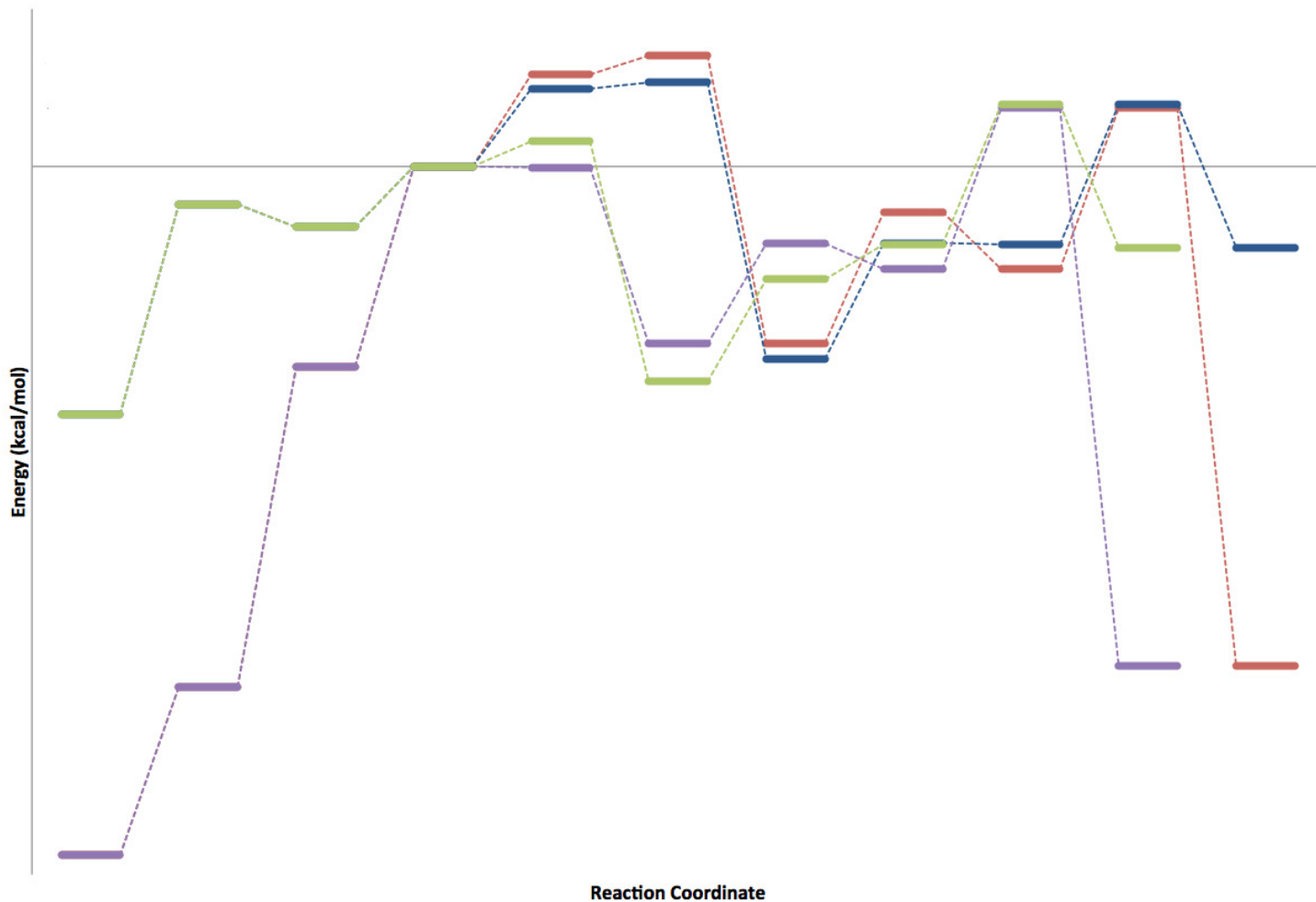


Figure D.5 Potential Energy Surface for the two water-gas shift mechanistic pathway geometries. Axial geometry energies are shown in purple (gas phase) and green (solvated phase), and planar geometries shown in red (gas phase) and blue (solvated phase).

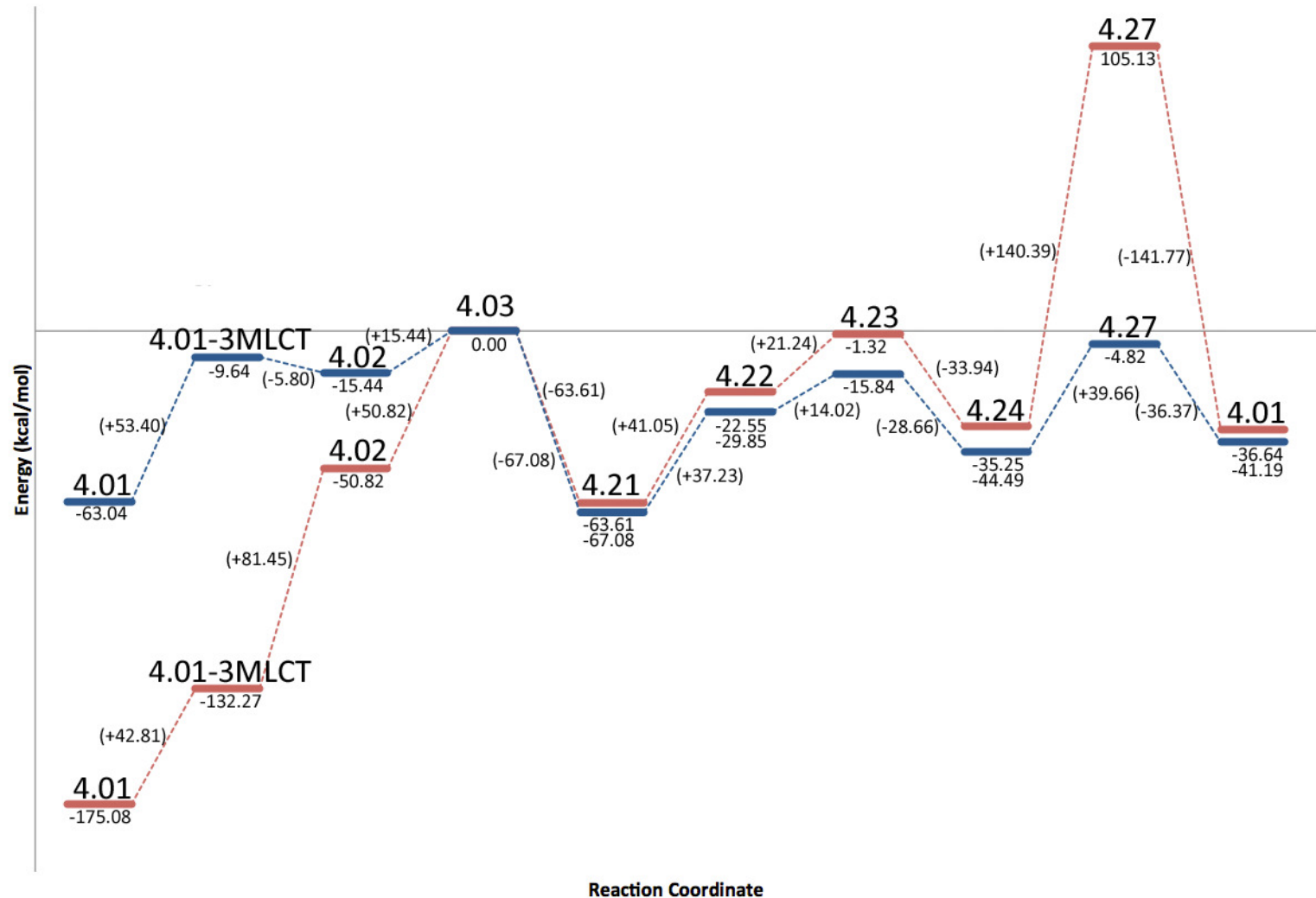


Figure D.6 Potential Energy Surface for the formate mechanistic pathway. Gas phase energies in red, DMF solvated energies in blue.

Reaction Potential Energy Diagrams

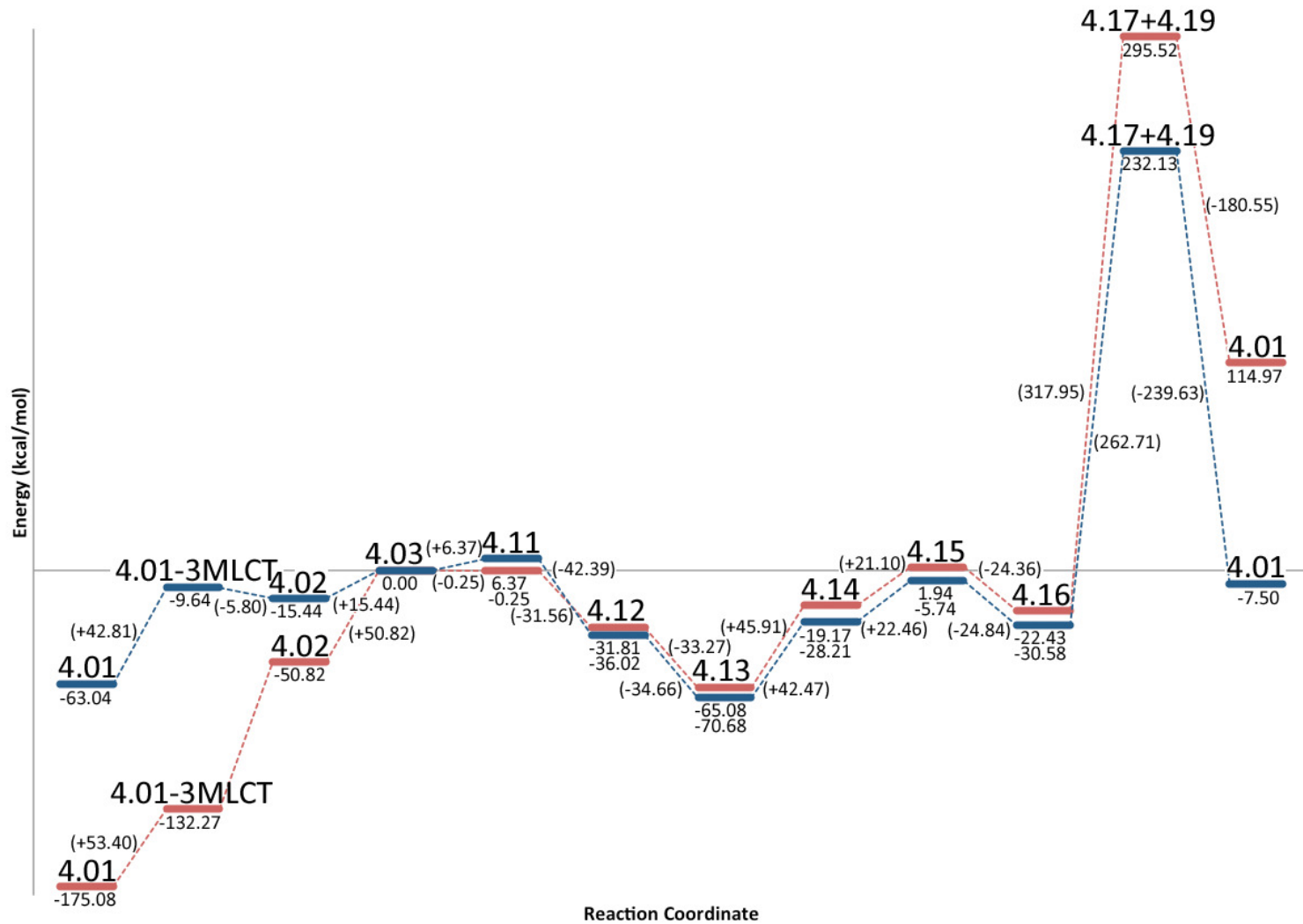


Figure D.7 Potential Energy Surface for the bicarbonate mechanistic pathway. Gas phase energies in red, DMF solvated energies in blue.

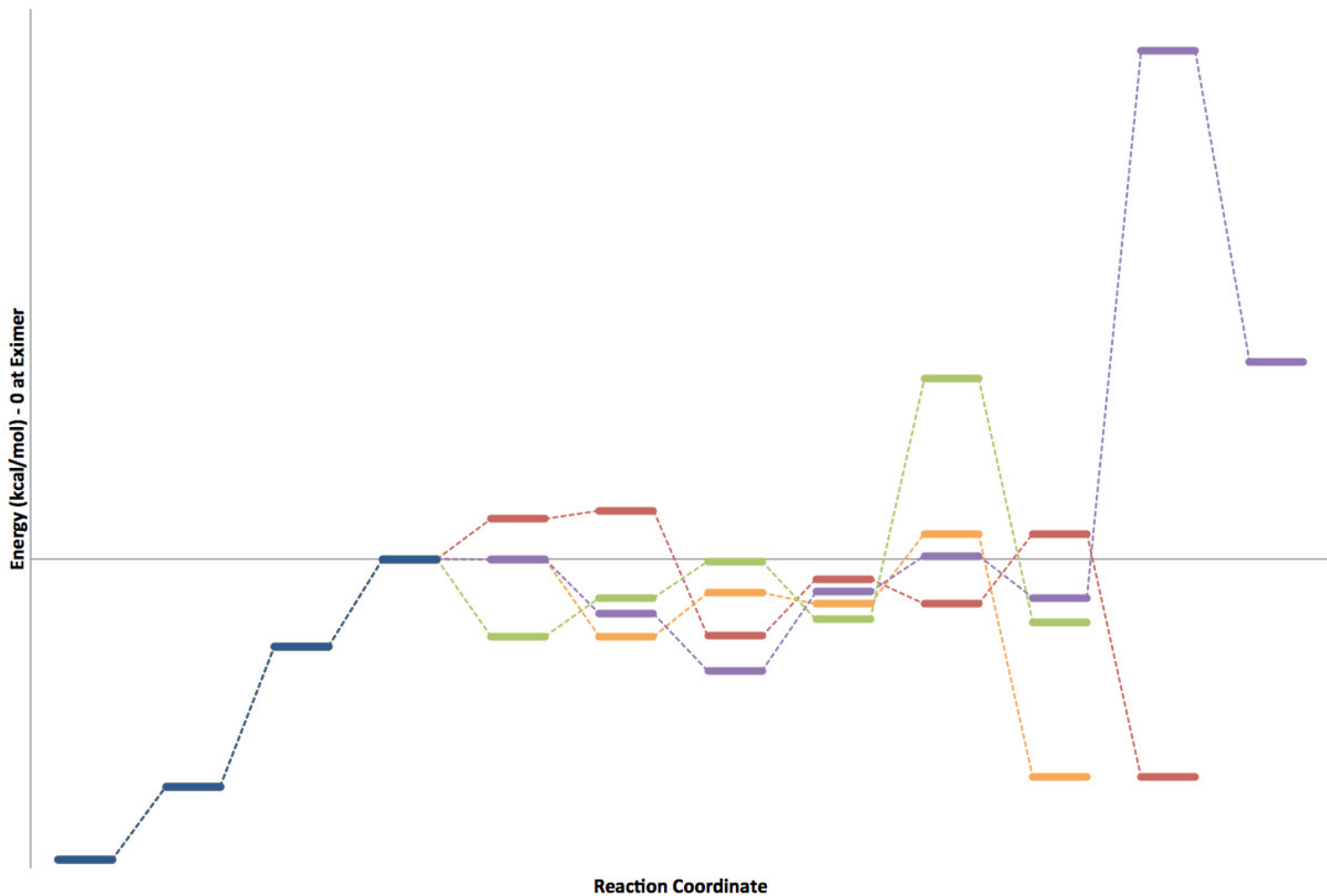


Figure D.8 An overview of the energies of the three mechanistic pathways of photochemical CO_2 reduction in gas phase. Excimer formation is shown in blue, the planar water-gas shift mechanism in red, the axial water-gas shift in orange, the bicarbonate in purple, and the formate in green.

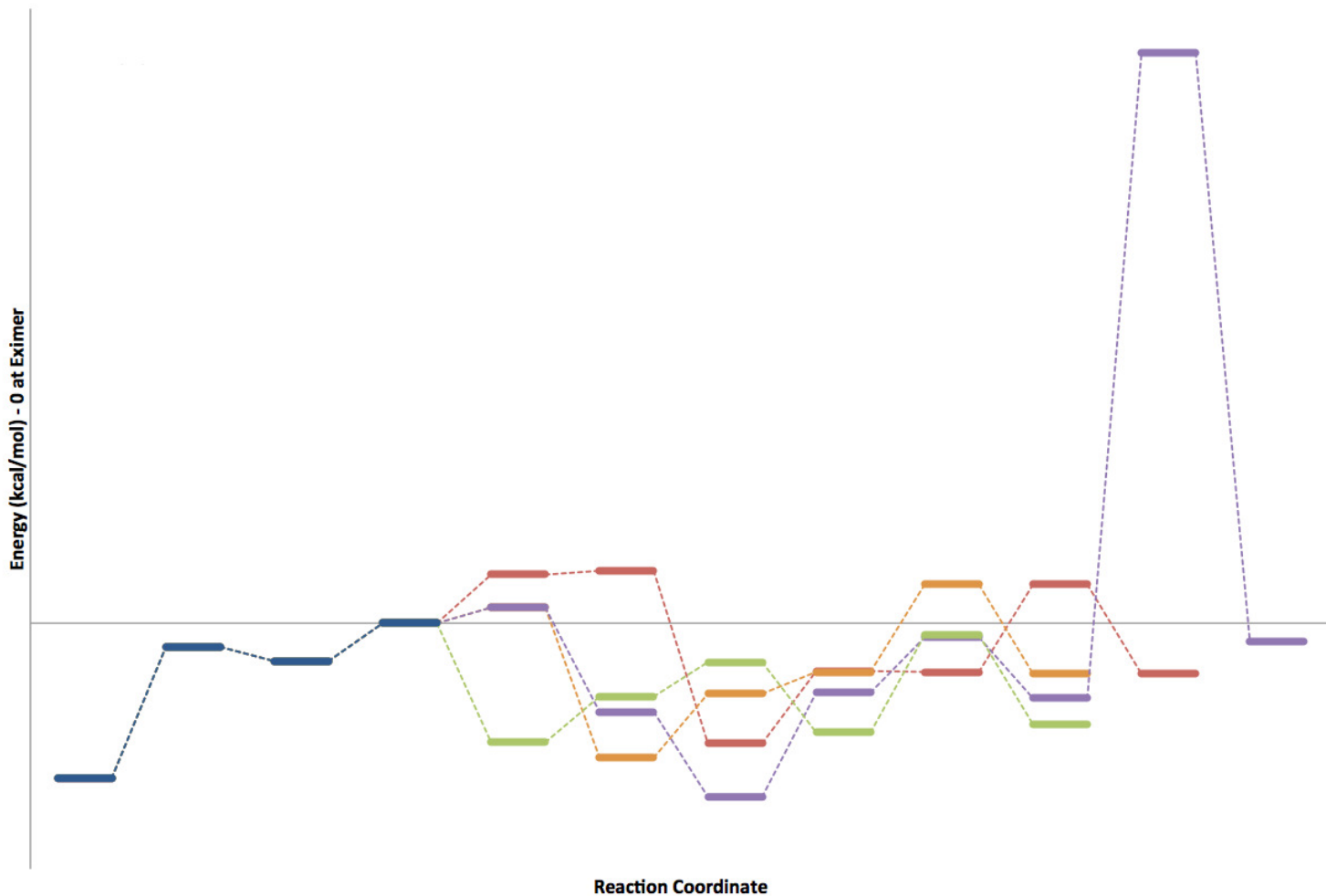


Figure D.9 An overview of the energies of the three mechanistic pathways of photochemical CO_2 reduction in DMF. Excimer formation is shown in blue, the planar water-gas shift mechanism in red, the axial water-gas shift in orange, the bicarbonate in purple, and the formate in green.

Appendix E

TurboControl and TurboGo Manual

TurboControl is a series of scripts to run TurboMole jobs from Gaussian style inputs. The following is the user manual included with distributions of TurboControl

E.1 Introduction

Gaussian software is well known for the user friendly GUI it contains (via GaussView). TurboMole, another computational suite, is known for its speed and optimizations, but has a significantly higher learning curve and is less beginner friendly. This software is an attempt to be able to use the user friendly input from Gaussian to smooth over the use of TurboMole.

E.2 System Requirements

There are two user-facing scripts available, both written to work with TurboMole 6.1-6.5 on clusters using Grid Engine queuing software. The only tests of operation are on a system with the following details:

- Rocks 6.1 (Emerald Boa)/CentOS 6.3
- Open Grid Scheduler/Grid Engine 2011.11p1
- Python 2.7.3

Other systems, including different operating systems, different versions of Grid Engine or python, or on other systems, are not supported.

Python dependencies include:

- pexpect 3.2²⁰⁸
- openbabel (optional)^{209,210}

Prior to running TurboGo or TurboControl, a valid installation of TurboMole must be available. On systems where computational modules must be loaded, TurboMole must have been loaded to the environment. Additionally, running the TurboMole environment configuration is recommended but not required prior to launching TurboGo or TurboControl:

```
$ source $TURBODIR/Config_turbo_env
```

E.3 Installation

Installation of TurboControl is very simple. Just extract the .tar.gz file available from the code repository at <https://github.com/pbulsink/turbocontrol/releases/latest>. Alternately, the source may be downloaded from <http://github.com/pbulsink/turbocontrol> and used without installation.

E.4 TurboGo

TurboGo is a script fun on an input file. It generates the inputs required for TurboMole jobs, and submits the job to the GridEngine queue before quitting. TurboGo is run with the following syntax:

```
$ turbogo [-h] [-v] [-q] file
```

positional arguments:

file	Read input from gaussian-type input FILE.
------	---

More info on the input files is available below.

optional arguments:

- **-h, --help** Show this help message and exit
- **-v, --verbose** Run more verbose (show debugging info)
- **-q, --quiet** Run less verbose (show only warnings)

TurboGo saves a log file (turbogo.log) in the directory in which it is run. A second log file (define.log) will remain if the setup crashes or is terminated at some points, or if the script is run verbose.

TurboGo writes the final coordinates to final_geometry.xyz. If openbabel is installed, it will also write finalgeom.mol. The entire optimization is written to optimization.xyz for viewing with a molecular viewer, such as vmd.

E.5 TurboControl

TurboControl is a management script called from a parent directory containing sub directories of input files. Each input file must be in its own directory. The input file format

must be the same as the input format for TurboGo (listed above), with the extension ‘.in’, ‘.inp’, ‘.input’, ‘.com’, or ‘.gjf’. TurboControl reads the inputs and submits the jobs to the computational cluster queue. It then monitors running jobs to determine when the script has finished. If the job is an Opt-Freq, it prepares the frequency analysis and resubmits to the queue. TurboControl analyses completed Opt-Freq jobs for true optimization, and attempts to re-run jobs with modified geometries when Transition States are found. TurboControl will not get stuck on the same transition state, but will return a ‘stuck’ job. TurboControl is run with the following syntax:

```
$ turbocontrol [-h] [-v/-q] [-s]
```

Optional arguments:

- **-h, --help** Show this help message and exit
- **-v, --verbose** Run more verbose (show debugging info)
- **-q, --quiet** Run less verbose (show only warnings)
- **-s, --solvent** List available solvents for COSMO and quit

TurboControl outputs information every 3 hours on the status of the jobs. It writes a log file (`turbocontrol.log`) and may or may not leave other log files in each directory (depending on verbosity level). Ends when the last job finishes or crashes. Requires 1 node or can be run on the headnode (minimal resource consumption especially after initial job preparation and submission.)

TurboControl assists with analysis by outputting a `stats.txt` file as jobs complete. This file contains file details, optimization and frequency timing details, energy, and the first frequency. Additional information can be requested by including the `freeh` keyword (see below).

E.6 Input File Format

The input file format is similar to that well known by Gaussian users. A series of keywords, one per line and indicated by a ‘%’, is followed by the ‘route card’ (specific job information). Charge and spin is indicated, then the molecule is shown in Cartesian format. This is followed by optional modifications to the TurboMole Control file. Note the location of blank lines in the example (Section 5.7).

E.6.1 Keywords

Keywords are as follows:

- **%nproc** - number of processors to use for the calculation job.
 - Synonym: **%processors**
- **%arch** - parallelization architecture to use for the job.
 - Synonyms: **%architecture**, **%para_arch**
- **%maxcycles** - number of optimization iterations before failing.
- **%autocontrolmod** - DEFAULT - modify the **control** file to include optimizations to speed up the job.
- **%nocontrolmod** - do not modify **control** file as above.
- **%rt** - specify max expected runtime (for any part of job)in hours. Allows backfilling in GridEngine queue to speed up job submission. For example, for a 1 hour opt and 4 hour freq, submit at least a **rt** of 4

- **%cosmo** - use TurboMole's COSMO solvation model with the specified solvent or **None** to use the idealized solvent (epsilon = infinity). List of available solvents can be shown by running `turbocontrol -s`

Gaussian args, including **%nosave**, **%rwf=[file]**, **%chk=[file]**, and **%mem=[memory]** are silently ignored.

E.6.2 Route Card Options

Route cards take the form of the following:

```
# [jobtype(s)] [joboption(s)]
```

Job types available:

- **opt** - Perform a geometry optimization
- **freq** - Perform a frequency analysis. Specify method via `numforce` or `aoforce`.
default = `numforce`
- **sp** - Perform a single point energy calculation.
 - Cannot be combined with Opt or Freq
- **ts** - Perform a transition state search to find 1 imaginary vibration.
 - Cannot be combined with Opt or Freq
- **prep** - Prepare the job but do not submit to queue.
 - Cannot be combined with Opt or Freq

Job options available:

- **ri** - Use TurboMole's ri approximation

- **marij** - Use TurboMole's marij approximation
 - Requires **ri**
- **disp** - Use TurboMole's implementation of Grimme's dispersion, version 3
- **aoforce** - Use aoforce for frequency jobs
- **numforce** - Use numforce for frequency jobs
- **freeh** - Use TurboMole's **freeh** thermodynamics data script to extract thermodynamic information after frequency analysis

E.6.3 Title

Following the Route cards, a blank line is added, then a line containing the title of the calculation. This can include any characters, spaces, etc., remaining on only one line. This is followed by a blank line.

E.6.4 Charge and Spin

Charge and spin are listed as two numbers separated by a space: charge spin (eg:0 1)

E.6.5 Geometry

Geometry in xyz coordinate format: Element xcoord ycoord zcoord. Z-matrix geometry is not supported by TurboControl or TurboGo.

E.6.6 Additional control File Modifications

Additional lines to be added or removed from control. Lines automatically added are, as required,:

```
$ricore 0
$paroptions ga_memperproc 9000000000000000 900000000000
$parallel_parameters maxtask=10000
$ricore_slave 1
$maxcor 2048
```

Additional lines may be added, or lines removed, by placing them after the geometry with a \$ (for addition) or -\$ (for removal).

E.6.7 Example Input File

An example input file for benzene in dmf:

```
%nproc=4
%arch=GA
%maxcycles=250
%rt=6
%cosmo=dmf
# opt freq b3-lyp/def2-TZVP ri marij numforce

Benzene Optimization & Frequency

O 1
C 0.000 1.396 0.000
C 1.209 0.698 0.000
C 1.209 -0.698 0.000
C 0.000 -1.396 0.000
C -1.209 -0.698 0.000
C -1.209 0.698 0.000
H 0.000 2.479 0.000
H 2.147 1.240 0.000
H 2.147 -1.240 0.000
H 0.000 -2.479 0.000
H -2.147 -1.240 0.000
H -2.147 1.240 0.000

$disp
-$paroptions
```

E.7 Code Details

Coverage percentages of code unit tests are listed in Table E.1. Results are low for def_op, screwer_op, cosmo_op, freeh_op, turbocontrol, and turbogo because they contain many

lines of interacting with GridEngine or TurboMole. Testing is performed via monitoring the status of the scripts as they run in real conditions.

The code style is graded by PyLint and results are shown in Table E.2. PyLint describes coding style, adherence to guidelines, and readability. It does not describe code efficiency or usefulness.

Table E.1 Test Coverage of scripts in TurboControl.

Name	Statements	Missing	Excluded	Coverage
cosmo_op	106	70	1	34%
cosmo_op_test	17	1	0	94%
def_op	302	226	1	25%
def_op_test	20	1	0	95%
freeh_op	162	55	1	66%
freeh_op_test	27	1	0	96%
screwer_op	71	25	1	65%
screwer_op_test	11	1	0	91%
test_all	18	0	0	100%
turbocontrol	537	319	0	41%
turbocontrol_test	245	24	0	90%
turbogo	343	132	0	62%
turbogo_helpers	383	52	0	86%
turbogo_helpers_test	274	2	0	99%
turbogo_test	98	1	0	99%
TOTAL	2614	910	4	65%

Table E.2 PyLint Scores for Turbocontrol Code.

File	Score /10
test_all.py	2.22
turbogo.py	8.80
turbogo_test.py	6.97
turbocontrol.py	8.55
turbocontrol_test.py	7.18
turbogo_helpers.py	8.81
turbogo_helpers_test.py	7.45
def_op.py	8.18
def_op_test.py	5.71
screwer_op.py	7.36
screwer_op_test.py	6.67
freeh_op.py	8.71
freeh_op_test.py	6.79
cosmo_op.py	8.22
cosmo_op_test.py	6.67

E.8 Citing TurboControl

TurboControl, Turbogo, or any other parts of this code may be cited as:

Bulsink, Philip. TurboControl, v. 1.1.0. <http://github.org/pbulsink/turbocontrol> (accessed June 2014)

Change the version number to match the version that you used, and change the accessed date to when you installed or downloaded TurboControl.

E.9 License

All third party software is a registered trademark of their respective creators. Use of third party software via this software is limited by the conditions as laid out by the respective companies. License to use this software in no way acts as a license to use any other separate referenced software.

The MIT License (MIT)

Copyright © 2014 Philip Bulsink

Permission is hereby granted, free of charge, to any person obtaining a copy of this software and associated documentation files (the “Software”), to deal in the Software without restriction, including without limitation the rights to use, copy, modify, merge, publish, distribute, sublicense, and/or sell copies of the Software, and to permit persons to whom the Software is furnished to do so, subject to the following conditions:

The above copyright notice and this permission notice shall be included in all copies or substantial portions of the Software.

THE SOFTWARE IS PROVIDED “AS IS”, WITHOUT WARRANTY OF ANY KIND, EXPRESS OR IMPLIED, INCLUDING BUT NOT LIMITED TO THE WARRANTIES OF MERCHANTABILITY, FITNESS FOR A PARTICULAR PURPOSE AND NONINFRINGEMENT. IN NO EVENT SHALL THE AUTHORS OR COPYRIGHT HOLDERS BE LIABLE FOR ANY CLAIM, DAMAGES OR OTHER LIABILITY, WHETHER IN AN ACTION OF CONTRACT, TORT OR OTHERWISE, ARISING FROM, OUT OF OR IN CONNECTION WITH THE SOFTWARE OR THE USE OR OTHER DEALINGS IN THE SOFTWARE.

Glossary of Terms

CCDC Cambridge Crystallography Data Centre

COSMO Conductor-like Screening Model

DFT Density Functional Theory

DMF N,N-dimethylformamide

DMSO Dimethylsulfoxide

FTIR Fourier Transform Infrared

GC Gas Chromatography

GUI graphical user interface

HOMO Highest Occupied Molecular Orbital

IRC Intrinsic Reaction Coordinate

LUMO Lowest Unoccupied Molecular Orbital

MLCT Metal-Ligand Charge Transfer

MO Molecular Orbital

NMR Nuclear Magnetic Resonance

PCM Polarizable Continuum Model

RWGSR Reverse Water-Gas Shift Reaction

TCD Thermal Conductivity Detector

TD-DFT Time Dependant Density Functional Theory

TEA Triethylamine

TEOA Triethanolamine

TGA Thermogravimetric Analysis

Bibliography

1. Zeise, W. C. *J. Physik und Chemie (Schweigger)* **1831**, *62*, 393–441.
2. Hunt, L. B. *Platinum Metals Review* **1984**, *28*, 76–83.
3. Griess, J. P.; Martius, C. A. *Compt Rendus*. **1861**, *53*, 922–925.
4. Birnbaum, K. *Ann. Chem. (Liebig)* **1868**, *145*, 67–77.
5. Small, B. L.; Brookhart, M. *J. Am. Chem. Soc.* **1998**, *120*, 7143–7144.
6. Small, B. L.; Brookhart, M.; Bennett, A. M. A. *J. Am. Chem. Soc.* **1998**, *120*, 4049–4050.
7. J. P. Britovsek, G.; C. Gibson, V.; J. McTavish, S.; A. Solan, G.; J. P. White, A.; J. Williams, D.; J. P. Britovsek, G.; S. Kimberley, B.; J. Maddox, P. *Chem. Commun.* **1998**, 849–850.
8. Britovsek, G. J. P.; Bruce, M.; Gibson, V. C.; Kimberley, B. S.; Maddox, P. J.; Mastroianni, S.; McTavish, S. J.; Redshaw, C.; Solan, G. A.; Strömberg, S.; White, A. J. P.; Williams, D. J. *J. Am. Chem. Soc.* **1999**, *121*, 8728–8740.
9. Gibson, V. C.; Redshaw, C.; Solan, G. A. *Chem. Rev.* **2007**, *107*, PMID: 17488059, 1745–1776.
10. Boudier, A.; Breuil, P.-A. R.; Magna, L.; Olivier-Bourbigou, H.; Braunstein, P. *Chem. Commun.* **2014**, *50*, 1398–1407.
11. Dudle, B.; Rajesh, K.; Blacque, O.; Berke, H. *J. Am. Chem. Soc.* **2011**, *133*, 8168–8178.
12. Jain, K. R.; Herrmann, W. A.; Kühn, F. E. *Coord. Chem. Rev.* **2008**, *252*, Chiral Catalysis, 556–568.
13. Kuninobu, Y.; Takai, K. *Chem. Rev.* **2011**, *111*, 1938–1953.
14. Kusama, H; Narasaka, K *Bull. Chem. Soc. Jpn.* **1995**, *68*, 2379–2383.
15. Nishiyama, Y.; Kakushou, F.; Sonoda, N. *Bull. Chem. Soc. Jpn.* **2000**, *73*, 2779–2782.
16. Kuninobu, Y.; Matsuki, T.; Takai, K. *J. Am. Chem. Soc.* **2009**, *131*, PMID: 19621953, 9914–9915.

17. Bolm, C.; Kesselgruber, M.; Hermanns, N.; Hildebrand, J. P.; Raabe, G. *Angew. Chem., Int. Ed.* **2001**, *40*, 1488–1490.
18. Zhao, W.-G.; Hua, R. *Tetrahedron* **2007**, *63*, 11803–11808.
19. Kawata, A.; Kuninobu, Y.; Takai, K. *Chem. Lett.* **2009**, *38*, 836–837.
20. Hori, H.; Koike, K.; Takeuchi, K.; Ishitani, O. *Chem. Lett.* **2000**, *29*, 376–377.
21. Hua, R.; Tian, X. *J. Org. Chem.* **2004**, *69*, PMID: 15307759, 5782–5784.
22. Adams, R. D.; Falloon, S. B. *J. Am. Chem. Soc.* **1994**, *116*, 10540–10547.
23. Adams, R. D.; Huang, M.; Huang, W.; Queisser, J. A. *J. Am. Chem. Soc.* **1996**, *118*, 9442–9443.
24. Zhao, W.-G.; Hua, R. *Euro. J. Org. Chem.* **2006**, *2006*, 5495–5498.
25. Müller, T. E.; Grosche, M.; Herdtweck, E.; Pleier, A.-K.; Walter, E.; Yan, Y.-K. *Organometallics* **2000**, *19*, 170–183.
26. Bartholoma, M.; Valliant, J.; Maresca, K. P.; Babich, J.; Zubieta, J. *Chem. Commun.* **2009**, 493–512.
27. Schibli, R.; Schubiger, A. *Euro. J. Nuc. Med. Mol. Imaging* **2002**, *29*, 1529–1542.
28. Coogan, M.; Fernández-Moreira, V.; Kariuki, B.; Pope, S.; Thorp-Greenwood, F. *Angew. Chem., Int. Ed.* **2009**, *48*, 4965–4968.
29. Giordano, P. J.; Wrighton, M. S. *J. Am. Chem. Soc.* **1979**, *101*, 2888–2897.
30. Fredericks, S. M.; Luong, J. C.; Wrighton, M. S. *J. Am. Chem. Soc.* **1979**, *101*, 7415–7417.
31. Sacksteder, L.; Zipp, A. P.; Brown, E. A.; Streich, J.; Demas, J. N.; DeGraff, B. A. *Inorg. Chem.* **1990**, *29*, 4335–4340.
32. Caspar, J. V.; Meyer, T. J. *J. Phys. Chem.* **1983**, *87*, 952–957.
33. Yam, V. W.-W. *Chem. Commun.* **2001**, 789–796.
34. Feliz, M.; Rodriguez-Nieto, F.; Ruiz, G.; Wolcan, E. *J. Photochem. Photobiol., A* **1998**, *117*, 185–192.
35. Ruiz, G.; Wolcan, E.; Félix, M. *J. Photochem. Photobiol., A* **1996**, *101*, 119–125.
36. Lin, R.; Fu, Y.; Brock, C. P.; Guarr, T. F. *Inorg. Chem.* **1992**, *31*, 4346–4353.
37. Hino, J. K.; Della Ciana, L.; Dressick, W. J.; Sullivan, B. P. *Inorg. Chem.* **1992**, *31*, 1072–1080.
38. Walters, K. A.; Kim, Y.-J.; Hupp, J. T. *Inorg. Chem.* **2002**, *41*, 2909–2919.
39. Striplin, D.; Crosby, G. *Coord. Chem. Rev.* **2001**, *211*, 163–175.
40. Martin, T. A.; Ellul, C. E.; Mahon, M. F.; Warren, M. E.; Allan, D.; Whittlesey, M. K. *Organometallics* **2011**, *30*, 2200–2211.

41. Abel, E. W.; Wilkinson, G. *J. Chem. Soc.* **1959**, 1501–1505.
42. Kirkham, W. J.; Osborne, A. G.; Nyholm, R. S.; Stiddard, M. H. B. *J. Chem. Soc.* **1965**, 550–553.
43. Zingales, F.; Sartorelli, U.; Trovati, A. *Inorg. Chem.* **1967**, *6*, 1246–1248.
44. Gamelin, D. R.; George, M. W.; Glyn, P.; Grevels, F.-W.; Johnson, F. P. A.; Klotzbuecher, W.; Morrison, S. L.; Russell, G.; Schaffner, K.; Turner, J. J. *Inorg. Chem.* **1994**, *33*, 3246–3250.
45. Martí, A. A.; Mezei, G.; Maldonado, L.; Paralitici, G.; Raptis, R. G.; Colón, J. L. *Euro. J. Inorg. Chem.* **2005**, *2005*, 118–124.
46. Morse, D. L.; Wrighton, M. S. *J. Am. Chem. Soc.* **1976**, *98*, 3931–3934.
47. Ge, Q.; Corkery, T. C.; Humphrey, M. G.; Samoc, M.; Hor, T. S. A. *Dalton Trans.* **2009**, 6192–6200.
48. Giordano, P. J.; Fredericks, S. M.; Wrighton, M. S.; Morse, D. L. *J. Am. Chem. Soc.* **1978**, *100*, 2257–2259.
49. Granifo, J.; Bird, S. J.; Orrell, K. G.; Osborne, A. G.; Šik, V. *Inorg. Chem. Acta* **1999**, *295*, 56–63.
50. Orrell, K. G.; Osborne, A. G.; Šik, V.; da Silva, M. W.; Hursthouse, M. B.; Hibbs, D. E.; Malik, K. A.; Vassilev, N. G. *J. Organomet. Chem.* **1997**, *538*, 171–183.
51. Abel, E. W.; Dimitrov, V. S.; Long, N. J.; Orrell, K. G.; Osborne, A. G.; Pain, H. M.; Sik, V.; Hursthouse, M. B.; Mazid, M. A. *J. Chem. Soc., Dalton Trans.* **1993**, 597–603.
52. Potgieter, K.; Mayer, P.; Gerber, T.; Yumata, N.; Hosten, E.; Boysen, I.; Betz, R.; Ismail, M.; van Brecht, B. *Polyhedron* **2013**, *49*, 67–73.
53. Gong, X.; Ng, P. K.; Chan, W. K. *Adv. Mater.* **1998**, *10*, 1337–1340.
54. Yu, T.; Tsang, D. P.-K.; Au, V. K.-M.; Lam, W. H.; Chan, M.-Y.; Yam, V. W.-W. *Chem.-Eur. J.* **2013**, *19*, 13418–13427.
55. Lo, K. K.-W.; Louie, M.-W.; Zhang, K. Y. *Coord. Chem. Rev.* **2010**, *254*, 18th International Symposium on the Photochemistry and Photophysics of Coordination Compounds Sapporo, 2009, 2603–2622.
56. Lin, T.-P.; Chen, C.-Y.; Wen, Y.-S.; Sun, S.-S. *Inorg. Chem.* **2007**, *46*, 9201–9212.
57. Slone, R. V.; Yoon, D. I.; Calhoun, R. M.; Hupp, J. T. *J. Am. Chem. Soc.* **1995**, *117*, 11813–11814.
58. D. Beer, P.; Timoshenko, V.; Maestri, M.; Passaniti, P.; Balzani, V. *Chem. Commun.* **1999**, 1755–1756.
59. Beer, P. D.; Hayes, E. J. *Coord. Chem. Rev.* **2003**, *240*, 35 Years of Synthetic Anion Receptor Chemistry 1968–2003, 167–189.

60. Amoroso, A. J.; Arthur, R. J.; Coogan, M. P.; Court, J. B.; Fernandez-Moreira, V.; Hayes, A. J.; Lloyd, D.; Millet, C.; Pope, S. J. A. *New J. Chem.* **2008**, *32*, 1097–1102.
61. Amoroso, A. J.; Coogan, M. P.; Dunne, J. E.; Fernandez-Moreira, V.; Hess, J. B.; Hayes, A. J.; Lloyd, D.; Millet, C.; Pope, S. J. A.; Williams, C. *Chem. Commun.* **2007**, 3066–3068.
62. Schutte, M.; Kemp, G.; Visser, H. G.; Roodt, A. *Inorg. Chem.* **2011**, *50*, 12486–12498.
63. Shestopalov, M. A.; Zubareva, K. E.; Khripko, O. P.; Khripko, Y. I.; Solovieva, A. O.; Kuratieva, N. V.; Mironov, Y. V.; Kitamura, N.; Fedorov, V. E.; Brylev, K. A. *Inorganic Chemistry* **0**, *0*, null.
64. Gimeno, M. C.; Fernandez-Moreira, V.; Marzo, I. *Chem. Sci.* **2014**, –.
65. Constable, E. C.; Thompson, A. M. W. C. *J. Chem. Soc., Dalton Trans.* **1992**, 3467–3475.
66. Hawecker, J.; Lehn, J.-M.; Ziessel, R. *J. Chem. Soc., Chem. Commun.* **1983**, 536–538.
67. Hawecker, J.; Lehn, J.-M.; Ziessel, R. *Helv. Chim. Acta* **1986**, *69*, 1990–2012.
68. Takeda, H.; Ishitani, O. *Coord. Chem. Rev.* **2010**, *254*, Inorganic Reaction Mechanisms A Tribute to Ralph Pearson on the occasion of his 90th birthday, 346 – 354.
69. Christensen, P.; Hamnett, A.; Muir, A. V. G.; Timney, J. A. *J. Chem. Soc., Dalton Trans.* **1992**, 1455–1463.
70. Sullivan, B. P.; Bolinger, C. M.; Conrad, D.; Vining, W. J.; Meyer, T. J. *J. Chem. Soc., Chem. Commun.* **1985**, 1414–1416.
71. Caulton, K. G. *Euro. J. Inorg. Chem.* **2012**, *2012*, 435–443.
72. Lyaskovskyy, V.; de Bruin, B. *ACS Catal.* **2012**, *2*, 270–279.
73. Jurca, T.; Chen, W.-C.; Michel, S.; Korobkov, I.; Ong, T.-G.; Richeson, D. S. *Chem.-Eur. J.* **2013**, *19*, 4278–4286.
74. Juris, A.; Campagna, S.; Bidd, I.; Lehn, J. M.; Ziessel, R. *Inorg. Chem.* **1988**, *27*, 4007–4011.
75. Black, D. R.; Hightower, S. E. *Inorg. Chem. Commun.* **2012**, *24*, 16 –19.
76. Song, C. *Catal. Today* **2006**, *115*, Proceedings of the 8th International Conference on Carbon Dioxide Utilization Dedicated to Professor Michele Aresta, 2 –32.
77. Matthews, H. D.; Gillett, N. P.; Stott, P. A.; Zickfeld, K. *Nature* **June 2009**, *459*, 829–832.

78. Meinshausen, M.; Meinshausen, N.; Hare, W.; Raper, S. C. B.; Frieler, K.; Knutti, R.; Frame, D. J.; Allen, M. R. *Nature* **2009**, *458*, 1158–1162.
79. Neuhoff, K. *Oxford Rev. Econ. Policy* **2005**, *21*, 88–110.
80. Pera-Titus, M. *Chem. Rev.* **2014**, *114*, 1413–1492.
81. Kadantsev, E. S.; Boyd, P. G.; Daff, T. D.; Woo, T. K. *J. Phys. Chem. Lett.* **2013**, *4*, 3056–3061.
82. Iremonger, S. S.; Liang, J.; Vaidhyanathan, R.; Martens, I.; Shimizu, G. K. H.; Daff Thomas, D.; Aghaji, M. Z.; Yeganegi, S.; Woo, T. K. *J. Am. Chem. Soc.* **2011**, *133*, 20048–20051.
83. Leitner, W. *Coord. Chem. Rev.* **1996**, *153*, 257–284.
84. Olah, G. A.; Goepert, A.; Prakash, G. K. S., *Beyond Oil and Gas: The Methanol Economy*, 2nd; Wiley: 2009.
85. Kang, P.; Cheng, C.; Chen, Z.; Schauer, C. K.; Meyer, T. J.; Brookhart, M. *J. Am. Chem. Soc.* **2012**, *134*, 5500–5503.
86. Schwarz, H. A.; Dodson, R. W. *J. Phys. Chem.* **1989**, *93*, 409–414.
87. Morris, A. J.; Meyer, G. J.; Fujita, E. *Acc. Chem. Res.* **2009**, *42*, PMID: 19928829, 1983–1994.
88. Arakawa, H. et al. *Chem. Rev.* **2001**, *101*, PMID: 11709862, 953–996.
89. Li, W. In *Advances in CO_j Conversion and Utilization*; ACS Symposium Series, Vol. 1056; American Chemical Society: 2010; Chapter 5, pp 55–76.
90. Inoue, T.; Fujishima, A.; Konishi, S.; Honda, K. *Nature* **1979**, *277*, 637–638.
91. Lim, H.-K.; Shin, H.; Goddard, W. A.; Hwang, Y. J.; Min, B. K.; Kim, H. *J. Am. Chem. Soc.* **2014**, *136*, 11355–11361.
92. Fisher, B. J.; Eisenberg, R. *J. Am. Chem. Soc.* **1980**, *102*, 7361–7363.
93. Tinnemans, A. H. A.; Koster, T. P. M.; Thewissen, D. H. M. W.; Mackor, A. *Recueil des Travaux Chimiques des Pays-Bas* **1984**, *103*, 288–295.
94. Beley, M.; Collin, J. P.; Ruppert, R.; Sauvage, J. P. *J. Am. Chem. Soc.* **1986**, *108*, 7461–7467.
95. Simon-Manso, E.; Kubiak, C. P. *Organometallics* **2004**, *24*, 96–102.
96. Fujita, E.; Haff, J.; Sanzenbacher, R.; Elias, H. *Inorg. Chem.* **1994**, *33*, 4627–4628.
97. Fujita, E.; Creutz, C.; Sutin, N.; Brunschwig, B. S. *Inorg. Chem.* **1993**, *32*, 2657–2662.
98. Kimura, E.; Wada, S.; Shionoya, M.; Okazaki, Y. *Inorg. Chem.* **1994**, *33*, 770–778.
99. Dhanasekaran, T.; Grodkowski, J.; Neta, P.; Hambright, P.; Fujita, E. *J. Phys. Chem. A* **1999**, *103*, 7742–7748.

100. Lacy, D. C.; McCrory, C. C. L.; Peters, J. C. *Inorg. Chem.* **2014**, *53*, 4980–4988.
101. Bourrez, M.; Molton, F.; Chardon-Noblat, S.; Deronzier, A. *Angew. Chem., Int. Ed.* **2011**, *50*, 9903–9906.
102. Sampson, M. D.; Nguyen, A. D.; Grice, K. A.; Moore, C. E.; Rheingold, A. L.; Kubiak, C. P. *J. Am. Chem. Soc.* **2014**, *136*, 5460–5471.
103. Zeng, Q.; Tory, J.; Hartl, F. *Organometallics* **0**, *0*, null.
104. Schneider, J.; Vuong, K. Q.; Calladine, J. A.; Sun, X.-Z.; Whitwood, A. C.; George, M. W.; Perutz, R. N. *Inorg. Chem.* **2011**, *50*, 11877–11889.
105. Ishida, H.; Tanaka, K.; Tanaka, T. *Organometallics* **1987**, *6*, 181–186.
106. Maidan, R.; Willner, I. *J. Am. Chem. Soc.* **1986**, *108*, 8100–8101.
107. Ishida, H.; Terada, T.; Tanaka, K.; Tanaka, T. *Inorg. Chem.* **1990**, *29*, 905–911.
108. Kitamura, N.; Tazuke, S. *Chem. Lett.* **1983**, *12*, 1109–1112.
109. Tanaka, K.; Ooyama, D. *Coord. Chem. Rev.* **2002**, *226*, 211–218.
110. Doherty, M. D.; Grills, D. C.; Fujita, E. *Inorg. Chem.* **2009**, *48*, 1796–1798.
111. Doherty, M. D.; Grills, D. C.; Muckerman, J. T.; Polyansky, D. E.; Fujita, E. *Coord. Chem. Rev.* **2010**, *254*, 18th International Symposium on the Photochemistry and Photophysics of Coordination Compounds Sapporo, 2009, 2472–2482.
112. Tamaki, Y.; Koike, K.; Morimoto, T.; Yamazaki, Y.; Ishitani, O. *Inorg. Chem.* **2013**, *52*, 11902–11909.
113. Sato, S.; Morikawa, T.; Kajino, T.; Ishitani, O. *Angew. Chem., Int. Ed.* **2013**, *52*, 988–992.
114. Reithmeier, R. O.; Meister, S.; Rieger, B.; Siebel, A.; Tschurl, M.; Heiz, U.; Herdtweck, E. *Dalton Trans.* **2014**, –.
115. Hori, H.; Johnson, F. P.; Koike, K.; Ishitani, O.; Ibusuki, T. *J. Photochem. Photobiol., A* **1996**, *96*, 171–174.
116. Takeda, H.; Koike, K.; Inoue, H.; Ishitani, O. *J. Am. Chem. Soc.* **2008**, *130*, 2023–2031.
117. Grills, D. C.; Fujita, E. *J. Phys. Chem. Lett.* **2010**, *1*, 2709–2718.
118. Windle, C. D.; Perutz, R. N. *Coord. Chem. Rev.* **2012**, *256*, Solar Fuels- by invitation only, 2562–2570.
119. Shavaleev, N. M.; Barbieri, A.; Bell, Z. R.; Ward, M. D.; Barigelli, F. *New J. Chem.* **2004**, *28*, 398–405.
120. Kutal, C.; Weber, M. A.; Ferraudi, G.; Geiger, D. *Organometallics* **1985**, *4*, 2161–2166.

121. Larsen, C. B.; van der Salm, H.; Clark, C. A.; Elliott, A. B. S.; Fraser, M. G.; Horvath, R.; Lucas, N. T.; Sun, X.-Z.; George, M. W.; Gordon, K. C. *Inorg. Chem.* **2014**, *53*, 1339–1354.
122. Russell, S. K.; Darmon, J. M.; Lobkovsky, E.; Chirik, P. J. *Inorg. Chem.* **2010**, *49*, PMID: 20143847, 2782–2792.
123. Tondreau, A. M.; Atienza, C. C. H.; Weller, K. J.; Nye, S. A.; Lewis, K. M.; Delis, J. G. P.; Chirik, P. J. *Science* **2012**, *335*, 567–570.
124. SciFinder. Chemical Abstracts Services, a division of the American Chemical Society.
125. Buckingham, D.; Dwyer, F.; Goodwin, H.; Sargeson, A. *Aust. J. Chem.* **1964**, *17*, 315–324.
126. Jurca, T. Charting New Territory in Bis(imino)pyridine Coordination Chemistry., PhD Thesis, University of Ottawa, 2012.
127. Morimoto, T.; Nakajima, T.; Sawa, S.; Nakanishi, R.; Imori, D.; Ishitani, O. *J. Am. Chem. Soc.* **2013**, *135*, 16825–16828.
128. Anderson, P. A.; Keene, F. R.; Horn, E.; Tiekkink, E. R. T. *Appl. Organomet. Chem.* **1990**, *4*, 523–533.
129. Civitello, E. R.; Dragovich, P. S.; Karpishin, T. B.; Novick, S. G.; Bierach, G.; O'Connell, J. F.; Westmoreland, T. D. *Inorg. Chem.* **1993**, *32*, 237–241.
130. Kurz, P.; Probst, B.; Spangler, B.; Alberto, R. *Euro. J. Inorg. Chem.* **2006**, *2006*, 2966–2974.
131. Becke, A. D. *J. Chem. Phys.* **1993**, *98*, 5648–5652.
132. Lee, C.; Yang, W.; Parr, R. G. *Phys. Rev. B* **1988**, *37*, 785–789.
133. Frisch, M. J. et al. Gaussian 09 Revision D.01., Gaussian Inc. Wallingford CT 2009.
134. Hay, P. J.; Wadt, W. R. *J. Chem. Phys.* **1985**, *82*, 299–310.
135. Schäfer, A.; Huber, C.; Ahlrichs, R. *J. Chem. Phys.* **1994**, *100*, 5829–5835.
136. Zhang, I. Y.; Wu, J.; Xu, X. *Chem. Commun.* **2010**, *46*, 3057–3070.
137. Zhao, Y.; Truhlar, D. G. *Accounts of Chemical Research* **2008**, *41*, 157–167.
138. Tomasi, J.; Mennucci, B.; Cammi, R. *Chem. Rev.* **2005**, *105*, 2999–3094.
139. Scalmani, G.; Frisch, M. J.; Mennucci, B.; Tomasi, J.; Cammi, R.; Barone, V. *J. Chem. Phys.* **2006**, *124* 094107, –.
140. Compain, J.-D.; Bourrez, M.; Haukka, M.; Deronzier, A.; Chardon-Noblat, S. *Chem. Commun.* **2014**, *50*, 2539–2542.
141. Allen, F. H. *Acta Crystallogr. Sect. B* **2002**, *58*, 380–388.

142. Andersson, M. P.; Uvdal, P. *The Journal of Physical Chemistry A* **2005**, *109*, PMID: 16833612, 2937–2941.
143. Portenkirchner, E.; Kianfar, E.; Sariciftci, N. S.; Knör, G. *ChemSusChem* **2014**, *7*, 1347–1351.
144. Rossenaar, B. D.; Hartl, F.; Stufkens, D. J. *Inorg. Chem.* **1996**, *35*, 6194–6203.
145. Hayashi, Y.; Kita, S.; Brunschwig, B. S.; Fujita, E. *J. Am. Chem. Soc.* **2003**, *125*, PMID: 14505419, 11976–11987.
146. Agarwal, J.; Johnson, R. P.; Li, G. *J. Phys. Chem. A* **2011**, *115*, 2877–2881.
147. Agarwal, J.; Sanders, B. C.; Fujita, E.; Schaefer III, H. F.; Harrop, T. C.; Muckerman, J. T. *Chem. Commun.* **2012**, *48*, 6797–6799.
148. Agarwal, J.; Fujita, E.; Schaefer, H. F.; Muckerman, J. T. *J. Am. Chem. Soc.* **2012**, *134*, 5180–5186.
149. Keith, J. A.; Grice, K. A.; Kubiak, C. P.; Carter, E. A. *J. Am. Chem. Soc.* **2013**, *135*, 15823–15829.
150. Grills, D. C.; Matsubara, Y.; Kuwahara, Y.; Golisz, S. R.; Kurtz, D. A.; Mello, B. A. *J. Phys. Chem. Lett.* **2014**, *5*, 2033–2038.
151. Martin, R. B.; Lissfelt, J. A. *J. Am. Chem. Soc.* **1956**, *78*, 938–940.
152. Zink, J. I. *Coord. Chem. Rev.* **2001**, *211*, 69–96.
153. Johnson, F. P. A.; George, M. W.; Hartl, F.; Turner, J. J. *Organometallics* **1996**, *15*, 3374–3387.
154. Koike, K.; Okoshi, N.; Hori, H.; Takeuchi, K.; Ishitani, O.; Tsubaki, H.; Clark, I. P.; George, M. W.; Johnson, F. P. A.; Turner, J. J. *J. Am. Chem. Soc.* **2002**, *124*, 11448–11455.
155. Gibson, D. H.; Yin, X.; He, H.; Mashuta, M. S. *Organometallics* **2003**, *22*, 337–346.
156. Smieja, J. M.; Benson, E. E.; Kumar, B.; Grice, K. A.; Seu, C. S.; Miller, A. J. M.; Mayer, J. M.; Kubiak, C. P. *Proc. Natl. Acad. Sci. U. S. A.* **2012**, *109*, 15646–15650.
157. Machan, C. W.; Sampson, M. D.; Chabolla, S. A.; Dang, T.; Kubiak, C. P. *Organometallics* **2014**, Accepted Article, DOI: 10.1021/om500044a.
158. Kou, Y.; Nabetani, Y.; Masui, D.; Shimada, T.; Takagi, S.; Tachibana, H.; Inoue, H. *J. Am. Chem. Soc.* **2014**, *136*, 6021–6030.
159. Hawecker, J.; Lehn, J.-M.; Ziessel, R. *J. Chem. Soc., Chem. Commun.* **1984**, 328–330.
160. Roy, S. C.; Varghese, O. K.; Paulose, M.; Grimes, C. A. *ACS Nano* **2010**, *4*, PMID: 20141175, 1259–1278.

161. Asatani, T.; Nakagawa, Y.; Funada, Y.; Sawa, S.; Takeda, H.; Morimoto, T.; Koike, K.; Ishitani, O. *Inorg. Chem.* **2014**, *53*, 7170–7180.
162. Kalyanasundaram, K.; Kiwi, J.; Grätzel, M. *Helv. Chim. Acta* **1978**, *61*, 2720–2730.
163. TURBOMOLE V6.5, a development of University of Karlsruhe and Forschungszentrum Karlsruhe GmbH., available from www.turbomole-gmbh.com, 2013.
164. Ahlrichs, R.; Bär, M.; Häser, M.; Horn, H.; Kölmel, C. *Chem. Phys. Lett.* **1989**, *162*, 165–169.
165. Tao, J.; Perdew, J. P.; Staroverov, V. N.; Scuseria, G. E. *Phys. Rev. Lett.* **2003**, *91*, 146401.
166. Weigend, F.; Ahlrichs, R. *Phys. Chem. Chem. Phys.* **2005**, *7*, 3297–3305.
167. Haase, F.; Ahlrichs, R. *J. Comput. Chem.* **1993**, *14*, 907–912.
168. Treutler, O.; Ahlrichs, R. *J. Chem. Phys.* **1995**, *102*, 346–354.
169. Eichkorn, K.; Weigend, F.; Treutler, O.; Ahlrichs, R. *Theor. Chem. Acc.* **1997**, *97*, 119–124.
170. Eichkorn, K.; Treutler, O.; Öhm, H.; Häser, M.; Ahlrichs, R. *Chem. Phys. Lett.* **1995**, *242*, 652–660.
171. Sierka, M.; Hogekamp, A.; Ahlrichs, R. *J. Chem. Phys.* **2003**, *118*, 9136–9148.
172. Deglmann, P.; May, K.; Furche, F.; Ahlrichs, R. *Chem. Phys. Lett.* **2004**, *384*, 103–107.
173. Weigend, F. *Phys. Chem. Chem. Phys.* **2002**, *4*, 4285–4291.
174. Von Arnim, M.; Ahlrichs, R. *J. Comput. Chem.* **1998**, *19*, 1746–1757.
175. Ahlrichs, R. *Phys. Chem. Chem. Phys.* **2004**, *6*, 5119–5121.
176. Grimme, S.; Antony, J.; Ehrlich, S.; Krieg, H. *J. Chem. Phys.* **2010**, *132*, 154104, –.
177. Deglmann, P.; Furche, F.; Ahlrichs, R. *Chem. Phys. Lett.* **2002**, *362*, 511–518.
178. Grimme, S.; Furche, F.; Ahlrichs, R. *Chem. Phys. Lett.* **2002**, *361*, 321–328.
179. Klamt, A.; Schuurmann, G. *J. Chem. Soc., Perkin Trans. 2* **1993**, 799–805.
180. Shaver, R. J.; Rillema, D. P. *Inorg. Chem.* **1992**, *31*, 4101–4107.
181. Gibson, D. H.; Yin, X. *J. Am. Chem. Soc.* **1998**, *120*, 11200–11201.
182. H. Gibson, D.; Yin, X. *Chem. Commun.* **1999**, 1411–1412.
183. Fujita, E.; Muckerman, J. T. *Inorg. Chem.* **2004**, *43*, PMID: 15554628, 7636–7647.
184. Bokarev, S. I.; Hollmann, D.; Pazidis, A.; Neubauer, A.; Radnik, J.; Kuhn, O.; Lochbrunner, S.; Junge, H.; Beller, M.; Brückner, A. *Phys. Chem. Chem. Phys.* **2014**, *16*, 4789–4796.

185. Chisholm, M. H.; Huffman, J. C.; Rothwell, I. P.; Bradley, P. G.; Kress, N.; Woodruff, W. H. *J. Am. Chem. Soc.* **1981**, *103*, 4945–4947.
186. Castella-Ventura, M.; Kassab, E.; Buntinx, G.; Poizat, O. *Phys. Chem. Chem. Phys.* **2000**, *2*, 4682–4689.
187. Gore-Randall, E.; Irwin, M.; Denning, M. S.; Goicoechea, J. M. *Inorg. Chem.* **2009**, *48*, PMID: 19673484, 8304–8316.
188. Irwin, M.; Jenkins, R. K.; Denning, M. S.; Krämer, T.; Grandjean, F.; Long, G. J.; Herchel, R.; McGrady, J. E.; Goicoechea, J. M. *Inorg. Chem.* **2010**, *49*, 6160–6171.
189. Lukehart, C.; Zeile, J. V. *J. Organomet. Chem.* **1977**, *140*, 309 –316.
190. *CRC Handbook of Chemistry and Physics*, 79th Edition; Lide, D. R., Ed.; CRC Press LLC: Boca Raton, FL, 1998.
191. Sullivan, B. P.; Meyer, T. J. *J. Chem. Soc., Chem. Commun.* **1984**, 1244–1245.
192. Sullivan, B. P.; Meyer, T. J. *Organometallics* **1986**, *5*, 1500–1502.
193. Creutz, C.; Chou, M. H. *J. Am. Chem. Soc.* **2007**, *129*, 10108–10109.
194. Lee, H.-J.; Lloyd, M. D.; Harlos, K.; Clifton, I. J.; Baldwin, J. E.; Schofield, C. J. *J. Mol. Biol.* **2001**, *308*, 937 –948.
195. Mauser, H.; King, W. A.; Gready, J. E.; Andrews, T. J. *J. Am. Chem. Soc.* **2001**, *123*, PMID: 11686683, 10821–10829.
196. Souter, P. F.; Andrews, L. *J. Am. Chem. Soc.* **1997**, *119*, 7350–7360.
197. Castro-Rodriguez, I.; Nakai, H.; Zakharov, L. N.; Rheingold, A. L.; Meyer, K. *Science* **2004**, *305*, 1757–1759.
198. Cokoja, M.; Bruckmeier, C.; Rieger, B.; Herrmann, W. A.; Kühn, F. E. *Angew. Chem., Int. Ed.* **2011**, *50*, 8510–8537.
199. Gibson, D. H. *Chem. Rev.* **1996**, *96*, 2063–2096.
200. Van Rossum; Barry Warsaw; Nick Coghlan, G. Style Guide for Python Code., 2132f8d8bc4; Python.org, 2013.
201. Goodger, D.; van Rossum, G. Docstring Conventions., 4b5a1100c7af; Python.org, 2001.
202. Bulsink, P. TurboControl v1.1.0., <http://github.com/pbulsink/turbocontrol>.
203. Skripnikov, L. Chemissian, a computer program to analyse and visualize quantum-chemical calculations., <http://chemissian.com>.
204. APEX Software Suite v.2010., Bruker AXS: Madison, WI, 2005.
205. Blessing, R. H. *Acta Crystallogr. Sect. A* **1995**, *51*, 33–38.
206. Sheldrick, G. Cell_Now., Bruker AXS: Madison, WI, 2004.
207. Sheldrick, G. M. *Acta Crystallogr. Sect. A* **2008**, *64*, 112–122.

208. Spurrier, N. Pexpect, version 3.2., <http://pexpect.readthedocs.org/en/latest/index.html>.
209. Open Babel Package, version 2.3.1., <http://openbabel.org>.
210. O'Boyle, N. M.; Banck, M; James, C. A.; Morley, C; Vandermeersch, T; Hutchison, G. R. *J. Cheminf.* **2011**, *3*, 33.

Todo list

add last struct	53
-----------------	-------	----